

1 Detecting and quantifying palaeoseasonality in stalagmites using geochemical
2 and modelling approaches

3 James U.L. Baldini¹, Franziska A. Lechleitner^{2, 3}, Sebastian F.M. Breitenbach⁴, Jeroen van
4 Hunen¹, Lisa M. Baldini⁵, Peter M. Wynn⁶, Robert A. Jamieson⁷, Harriet E. Ridley¹, Alex J.
5 Baker⁸, Izabela W. Walczak⁹, and Jens Fohlmeister^{10, 11}

6 ¹Department of Earth Sciences, Durham University, DH1 3LE, United Kingdom.

7 ²Department of Earth Sciences, University of Oxford, South Parks Road, Oxford OX1 3AN,
8 United Kingdom.

9 ³Laboratory for the Analysis of Radiocarbon with AMS (LARA), Department of Chemistry and
10 Biochemistry, and Oeschger Centre for Climate Change Research, University of Bern,
11 Freiestrasse 3, 3012 Bern, Switzerland.

12 ⁴Department of Geography and Environmental Sciences, Northumbria University,
13 Newcastle upon Tyne, NE1 8ST, United Kingdom.

14 ⁵School of Health & Life Sciences, Teesside University, Middlesbrough, TS1 3BX, United
15 Kingdom

16 ⁶Lancaster Environment Centre, Lancaster University, Lancaster, LA1 4YQ, United Kingdom.

17 ⁷School of Earth and Environment, University of Leeds, Leeds, LS2 9JT, United Kingdom

18 ⁸National Centre for Atmospheric Science and Department of Meteorology, University of
19 Reading, RG6 6BB, United Kingdom.

20 ⁹Durham Centre for Academic Development, Durham University, Durham, DH1 1TA, United
21 Kingdom.

22 ¹⁰Potsdam Institute for Climate Impact Research, Telegrafenberg, 14473 Potsdam, Germany.

23 ¹¹GFZ German Research Centre for Geosciences, Section 'Climate Dynamics and Landscape
24 Development', Telegrafenberg, 14473 Potsdam, Germany.

25

26

27

28 **Abstract**

29 Stalagmites are an extraordinarily powerful resource for the reconstruction of climatological
30 palaeoseasonality. Here, we provide a comprehensive review of different types of
31 seasonality preserved by stalagmites and methods for extracting this information. A new
32 drip classification scheme is introduced, which facilitates the identification of stalagmites
33 fed by seasonally responsive drips and which highlights the wide variability in drip types
34 feeding stalagmites. This hydrological variability, combined with seasonality in Earth
35 atmospheric processes, meteoric precipitation, biological processes within the soil, and cave
36 atmosphere composition means that every stalagmite retains a different and distinct (but
37 correct) record of environmental conditions. Replication of a record is extremely useful but
38 should not be expected unless comparing stalagmites affected by the same processes in the
39 same proportion. A short overview of common microanalytical techniques is presented, and
40 suggested best practice discussed. In addition to geochemical methods, a new modelling
41 technique for extracting meteoric precipitation and temperature palaeoseasonality from
42 stalagmite $\delta^{18}\text{O}$ data is discussed and tested with both synthetic and real-world datasets.
43 Finally, world maps of temperature, meteoric precipitation amount, and meteoric
44 precipitation oxygen isotope ratio seasonality are presented and discussed, with an aim of
45 helping to identify regions most sensitive to shifts in seasonality.

46

47 **1. Introduction**

48 Over the past few decades stalagmites have become one of the most important terrestrial
49 archives of climate and environmental change. Their widespread distribution, amenability to

50 radiometric dating, and capacity for retaining seasonal- to decadal-scale environmental
51 information have made them indispensable archives for a wide variety of climate information,
52 most commonly rainfall or temperature variability. The field has developed rapidly, and it is
53 now clear that stalagmites generally do not record a single climate parameter (e.g., cave
54 temperature, rainfall amount, [etc.](#)) exclusively, but instead record a combination of
55 processes. It is increasingly acknowledged that every stalagmite contains a robust history of
56 some aspect of environmental change. The issue is one of complexity; generally speaking, the
57 stalagmite with the least complex signal is considered the ideal. Records generated from
58 stalagmites with more complex stratigraphies, whose drip flow route changes through time,
59 or that are influenced by numerous environmental processes, often prove more difficult to
60 interpret. Some stalagmite records may miss short-lived climate excursions because they are
61 fed by drips that do not respond to the transient climate forcing in question. Others might
62 lose sensitivity or respond non-linearly to a climate forcing; for example, a stalagmite might
63 record droughts faithfully, but miss exceptionally wet intervals when the epikarst (the highly
64 fractured transition zone between soil and bedrock) is saturated with water. To exacerbate
65 the issue further, most [published](#) stalagmite records lack the requisite [analytical](#) resolution to
66 detect palaeoseasonality, an aspect of the climate signal that is increasingly recognised as
67 critical to the interpretation of geochemical records from stalagmites (Baldini et al., 2019;
68 Morellón et al., 2009; Moreno et al., 2017). In other words, the desired climate signal is often
69 compromised by: i) inherent complexities associated with the hydrological transfer of the
70 climate signal to the stalagmite, ii) overprinting of the desired climate-driven signal by other
71 environmental variables, and iii) bias introduced via the necessarily selective sampling of the
72 stalagmite for analysis. The challenge for palaeoclimatologists is to extract and correctly
73 interpret the desired climate signal from a stalagmite, bearing these complexities in mind.

74 The detection of a seasonality signal within a stalagmite can greatly help interpret all datasets
75 from a stalagmite sample, of any temporal resolution. For example, the detection of a
76 seasonal geochemical cycle can contribute to chronological models (Baldini et al., 2002;
77 Carlson et al., 2018; Ridley et al., 2015b), in some cases permitting the development of high-
78 precision chronologies over extended time intervals (Ban et al., 2018; Carlson et al., 2018;
79 Duan et al., 2015; Nagra et al., 2017; Ridley et al., 2015b; Smith et al., 2009). Unlike most
80 other laminated records (e.g., tree rings, ice cores), high-precision radiometric dates can
81 anchor stalagmite layer count chronologies, reducing accumulated counting errors. Proxy
82 information from laminated stalagmites can be linked to environmental variability at seasonal
83 resolution (Matthey et al., 2010; Orland et al., 2019; Ridley et al., 2015b), allowing much
84 needed insights into past climatic dynamics that are difficult to obtain otherwise.

85 The fact that stalagmites can reveal palaeoseasonality, a notoriously difficult climate
86 parameter to reconstruct, is critical for identifying wholesale shifts in climate belts. For
87 example, monthly-scale geochemical data from a stalagmite has detected variability in the
88 Intertropical Convergence Zone influence on rainfall seasonality in Central America over the
89 last two millennia (Asmerom et al., 2020) and the shift from a maritime to a more continental
90 climate in western Ireland in the early Holocene (Baldini et al., 2002), transitions which must
91 otherwise be inferred using annual- to centennial-resolution data (e.g., Breitenbach et al.,
92 2019). High spatial resolution approaches yielding palaeoseasonality can distinguish rainfall
93 occurring at different times of the year, for example, monsoonal rainfall versus dry season
94 rainfall (Ban et al., 2018; Ronay et al., 2019), providing a wealth of information
95 unattainable by other means.

96 Seasonality is one of climate's most important aspects, and this is reflected in the basic
97 subdivisions of the Köppen system, the most commonly used climate classification scheme
98 (Köppen, 1918; Peel et al., 2007). Reconstructing past seasonality is not only relevant for pure
99 palaeoclimatological studies, but also for palaeobotany and archaeology, and for establishing
100 a benchmark by which to compare recent changes in seasonality during the Anthropocene;
101 recent research suggests seasonality in rainfall (e.g., Feng et al., 2013) and temperature (e.g.,
102 Santer et al., 2018) are shifting under modern climate change. This is particularly concerning
103 because changing seasonality has had broad ecological and social implications in the past. For
104 example, human dispersal through Asia was limited more by water availability than by
105 temperature, and likely followed habitable corridors with favourable rainfall seasonality (Li et
106 al., 2019; Parton et al., 2015; Taylor et al., 2018). Also, the domestication and dispersal of
107 crops are linked to rainfall seasonality because optimal growth
108 conditions depend on hydrological conditions. In the Fertile Crescent, barley and wheat were
109 sown in autumn, because in this semi-arid region the winter rains are the limiting factor for
110 their prosperity (Spengler, 2019). Similarly, abundant evidence now exists that variability in
111 seasonal rainfall has played a key role in the waxing and waning of major civilisations (Hsiang
112 et al., 2013; Kennett et al., 2012).

113 Despite the clear importance of reconstructing palaeoseasonality, it is rarely directly
114 observable in climate proxy records. The obfuscation of seasonality by undersampling or
115 aliasing is often a consequence of logical and pragmatic choices designed to maximise returns
116 from available resources. Ideally, analyses would resolve nearly the full climate signal residing
117 within every stalagmite, but this is neither logistically (given the time and funding required)
118 nor realistically (given that the karst system transmutes the signal) possible.

119 Here we review both the advantages of obtaining palaeoseasonality information and methods
120 for its reconstruction using stalagmite geochemistry and modelling, as well as common issues
121 in extracting this information. A short review of the history of speleothem science and
122 techniques frames the discussion and highlights how speleothems have become the premier
123 archives for annual- to sub-annual scale terrestrial climate reconstructions, particularly during
124 the Quaternary. We also suggest a methodology to maximise the likelihood of successfully
125 extracting palaeoseasonality information from a stalagmite, including evaluating the
126 hydrological characteristics of the drip feeding a stalagmite sample prior to collection,
127 modelling palaeoseasonality from lower resolution data, and determining the seasonality of
128 the climate at (and in regions near) the site.

129

130 **2. Background and technique development**

131 Very early studies demonstrated the potential of stalagmites to record climate information
132 (Allison, 1923, 1926; Broecker, 1960; Orr, 1952). However, the real growth in the application
133 of stalagmites as climate archives occurred after the convergence of Thermal Ionisation Mass
134 Spectrometry (TIMS) uranium-thorium dating of stalagmites in the 1990s (e.g., Edwards et al.,
135 1987; Edwards and Gallup, 1993) (which allowed accurate dating) and high resolution
136 sampling techniques in the 2000s (permitting the reconstruction of climate on sub-decadal
137 timescales). The subsequent development and proliferation of multi-collector inductively
138 coupled plasma mass spectrometry (MC-ICP-MS) permitted extraordinarily robust (precise
139 and accurate) chronological control (e.g., Cheng et al., 2013; Hellstrom, 2003; Hoffmann et
140 al., 2007), while the development of a variety of microanalytical techniques provided climate
141 proxy information of an unparalleled temporal resolution. The realisation in the late 1990s

142 (Roberts et al., 1998) and early 2000s that stalagmite carbonate trace element compositions
143 and isotope ratios often vary seasonally (Baldini et al., 2002; Fairchild et al., 2000; McMillan
144 et al., 2005; Treble et al., 2003; Treble et al., 2005b) opened the door to the investigation of
145 palaeoseasonality on an unprecedented level.

146

147 **2.1. Increasing resolution of analysis**

148 Immense technical progress has facilitated the transition from the first speleothem studies,
149 which broadly placed periods of speleothem growth into the global climatic context (Harmon,
150 1979; Hendy and Wilson, 1968; Thompson et al., 1975), to [studies adopting](#) increasingly
151 detailed sub-annual resolution [sampling](#) (Fairchild et al., 2001;
152 Johnson et al., 2006; Liu et al., 2013; Matthey et al., 2008; Maupin et al., 2014; Myers et al.,
153 2015; Ridley et al., 2015b; Ronay et al., 2019; Treble et al., 2005a). Methodological
154 developments, particularly after the mid-2000s and particularly with respect to trace element
155 analysis, greatly reduced the required sample size and increased measurement precision. This
156 included the widespread adoption of micromilling techniques (Spötl and Matthey, 2006), laser
157 ablation (Müller et al., 2009; Treble et al., 2003), secondary ionisation mass spectrometry
158 (Baldini et al., 2002; Fairchild et al., 2001; Finch et al., 2001; Kolodny et
159 al., 2003; Orland et al., 2008, 2009), and the development of protocols for stable carbon and
160 oxygen isotope measurements with reduced sample sizes (Breitenbach and Bernasconi,
161 2011), [including cold-trap methods capable of analysing less than 5 µg of carbonate powders](#)
162 (Vonhof et al., 2020)

163 .

164 .

165 Here, we apply the recently compiled Speleothem Isotope Synthesis and Analysis (SISAL)
166 database v1b (Atsawawaranunt et al., 2018; Comas-Bru et al., 2019) to document the
167 evolution of speleothem stable isotope record resolution. SISAL was created with the primary
168 objective of providing access to a comprehensive repository of published stalagmite $\delta^{18}\text{O}$
169 records to the palaeoclimate community and for climate model evaluation (Comas-Bru and
170 Harrison, 2019; Comas-Bru et al., 2019). SISALv1b contains 455 speleothem records (i.e., SISAL
171 'entities') from 211 globally distributed caves published since 1992 (Comas-Bru et al., 2019).
172 More than half the records (264) included in the database cover at least portions of the last
173 10,000 years.

174 To investigate how stable isotope record resolution has evolved over the last three decades,
175 we extracted all records from the database and calculated their temporal resolution as the
176 absolute difference between two consecutive samples. Hiatuses and gaps in the individual
177 records were excluded from the analysis, as these would have erroneously suggested much
178 lower resolution than that actually present. In a second step, we performed the same
179 calculation, considering only Holocene records.

180 The analysis reveals how the number of speleothem stable isotope records steadily increased
181 with publication year (Figure 1), highlighting the increased popularity of speleothem science
182 over the past three decades. A trend of increasing temporal resolution with time becomes
183 apparent after binning all records published in the same year and calculating their mean
184 resolution (Figure 1). This trend becomes even clearer when only Holocene records are
185 considered, with a particularly striking increase in resolution over recent years (post-2010)
186 (records pre-2010: mean resolution = 50.1 years, STDEV = 38.9 years; records between 2010
187 and 2018: mean resolution = 16.5 years, STDEV = 7.4 years), and is likely related to the

188 widespread adoption of microanalytical advances. Additionally, a record's resolution will
189 typically depend on the time period covered by the record; in general, resolution is higher in
190 Holocene records compared to the full dataset, which includes older records as well. This
191 partly arises because of greater availability of independent data and information on climate
192 conditions during more recent time intervals, thus requiring higher resolution records to
193 tackle relevant research questions. It may also be partially due to typically lower growth rates
194 during the last glaciation compared to the Holocene. However, overall, only nine of the
195 records in SISALv1b have resolution <0.5 years, directly allowing for investigations of
196 paleoseasonality. This highlights the difficulties often encountered with conventional
197 sampling techniques, as this compilation only includes stable isotope records, and does not
198 consider other methods (e.g., laser ablation trace element analysis), which can generate
199 higher resolution time-series. The increasing resolution possible via technological
200 developments has largely involved the analysis of trace elements, whereas stable isotope
201 analysis still predominantly relies on micromilling or drilling techniques.

202

203 **2.2. Transition from temperature to rainfall amount to seasonality**

204 Early speleothem palaeoclimate studies focused on using $\delta^{18}\text{O}$ to generate quantitative cave
205 temperature records (Gascoyne et al., 1980; Hendy and Wilson, 1968; Lauritzen, 1995;
206 Lauritzen and Lundberg, 1999), based on the insight that oxygen isotope fractionation during
207 carbonate deposition is temperature dependent (Epstein et al., 1951; O'Neil et al., 1969), and
208 building on similar work on marine carbonates (Emiliani, 1955). It was quickly recognised
209 however that speleothem $\delta^{18}\text{O}$ is a complex mixed signal reflecting variations in cave
210 temperature, changes in dripwater isotope composition, and various kinetic effects, which

211 severely hamper the use of this proxy for quantitative temperature reconstructions
212 (McDermott, 2004). The subsequent shift in how speleothem $\delta^{18}\text{O}$ is interpreted led to its
213 establishment as a proxy for past hydroclimate changes, including atmospheric circulation,
214 regional temperature, moisture source dynamics, and amount of precipitation (Lachniet,
215 2009).

216 At the same time, the toolkit of geochemical proxies available to speleothem researchers
217 continued to expand. In particular, trace element concentrations in speleothem carbonate
218 emerged as tracers for numerous processes, from surface productivity to karst hydrology and
219 transport (Borsato et al., 2007; Fairchild et al., 2001; Huang and Fairchild, 2001; Treble et al.,
220 2005a). The combination of multiple proxies measured on the same speleothem provided a
221 means to disentangle complexities regarding mixed signals in individual proxies and allowed
222 a progressively deeper understanding of the archive and the associated processes in soil,
223 karst, atmosphere, and cave. In tandem with these developments regarding the climate proxy
224 development, monitoring of cave and local atmospheric conditions became increasingly
225 important, as it was recognised that understanding sometimes highly localised controls on
226 geochemical signatures is crucial for their interpretation (Genty, 2008; Matthey et al., 2008;
227 Matthey et al., 2010; Spötl et al., 2005; Verheyden et al., 2008).

228 The presence of annual petrographic cyclicity within stalagmites was recognised very early on
229 (Allison, 1926). The later identification of visible and luminescent annual banding (Baker et
230 al., 1993; Broecker, 1960; Shopov et al., 1994) underscored that the deposition, mineralogy,
231 and chemical composition of speleothems varied seasonally. However, the concept of
232 seasonal shifts in climate variables (e.g., temperature, precipitation) as contributing to the
233 net multi-annual climate signal did not gain traction until the early to mid-2000s (Wang et al.,

234 2001). Cave monitoring revealed drip rate seasonality in Pere Noel Cave, Belgium (Genty and
235 Deflandre, 1998), Crag Cave, Ireland (Baldini et al., 2006), and in Soreq Cave, Israel (Ayalon et
236 al., 1998), and seasonality was discussed within the context of a speleothem-based trace
237 element study at Grotta di Ernesto, Italy (Huang et al., 2001). Meteorological data were
238 compared to seasonal trace element data for an Australian stalagmite (Treble et al., 2003),
239 and the potential to use seasonal-scale geochemical data to reconstruct the East Asian
240 Summer Monsoon (EASM) was investigated using a stalagmite from Heshang Cave, China
241 (Johnson et al., 2006). Studies coupling cave environmental monitoring and ‘farmed’
242 carbonate precipitates were critical for clarifying the links between hydrological and cave
243 atmosphere conditions on the chemistry of stalagmites, including at a seasonal scale
244 (Czuppon et al., 2018; Moerman et al., 2014; Sherwin and Baldini, 2011; Tremaine et al.,
245 2011). Drip monitoring was also key for establishing how cave hydrology attenuates seasonal
246 and interannual rainfall variability, and was used to predict ENSO variability preservation
247 within stalagmites (Chen and Li, 2018; Moerman et al., 2014). These studies all illustrate that
248 a thorough understanding of annual geochemical cycles requires the development of
249 extensive cave monitoring records, which highlight the complexities inherent in signal
250 transfer from surface environment to the stalagmite.

251

252 **2.3. Importance of monitoring for understanding the seasonal signal**

253 Monitoring environmental conditions in and above a cave at a high temporal resolution
254 greatly improves the accuracy of palaeoclimate interpretations derived from stalagmites.
255 Linking proxy characteristics at a given site with current environmental conditions via
256 monitoring is relevant for reconstructing past conditions. Although modern conditions may

257 differ from ancient conditions, monitoring the cave environment [clarifies](#)
258 processes operating at a site, including the timing and extent of ventilation and the general
259 nature of a hydrological signal, acknowledging that some hydrological re-routing may have
260 occurred through time for certain drip types.

261 Understanding a stalagmite geochemical proxy record is difficult without first understanding
262 how that signal is transferred and altered from the external environment to the sample.
263 Environmental changes affecting the seasonal signal fall under four main categories: *i) Earth*
264 *atmospheric, ii) meteoric precipitation, iii) biological* (e.g., soil processes), and *iv) cave*
265 *atmospheric*.

266 *Earth atmospheric* processes affect the seasonality signal retained within stalagmites by
267 influencing meteoric precipitation isotope ratios at the cave site. Possibly the most common
268 atmospheric process is the seasonal variation in precipitation $\delta^{18}\text{O}$ induced by shifts in the
269 temperature-dependent water vapour-meteoric precipitation fractionation factor. Other
270 related changes in atmospheric processing include seasonal shifts in moisture source and
271 pathway of the moisture package to the cave site, as, for example, in monsoonal settings.

272 *Meteoric precipitation* variability regards the nature of the primary
273 rainfall amount-derived seasonality signal. Here we include meteoric precipitation amount
274 and seasonal distribution as separate from 'Earth atmospheric' processes (such as changes in
275 moisture source), although clearly the latter affect the former. Meteoric precipitation
276 is a fundamental control on stalagmite seasonality that is worth considering independently of
277 other atmospheric processes. Stalagmites deposited in monsoonal climates (e.g., the East
278 Asian Summer Monsoon, Indian Summer Monsoon, South American Monsoon, and Australian
279 Summer Monsoon) with distinct wet and dry seasons are excellent examples of samples

280 whose geochemistry generally (but not always) responds to hydrologic seasonality. In
281 temperate mid-latitude settings with more evenly distributed rainfall, hydrological shifts
282 might record less seasonal than inter-annual (e.g., ENSO) dynamics or possess a seasonal bias
283 (see section 3.1) derived from effective infiltration dynamics.

284 **Biological (soil-derived)** seasonality is the least clearly defined control, and predominantly
285 affects the trace element composition and carbon isotope ratio of cave percolation waters.
286 However, evidence also exists that increased soil bioproductivity can affect oxygen isotope
287 ratios by preferential uptake of water during the growing season during intervals with
288 substantial surface vegetation (Baldini et al., 2005). Trace element transport critically
289 depends on the biological activity and water supply, both factors that are inherently variable
290 and not necessarily in-phase. Hydrology can affect biological seasonality, as leaching of
291 organic matter and trace elements from freshly decomposed litter depends on excess
292 infiltration. Soils may thus produce a wet season pulse of colloidal material (organics as well
293 as weathering products) which contributes to an annual peak in trace element concentrations
294 in some samples; such dynamics are highly site-specific. The evidence for this pulse is derived
295 both from synchrotron-based stalagmite studies (e.g., Borsato et al., 2007) and daily-scale
296 automated dripwater collection schemes (Baldini et al., 2012). Treble et al. (2003) suggest
297 phosphorous enrichment in stalagmite carbonate stemming from seasonal infiltration pulses,
298 and monitoring at Shihua Cave (China) revealed that organic carbon was transported during
299 the wet season (Ban et al., 2018; Tan et al., 2006). Whether this pulse is truly independent
300 from hydrological variability is unclear, but some evidence from dripwater monitoring in
301 temperate Irish caves suggests that the seasonal trace element pulse is not associated with
302 increased autumnal water throughput, but rather with seasonal vegetation die-back (Baldini

303 et al., 2012). In monsoonal north-eastern India biologically-induced litter decomposition
304 reaches a maximum in early summer (Ramakrishnan and Subhash, 1988), which increases
305 element availability in the soil that can be leached during the entire wet season (Khiewtam
306 and Ramakrishnan, 1993). Trace element transport may also hinge
307 directly on the presence of natural organic matter in dripwater, which may link the dripwater
308 directly to surface bioproductivity (Hartland et al., 2012; Hartland et al., 2011). Thus,
309 biological seasonality is highly site-specific and likely variable through time; this and the
310 complexities outlined above underscore the importance of dripwater monitoring campaigns.

311 **Cave atmospheric** variability can also impart a seasonal signal to a stalagmite geochemical
312 record. Seasonal changes in cave air mixing with outside air lead to conditions within the cave
313 that lower cave air carbon dioxide partial pressure ($p\text{CO}_2$) and potentially even contribute to
314 dripwater evaporation, promoting calcite deposition. Cave atmosphere variability, induced by
315 ventilation (through thermal gradients or changing wind patterns) therefore affects the
316 calcite deposition seasonality, as well as kinetic fractionation amount. Excellent examples of
317 caves whose stalagmites are affected by this variability include New St. Michael's Cave
318 (Gibraltar) (Mattey et al., 2016; Mattey et al., 2010) and numerous caves in Central Texas
319 (Banner et al., 2007; Breecker et al., 2012; Cowan et al., 2013; Wong et al., 2011). These
320 effects are discussed in detail below (Section 3).

321

322 **3. Issues inherent to speleothem-based high-resolution climate reconstructions**

323 Detecting any seasonal component in a stalagmite climate signal includes quantifying growth
324 rate and input signal seasonality. It is worth noting that the input signal is sometimes

325 unexpected, and a thorough site monitoring scheme can help identify the main contributing
326 factors. For example, although many trace element ratios (and particularly Mg/Ca) are
327 affected by recharge (often via prior calcite precipitation (PCP) mechanisms (Fairchild
328 and Treble, 2009)), other factors can also influence (seasonal) stalagmite geochemistry. This
329 is the case at ATM Cave, Belize, where various trace element/calcium ratios (including
330 Mg/Ca) increase in concentration at the beginning of the annual rainy season, and
331 are probably linked to dry deposition during the preceding dry season followed by transport
332 to the stalagmite with the onset of the rainy season (Jamieson et al., 2015). In other cases,
333 the advection of atmospheric aerosols directly into the cave can affect the stalagmite trace
334 element signal (Dredge et al., 2013). Seasonal non-deposition caused by either drying of the
335 feeder drip or by seasonally high cave air $p\text{CO}_2$ can bias any record where every data point
336 integrates more than a few months of deposition. From this perspective, most stalagmite
337 records include palaeoseasonality information to some extent, but, without
338 appropriate monitoring strategies in place, deconvolving the extent to which the shifting
339 seasonal signal dominates the overall record is difficult.

340

341 **3.1. Mixing within the aquifer**

342 The degree of recharge mixing within the aquifer and epikarst is a fundamental control on the
343 preservation of a seasonality signal within stalagmites. A long residence time and/or thorough
344 mixing within the overlying aquifer can greatly attenuate any hydrological seasonal signal,
345 and understanding the hydrology feeding a cave drip is therefore critical (Atkinson, 1977;
346 Ayalon et al., 1998; Baker et al., 1997; Baker and Brunson, 2003; Baker et al., 2019; Kaufman

347 et al., 2003). For conservation and logistical reasons, monitoring and classification of the drip
348 should ideally occur prior to sampling a stalagmite.

349 Smart and Friedrich (1987) undertook one of the earliest efforts to comprehensively
350 categorise cave drips. Their scheme involved measuring drip rates at G.B. Cave, in the Mendip
351 Hills, UK, and parameterising them by plotting maximum drip rate versus the coefficient of
352 variation (C.V.; the standard deviation divided by the mean multiplied by 100). Baker et al.
353 (1997) later modified the scheme, dividing drips into six categories (seepage flow, seasonal
354 drip, percolation stream, shaft flow, vadose flow, subcutaneous flow). Other classification
355 schemes (e.g., Arbel et al., 2010; Arbel et al., 2008) focussed on analysing drip hydrographs,
356 and suggested terminology such as 'post-storm', 'seasonal', 'perennial', and 'overflow', which
357 are broadly consistent with the categories introduced by Smart and Friedrich (1987). The
358 introduction of automated drip loggers revolutionised the field (Mattey and Collister, 2008),
359 partly by ensuring that short-lived hydrological events were not missed. This
360 ensured a substantially more robust characterisation of drips than that possible via manually
361 measuring drip rates only during on-site visits.

362 Understanding the hydrology feeding a stalagmite is fundamental for determining if a
363 stalagmite retains a seasonal signal. Drip rate is controlled by surface processes (e.g.,
364 meteoric precipitation, evaporation, soil moisture capacity, and susceptibility to runoff) and
365 aquifer characteristics including reservoir capacity and bedrock permeability (Markowska et
366 al., 2015; Treble et al., 2013). Bedrock pathways recharging a drip are broadly divisible into
367 diffuse (or 'matrix'), fracture, and conduit flows
368 (Ayalon et al., 1998; Baker et al., 1997; Perrin et al., 2003; Smart and Friedrich, 1987), and
369 recent models suggest that many drips are a combination of diffuse and fracture flow.

370 Diffuse permeability typically refers to either the primary intra-granular bedrock
371 permeability or to secondary permeability along fine fractures, and is characterised by a slow
372 response to precipitation events and a large reservoir capacity (Atkinson, 1977; Smart and
373 Friedrich, 1987). Fracture permeability relates to potentially solution-enlarged bedding plane
374 partings and joints and is characterised by a rapid to intermediate response to precipitation
375 events, and a low to moderate storage capacity. Conduit permeability refers to often
376 solutionally-enlarged pipe-like openings >1 cm in diameter (Atkinson, 1977; Smart and
377 Friedrich, 1987). Such conduit flow is characterised by a rapid response to storm events
378 followed by a rapid return to baseline flow (Baldini et al., 2006), and often carries chemically
379 aggressive waters that do not allow secondary carbonate deposition. Large conduits or
380 bedding planes may intersect a network of more diffuse hydrological pathways, leading to
381 dual-component flow where the fracture is itself fed by some diffuse recharge in addition to
382 the fracture flow. The hydrologic permeability of the fracture flow component compared to
383 the diffuse flow component essentially defines the drip type; 100% diffuse flow would exhibit
384 no response to storm events, whereas 100% fracture flow would usually have no drip except
385 for immediately following storm events large enough to activate the pathway (Figure 2). Most
386 drips would fall along the spectrum between these two endmembers; a constant base drip
387 (the diffuse flow component) combined with a variably rapid response to storm events (the
388 fracture flow component).

389 From a seasonality perspective, pure fracture-flow drips vary considerably seasonally but may
390 experience occasional dripwater undersaturation and/or drying, and consequently the
391 resultant stalagmite could have abundant 'crypto-hiatuses' (hiatuses in growth
392 too brief to leave a clear petrographic expression, or appear in chronological models (Stoll et
393 al., 2015), also referred to as

Formatted: Font: 12 pt

394 [‘microhiatuses’ \(Baker et al., 2014; Moseley et al., 2015\)](#).
395 [We suggest that if these hiatuses are demonstrably seasonally, ‘seasonal hiatus’ is](#)
396 [appropriate terminology.](#) Drips characterised by 100% diffuse flow would be stable with little
397 hydrological or biological seasonality. [Although](#) the likelihood for [seasonal](#)
398 [hiatuses](#) or drying is low for stalagmites fed by diffuse flow, the seasonal signal is probably
399 muted, unless at a site where the seasonal signal is controlled by a forcing other than
400 hydrological variability (see Section 2.4.). The optimal hydrology for imparting seasonality
401 onto a stalagmite is a drip fed by moderately diffuse flow that is responsive to monthly-scale
402 shifts in rainfall, but that does not have a substantial fracture component to transmit event-
403 scale (and possibly undersaturated) water.

404

405 **3.2. Non-deposition and seasonal bias in samples**

406 Although growth hiatuses lasting longer than a few years are often (but not always) apparent
407 within stalagmites as horizons of detrital material followed by competitive growth of
408 carbonate crystals (Broughton, 1983), brief growth hiatuses occurring seasonally are often
409 undetectable (though occasionally they have a petrographic manifestation). Thus, the
410 existence of these [seasonal](#) hiatuses is often inferred by applying monitoring data to
411 isolate intervals through the year where environmental conditions suggest temporary non-
412 deposition could exist. Because drip rate is one of the fundamental controls on stalagmite
413 growth (Genty et al., 2001), the use of drip loggers to detect seasonal drying of the stalagmite
414 feeder drip is important for understanding whether a stalagmite record excludes a certain
415 season’s climate information.

416 Additionally, careful examination of sample petrography can reveal important insights into
417 the nature of the climate signal retained by a stalagmite. Petrographic microscopy helps in
418 identifying growth interruptions caused by lack of water, and dissolution features caused by
419 undersaturated dripwater. An excellent example of this approach exists for Holocene
420 stalagmites from northern Spain (Railsback et al., 2011; Railsback et al., 2017); the analysis
421 reveals horizons of dissolution (termed Type 'E' surfaces), interpreted as reflecting occasional
422 undersaturation of the feeder drip. Other examples of careful petrographic analysis informing
423 seasonality studies are provided from Drotzky's Cave, Botswana, where the alternating wet
424 and dry seasons are manifested by alternating calcite and aragonite (respectively)
425 laminae (Railsback et al., 1994) and from Grotta di Carburangeli, Italy, where columnar fabrics
426 were interpreted as reflected pronounced seasonal drip rate variability (Frisia,
427 2015).

428 Cave air carbon dioxide concentrations ($p\text{CO}_2$) are inversely linked to
429 stalagmite growth rate (Banner et al., 2007; Sherwin and Baldini, 2011). For example, in a
430 study of three caves across Texas, it was observed that formed calcite growth rate was
431 inversely correlated with cave air $p\text{CO}_2$ (Banner et al., 2007). Negligible calcite growth and
432 even seasonal hiatuses occurred during the warmest summer months, when cave air
433 $p\text{CO}_2$ increased due to low cave ventilation rates (Banner et al., 2007). Elevated cave air $p\text{CO}_2$
434 discourages the dripwater's thermodynamic tendency to degas CO_2 , thereby slowing the
435 carbonate precipitation rate. In most caves where the entrance is located above the rest of
436 the cave, outside air with low $p\text{CO}_2$ advects into the cave when the outside air density
437 becomes greater than the cave air density (e.g., Spötl et al., 2005). This is usually driven by
438 temperature gradients; colder, denser air moves down into a cave during winter, lowering

439 the cave air $p\text{CO}_2$ and encouraging stalagmite growth (James et al., 2015). However, cave air
440 $p\text{CO}_2$ does not act in isolation, but instead the critical growth determining variable is the
441 differential between cave air $p\text{CO}_2$ and dissolved CO_2 in dripwater (Baldini et al., 2008).
442 Carbonate deposition thus could increase in the high cave air $p\text{CO}_2$ season if the dripwater
443 had equilibrated with an atmosphere with even greater seasonal dissolved CO_2 increases
444 (e.g., stemming from seasonal soil bioproductivity increases) which exceed those of the cave
445 atmosphere. These types of drips are generally quite responsive to rain events, so
446 determining if a seasonal growth bias exists should incorporate both hydrology and cave
447 atmospheric chemistry. Drips with stable drip rates, that are not responsive to storm events
448 may have more constant dissolved CO_2 and therefore seasonal deposition rates that are
449 affected exclusively by cave air $p\text{CO}_2$ dynamics. However, several recent publications suggest
450 that dripwater equilibrates not only with soil air, but also with a reservoir of carbon dioxide
451 within the unsaturated zone of aquifers (termed 'ground air') that may have very high $p\text{CO}_2$
452 values (2 to 7%), much higher than typical soils (0.1 to 2%) (Baldini et al., 2018; Bergel et al.,
453 2017; Markowska et al., 2019; Matthey et al., 2016; Noronha et al., 2015). Thus, it is possible
454 that drip dissolved CO_2 is often near-constant, having equilibrated with a ground air reservoir
455 of near-constant $p\text{CO}_2$, and that carbonate precipitation is anticorrelated with cave air $p\text{CO}_2$
456 regardless of drip type, although this requires further research. The complexities of cave
457 atmospheres are now reasonably well understood, but more long datasets describing the
458 dissolved CO_2 of cave drips are essential for determining the variability of cave percolation
459 waters.

460 Although a temperate-zone (Peel et al., 2007) cave's tendency to ventilate during the winter
461 is generally predictable from seasonality in external temperature (James et al., 2015),

462 occasionally cave geometry provides a more dominant control. In New St. Michael's Cave in
463 Gibraltar, ventilation is driven by seasonal changes in wind speed and direction (Mattey et al.,
464 2016; Mattey et al., 2009). The cave experiences the lowest cave air $p\text{CO}_2$ values in summer,
465 and consequently growth (assuming constant drip rate) is biased towards summer (Baker et
466 al., 2014). The cave's position high within the Rock of Gibraltar contributes to strong winds
467 and unusual seasonal ventilation, illustrating how cave position or geometry can dominate
468 seasonal ventilation patterns. Other examples include Bunker Cave in Germany, where an
469 essentially horizontal plan with little altitude difference between entrances produces very
470 little seasonal variability in $p\text{CO}_2$ (e.g., Riechelmann et al., 2011; Riechelmann et al., 2019),
471 and Císařská Cave (Czech Republic) where a U-shaped cave produces nonlinearities between
472 air temperature, density, and ventilation (Faimon and Lang, 2013).

473 Because seasonal hiatuses can lack either a petrological or a geochemical manifestation,
474 cave monitoring is critical for assessing the likelihood of seasonal non-deposition (Shen et al.,
475 2013). Stalagmite growth rate modelling, informed by cave monitoring data, can provide
476 invaluable information regarding how seasonal growth variability affects geochemical climate
477 proxy records integrating more than one year's worth of growth. For example, seasonal non-
478 deposition during summer due to either high evapotranspiration-induced drip cessation or
479 elevated cave air $p\text{CO}_2$ might bias lower resolution records towards wintertime rainfall values
480 (generally towards lower $\delta^{18}\text{O}$ values) (e.g., James et al., 2015) at sites where drip water is not
481 well mixed. Stoll et al. (2012) used an inverse model to illustrate that rainfall seasonality shifts
482 relative to the cave air $p\text{CO}_2$ can greatly affect PCP and consequently stalagmite trace element
483 concentrations. Baldini et al. (2008) used theoretical stalagmite growth rate equations and
484 theory developed previously (Buhmann and Dreybrodt, 1985; Dreybrodt, 1980, 1988, 1999),

485 coupled with monitoring information, to model stalagmite $\delta^{18}\text{O}$ for various drips within Crag
486 Cave (Ireland). The results suggest that the amount of time integrated by the analyses, the
487 nature of the drip, and the ventilation dynamics of the cave, all strongly modulate carbonate
488 $\delta^{18}\text{O}$ signals.

489 These studies all highlight how characterising the surface and depositional environment is
490 critical for interpreting the climate signal. Either seasonal hiatuses or reduced growth
491 may bias annual- (or coarser-) scale geochemical records towards particular seasons.
492 Additionally, it is also important to consider how regional climate shifts may have affected a
493 sample in the past, because modern processes may not have applied throughout the record.
494 Understanding climate signal emplacement processes within stalagmite carbonate is
495 therefore fundamental for building robust climate records.

496

497 **3.3. A drip classification scheme to quantify seasonal responsiveness**

498 Existing drip classification schemes are not designed to characterise the likelihood that a
499 sampled stalagmite retains a hydrologically induced seasonal signal. However, such
500 knowledge is crucial if research goals include a component of seasonal climate reconstruction.
501 Here, we introduce a new drip categorisation scheme that not only permits the identification
502 of stalagmites most likely to retain a hydrology-modulated seasonal climate signal, but that
503 also helps predict the general nature of the climate signal within any sample. This is important
504 for both the accurate interpretation of stalagmite palaeoclimate records, but also for cave
505 conservation (i.e., to maximise the usefulness of collected samples for the purpose of the
506 research goals) and for the appropriate usage of research-related resources. A seasonal-
507 resolution stable isotope record of any length requires considerable resources, and we hope

508 that this new drip classification scheme will help direct these resources to appropriate
509 stalagmite samples.

510 The scheme's essence is the collection of (ideally) at least one year of hourly drip rate data
511 for a drip feeding a stalagmite of interest. For every month, the minimum and maximum
512 hourly drip rate values are extracted. When plotted, these data reveal the extent to which
513 the drip is affected by seasonal activation of fracture permeability, and what proportion of
514 the drip consists of diffuse 'baseflow' (and whether this varies through the year). Drip
515 categorisation then involves evaluating the distribution of the datapoints, and is described
516 with terminology broadly consistent with the Smart and Friedrich (1987) scheme. Because the
517 classification scheme uses multiple data points per site, a very large number of possible
518 combinations of descriptors are possible. For example, some drip sites (e.g., drip site YOK-LD
519 within Yok Balum Cave, Belize; (Ridley et al., 2015a)) are fed by a slow diffuse flow most of
520 the year, where the minimum and maximum monthly drip rates are almost identical (Figure
521 3). However, during wetter months an overflow route is activated, and the maximum drip
522 rate increases substantially, whereas the minimum remains the same; this would be
523 characterised as a diffuse drip with a seasonally active overflow component. If this overflow
524 component is saturated with respect to calcite or aragonite, some seasonal signal may be
525 preserved, but if the overflow water is undersaturated a stalagmite fed by this drip type has
526 less potential for seasonal climate reconstructions. Similarly, drip YOK-SK is characterised by
527 almost entirely invariant diffuse recharge and would not record seasonal changes in recharge
528 (Figure 3). At Leamington Cave (Bermuda), drip BER-drip
529 #5 is fed by diffuse recharge during drier intervals of the year, but during wetter months more
530 water is routed to the diffuse flow, increasing the base flow (Walczak, 2016). Consequently,

531 the drip does experience some seasonality without risk of undersaturation, and thus a
532 stalagmite fed by it should retain hydrology-induced seasonality.

533 In this new drip classification plot, drips that are expected to produce stalagmites that
534 retain the clearest seasonal signal are those that plot with a slope approaching unity. In other
535 words, those that are not fed by either an extremely diffuse drip or an extremely flashy drip,
536 and that consequently respond to seasonal rainfall shifts without transient extreme rapid drip
537 rate episodes caused by individual storm events (which may lead to dripwater
538 undersaturation and signal loss). The two drip sites plotted in Figure 3 that
539 best display this type of behaviour (drips YOK-G and BER-drip #5) have both yielded
540 stalagmites retaining exceptional seasonal signals, stalagmites YOK-G (Ridley et al., 2015b)
541 and BER-SWI-13 (Walczak, 2016). Other drip sites that have a slope approaching unity and
542 have a pronounced difference between the highest and the lowest set of drip rates (Figure
543 3B) should also produce stalagmites with well-developed records of seasonality.

544 Importantly, this drip classification scheme equally helps to identify drips that are unlikely to
545 produce good seasonality records. For example, stalagmites fed by drips that are invariant
546 throughout the year would not record hydrologically-induced seasonality (although a
547 seasonal signal might still be preserved based on non-hydrological factors – see Section 2.4).
548 Stalagmites fed by drips that have one or more monthly values plotting at the origin (i.e., no
549 drips for an entire month, Figure 3D) would contain seasonal hiatuses and would
550 consequently not record that interval's climate information. Drips where the diffuse flow
551 component (i.e., the monthly minimum flow) remains constant but the fracture flow
552 component (i.e., the monthly maximum flow) changes considerably (Figure 3C) may
553 experience undersaturation and either non-deposition or even corrosion of the stalagmite.

554 This classification scheme comes with some caveats. First, as discussed in Section 2.4., it is
555 possible that the seasonality signal is imparted onto the stalagmite independent of hydrology.
556 For example, if seasonal cave ventilation controls the seasonality signal, the application of
557 the scheme would differ. At a site with strong seasonal ventilation, a stalagmite
558 deposited by a purely diffuse flow-fed drip would reflect a largely cave atmospheric
559 seasonality signal (i.e., with no hydrological seasonality). This would reduce the complexity of
560 the geochemical signal and obviate the need to deconvolve hydrological- and cave
561 atmosphere-induced seasonality from any geochemical record produced. Second, some drips
562 are so-called ‘underflow’ drip sites, which respond to recharge linearly up until a maximum
563 drip rate and then become unresponsive to further recharge increases. This is often
564 caused by a constriction in the flow pathway leading to the water egress point into the cave.
565 Despite the lack of variability at high flow, the dripwater is still in dynamic equilibrium with
566 recharge (unlike high residence time diffuse flow fed sites) and the stalagmite may reflect the
567 dripwater isotopic variability. Similarly, some drips are affected by piston flow, whereby an
568 increase in hydrologic head might push through a slug of older water, leading to an
569 instantaneous response to recharge but of water with a signature of
570 ‘old’ water; careful monitoring can identify and mitigate these issues (see Section 3.4).
571 Despite these caveats, this drip evaluation scheme will hopefully provide an efficient means
572 for identifying actively growing stalagmite samples most likely to record a seasonal climate
573 signal prior to collection of that sample.

574

575 **3.4. Dripwater oxygen isotope seasonality**

576 The extent that cave dripwater $\delta^{18}\text{O}$ ($\delta^{18}\text{O}_{\text{dw}}$) values reflect the $\delta^{18}\text{O}$ of meteoric precipitation
577 ($\delta^{18}\text{O}_{\text{p}}$) is critical to climate studies and for understanding the palaeoseasonality signal in
578 particular. Many publications have investigated the relationship between $\delta^{18}\text{O}_{\text{p}}$ and $\delta^{18}\text{O}_{\text{dw}}$
579 (Ayalon et al., 1998; Baker et al., 2019; Baldini et al., 2015; Bar-Matthews et al., 1996; Cruz Jr.
580 et al., 2005; Duan et al., 2016; Feng et al., 2014; Harmon, 1979; Luo et al., 2014; Markowska
581 et al., 2016; Mischel et al., 2015; Moquet et al., 2016; Moreno et al., 2014; Oster et al., 2012;
582 Pu et al., 2016; Riechelmann et al., 2011; Riechelmann et al., 2017; Surić et al., 2017; Tadros
583 et al., 2016; Tremaine et al., 2011; Verheyden et al., 2008; Wu et al., 2014; Yonge et al., 1985;
584 Zeng et al., 2015). Depending on the drip site's hydrological characteristics (Arbel et al., 2010;
585 Baker and Brunson, 2003; Smart and Friedrich, 1987), $\delta^{18}\text{O}_{\text{dw}}$ values may reflect $\delta^{18}\text{O}_{\text{p}}$ on
586 timescales ranging from the annual weighted mean (Baker et al., 2019; Cabellero et al., 1996;
587 Chapman et al., 1992; Yonge et al., 1985) to individual (intense) recharge events (Atkinson et
588 al., 1985; Frappier et al., 2007; Harmon, 1979).

589 Factors such as depth below surface, residence time and mixing of the water within the
590 unsaturated zone, soil depth and texture, and aquifer hydraulics can vary between drip sites.
591 Important reservoirs for storage and mixing of effective rainfall are documented as the soil
592 and epikarst zones (Cabellero et al., 1996; Chapman et al., 1992; Gazis and Feng, 2004; Perrin
593 et al., 2003; Yonge et al., 1985). Rainwater infiltrating into the soil reservoir is variably lost to
594 evapotranspiration but in karst regions preferential recharge through dolines and grikes may
595 occasionally circumvent the soil and related evapotranspiration (e.g., Hess and White, 1989).

596 Dripwater $\delta^{18}\text{O}$ and δD values potted relative to the local meteoric water line can detect
597 secondary evaporation from infiltrating water
598 (Ayalon et al., 1998; Breitenbach et al.,

599 2015). Bar-Matthews et al. (1996) observed a 1.5 ‰ $\delta^{18}\text{O}_{\text{dw}}$ enrichment relative to rainwater
600 and attributed this primarily to seasonal evaporation in the soil and epikarst zones above their
601 Israeli cave site. Evaporative enrichment of infiltrating rainwater is greater in arid and
602 semiarid regions than in temperate regions where conditions of water excess occur through
603 much of the year (Markowska et al., 2016; McDermott, 2004). Any excess, non-
604 evapotranspired water is then transmitted to the epikarst, karst, and finally the cave.
605 Dripwater residence times in the aquifer or epikarst are highly variable, ranging from minutes
606 to years, depending on soil thickness, hydraulic properties (Gazis and Feng, 2004), and drip
607 pathway (e.g., diffuse vs. conduit flow) (Baldini et al., 2006). Mixing of infiltrating rainwater
608 with existing epikarst water can buffer the climate signal and reduce seasonal $\delta^{18}\text{O}_{\text{dw}}$
609 variability from muted to invariant (within analytical error, and assuming no cave
610 atmosphere-induced seasonality) (Baker et al., 2019; Breitenbach et al., 2019; Onac et al.,
611 2008; Schwarz et al., 2009). At some cave sites, $\delta^{18}\text{O}_{\text{dw}}$ does not necessarily correlate with
612 $\delta^{18}\text{O}_{\text{p}}$ shifts, most likely due to mixing within the aquifer (Moquet et al., 2016), underscoring
613 that different hydrologies produce stalagmites retaining different environmental signals.

614 A recent global compilation of available dripwater monitoring data has further clarified the
615 relationship between climate (e.g., mean annual temperature and annual precipitation) and
616 $\delta^{18}\text{O}_{\text{dw}}$ (Baker et al., 2019). In cooler regions where mean annual temperature (MAT) < 10°C,
617 $\delta^{18}\text{O}_{\text{dw}}$ most closely reflects the amount-weighted $\delta^{18}\text{O}_{\text{p}}$ (i.e., evaporation from the soil and
618 epikarst does not exert much influence). In seasonal climates with MAT between 10°C and
619 16°C, $\delta^{18}\text{O}_{\text{dw}}$ values generally reflect the recharge-weighted $\delta^{18}\text{O}_{\text{p}}$ (see Fig. 1 of (Baker et al.,
620 2019)). In regions where MAT > 16°C, $\delta^{18}\text{O}_{\text{dw}}$ is generally higher relative to amount-weighted
621 precipitation $\delta^{18}\text{O}_{\text{p}}$ because fractionation processes related to evaporative effects on stored

622 karst water are more substantial (Baker et al., 2019). Stalagmite $\delta^{18}\text{O}$ records from regions
623 experiencing high temperatures and/or aridity will probably not reflect rainfall $\delta^{18}\text{O}$ (Baker
624 et al., 2019).

625

626 **3.5. The uniqueness of each stalagmite record**

627 Recent publications have made a case for the importance of replication in stalagmite
628 geochemical records (Wong and Breecker, 2015; Zeng et al., 2015), which is a worthwhile and
629 useful goal. Producing the same geochemical record from multiple samples ensures that no
630 analytical issues exist and can facilitate correlating records whose growth intervals overlap in
631 regions and for time periods with high signal-to-noise ratios. Particularly in cases where
632 evidence for a short-lived climate anomaly exists, replication from within the same sample
633 and from other stalagmites is critical. However, stalagmite geochemistry is affected by a
634 myriad of variables, and the precise combination of factors affecting any one sample are
635 essentially unique. Thus, every stalagmite retains a different component of the environmental
636 signal, and a lack of reproducibility does not necessarily indicate that a record is 'incorrect' or
637 flawed. Even stalagmites that are affected by strong kinetic effects retain accurate
638 environmental data; it is a matter of recognising this control and basing any
639 interpretations accordingly.

640 Unless two stalagmites are fed by a very similar drip type (often two samples growing near
641 each other whose feeder drips share the same hydrological pathway), stalagmite records
642 from the same cave may not match. This is a clear consequence of the diversity of possible
643 drip pathways feeding individual stalagmites. For example, a stalagmite growing underneath

644 a diffuse drip fed by an extremely low hydrologic permeability pathway that is unresponsive
645 to large rain events would not contain the same record as a stalagmite growing underneath a
646 drip with no diffuse component but that is instead fed by fracture flow. The former (diffuse
647 flow-fed) stalagmite may retain long-term climate information but lack seasonal-scale
648 information, whereas the latter (fracture flow-fed) stalagmite may retain some seasonal
649 environmental information but may also experience occasional
650 undersaturation following large rain events, leading to hiatuses and information loss.
651 The fracture flow-fed stalagmite may have a more rapid overall growth rate but may
652 experience flow re-routing and stochastic drip variability due to solutional enlargement of the
653 fracture pathway, potentially leading to a shorter overall growth interval due to the eventual
654 diversion of water away from the stalagmite. Once cave- and site-specific ventilation factors
655 are considered as well, it is apparent that no two stalagmites can yield precisely the same
656 record; rather it is imperative to understand the environmental conditions recorded by each
657 individual sample. If the goal is to reconstruct seasonality, it is important to understand the
658 nature of the seasonality signal for each potential sample, e.g., whether the sample is affected
659 by hydrological seasonality or cave atmospheric seasonality. In the latter case, it is then
660 favourable to select a stalagmite from a diffuse flow drip in order to simplify the extraction of
661 the seasonal ventilation signal.

662 The considerable range of stalagmite records possible, even from the same site, is potentially
663 advantageous. The individuality of stalagmite records may yield a powerful tool for the
664 quantitative reconstruction of historically elusive environmental variables. For example,
665 differences in oxygen isotope ratios between two samples from the same site could reflect
666 in-cave temperature-induced kinetic fractionation effects, and modelling (Deininger and

667 Scholz, 2019; Deininger et al., 2016; Dreybrodt, 1988; Dreybrodt and Deininger, 2014;
668 Riechelmann et al., 2013) could theoretically yield the cave temperature, potentially even at
669 a seasonal resolution. This perspective is consistent with the recent appreciation that
670 speleothems deposited at isotopic equilibrium are extremely rare (Daëron et al., 2019;
671 Mickler et al., 2006) and that kinetic effects are an integral part of the environmental signal
672 retained by stalagmites (Millo et al., 2017; Sade and Halevy, 2017). The concept that kinetic
673 effects are undesirable is a vestige of early studies attempting to derive absolute
674 palaeotemperatures from stalagmite oxygen isotope ratios, in which case kinetic effects do
675 indeed interfere with the extraction of the desired signal. However, because stalagmite $\delta^{18}\text{O}$
676 values are no longer considered pure in-cave temperature proxies, kinetic effects no longer
677 present a serious issue, provided that they are considered within any interpretations. In fact,
678 because kinetic effects often vary in sync with the primary rainfall signal (e.g., kinetic effects
679 tend to occur during drier periods accentuating the already elevated stalagmite $\delta^{18}\text{O}$ and $\delta^{13}\text{C}$
680 signature) they tend to help the climate signal stand out above background noise.

681 Stalagmite climate reconstructions are usually based around one record or an overlapping
682 series of records; future research could use the differences between two records (considering
683 in-cave kinetic effects) to reconstruct aspects of the environmental signal, including seasonal
684 temperature shifts. Recent research utilising several stalagmites from along the same
685 moisture trajectory across a wide region to reconstruct oxygen isotope systematics and
686 temperature represent an exciting development in speleothem climate sciences (Deininger
687 et al., 2017; Hu et al., 2008; McDermott et al., 2011; Wang et al., 2017), and similar
688 methodologies could reveal in-cave fractionation processes that are ultimately relatable to
689 temperature, potentially on a seasonal-scale. For example, changes in outside temperature-

690 induced ventilation may affect samples fed by different hydrologies differently (promoting
691 more kinetic fractionation in slower dripping sample), and comparing the isotope ratio
692 records may reveal the range of external seasonal temperature variability. We suggest that
693 the comparison of multiple coeval stalagmite geochemical records from within the same cave
694 site is a crucial research frontier that is well worth investigating further.

695

696 **4. Analytical techniques**

697 Direct detection of seasonal variations in stalagmite geochemical parameters requires
698 sampling or analysis at sufficiently high spatial resolution to mitigate signal averaging (Figure
699 4). Sampling frequency should approach monthly resolution to detect a seasonality signal and
700 to avoid aliasing issues during intervals with slower growth. This necessitates careful
701 consideration prior to analysis to ensure both sufficient sampling resolution to detect
702 seasonal-scale variability, and sufficient material for the analytical method. In addition to
703 the pre-analysis considerations, we also recommend publishing complete micro-analytical
704 data tables, in order to increase transparency. Below we discuss common microanalytical
705 techniques capable of palaeoseasonality reconstruction and compare advantages and
706 disadvantages of each.

707

708 **4.1. Sampling for palaeoseasonality**

709 Sub-sampling stalagmites for geochemical analysis requires careful planning and execution.
710 We recommend a thorough reconnaissance of a sample's petrography using microscopy prior
711 to geochemical analysis. The conversion of a sample into polished thin sections can provide

712 critical information but is destructive. Reflected light microscopy provides [a](#) non-
713 destructive alternative that can yield crucial information regarding crystal growth habit, the
714 location of possible hiatuses, inclusions, and porosity.

715 The various methods available for the extraction of proxy data all require different sample
716 amounts depending on analytical limits of detection and other factors (Fairchild et al., 2006).
717 Methods are broadly categorizable as destructive and non-destructive, depending on the
718 amount of material required. The former is further divisible into: i) macro-destructive (e.g.,
719 cuttings for fluid inclusion studies, low-concentration proxies like biomarkers or DNA) (e.g.,
720 Blyth et al., 2011; Vonhof et al., 2006; Wang et al., 2019a), ii) meso-destructive (e.g.,
721 conventional and micro-milling for U-series samples, stable isotopes, ICP-OES, ¹⁴C) (e.g.,
722 Lechleitner et al., 2016a; Ridley et al., 2015b; Spötl and Matthey, 2006), and iii) micro-
723 destructive (e.g., laser ablation or secondary ionization mass spectrometer (SIMS) analyses
724 for traditional and non-traditional isotope systems, element concentrations or ratios) (Baldini
725 et al., 2002; Luetscher et al., 2015; Treble et al., 2007; Webb et al., 2014; Welte et al., 2016).
726 Non-destructive methods include (but are not restricted to): i) simple desktop scanning and
727 photography, ii) μ XRF line scanning and mapping (e.g., Breitenbach et al., 2019; Scropton et
728 al., 2018), iii) synchrotron analyses (e.g., Frisia et al., 2005; Vanghi et al., 2019; Wang et al.,
729 2019b; Wynn et al., 2014), iv) phosphor mapping via beta-scanning (e.g., Cole et al., 2003), v)
730 reflected light, and fluorescence, including confocal laser fluorescent microscopy (CLFM) (e.g.,
731 Orland et al., 2012) and other microscopy techniques (e.g. SEM, EMPA, RAMAN), or vi) X-ray
732 Computed Tomography (CT) scanning (e.g., Walczak et al., 2015; Wortham et al., 2019). The
733 choice of technique should consider suitability for answering the targeted research questions,
734 and logistical considerations such as sample sectioning. Although the list above categorises
735 techniques based on their destructiveness, it does not account for sample preparation; for

736 example, SIMS analysis uses only a small amount of sample (i.e., essentially non-destructive),
737 but requires sectioning of the stalagmite into centimetre-scale cubes, polishing and epoxy-
738 mounting. Another major consideration is the length of the record required; it is possible
739 (though labour-intensive) to produce seasonal-scale records extending hundreds or even
740 thousands of years using micromilling, but this is not practical using SIMS, unless automated
741 protocols allowing for unattended analysis can be developed.

742 Although macro-destructive sampling can inform interpretations based on higher resolution
743 data, it cannot generally reconstruct seasonality on its own. Thus, here we discuss only
744 selected meso-, micro-, and non-destructive techniques. The focus is first on 'conventional
745 drilling' and 'micromilling' of powder samples, which probably are the most widely used
746 techniques to obtain material for inorganic chemistry, followed by the highly versatile, fast,
747 and cost-effective laser ablation sampling (LA-ICPMS). SIMS requires substantial sample
748 preparation, offers excellent resolution and is a good choice in situations requiring in-depth
749 characterisation of a short interval. Synchrotron- μ XRF (SR- μ XRF) has advanced considerably
750 over the past decade, and it is now possible to obtain high-resolution (0.5-5 μ m) quantitative
751 trace element data non-destructively through fast scanning of large samples (Borsato et al.,
752 2019). Below we describe the relevance and applicability of these techniques towards the
753 reconstruction of palaeoseasonality.

754

755 **4.1.1. Conventional drilling**

756 Conventional drilling (or 'spot-sampling') (Fairchild et al., 2006) is the drilling of powders
757 [from discrete spots](#) that are normally separated by unsampled material, and is still
758 amongst the most widely used methods to obtain carbonate powders from speleothems. This

759 method is comparably fast and, with a sufficiently small drill bit (typical \varnothing ca. 0.2-1 mm), can
760 achieve a spatial resolution of up to 0.3-0.5 mm along the growth axis, although more
761 frequently the resolution is \sim 1 mm. Conventional drilling is ideally performed with
762 instruments that allow computer-aided control of x-y-z dimensions, such as Sherline® or
763 Mercantek® instruments.

764 With typical stalagmite growth rates of 0.1 to 0.2 mm year⁻¹, this technique is usually
765 inadequate when targeting sub-annual resolution (Figure 5). If used on samples with growth
766 rates approaching twice the sampling interval, aliasing may occur and unfavourably affect the
767 recovery of high-frequency variability (Fairchild et al., 2006). Furthermore, this type of spot
768 sampling usually does not integrate all the carbonate material, i.e. the time slices at the top
769 and bottom of the hole are under-represented in the average for the drill-hole; this
770 undersampling could miss short-lived climate excursions. Consequently, we cannot
771 recommend conventional drilling for recovering a seasonal signal, although the technique is
772 effective at quickly producing a lower-resolution record and is well suited for longer records
773 of climate (e.g., those covering multiple glacial cycles), and for screening potential target
774 stalagmites. Additionally, conventional drilling is possible on a large stalagmite slab, obviating
775 the need for sectioning into multiple smaller slabs. A related technique which is preferred for
776 sampling at seasonal scale is micromilling, discussed below.

777

778 **4.1.2. Micromilling**

779 Micromilling refers to continuous sample cutting along a trench parallel to a stalagmite's
780 growth axis (Fairchild et al., 2006; Frappier et al., 2002; Spötl and
781 Matthey, 2006). Usually performed with computer-controlled milling devices (such as the

782 ESI/New Wave micromill) this technique can achieve ~10-micron spatial resolution [e.g.](#)
783 [Ridley et al., 2015b](#), but is critically dependent on
784 the textural characteristics of the sample. Dense columnar, fascicular, radiaxial, or radial
785 fibrous calcites are the most suitable material, but needle-like aragonite can also be sampled,
786 although gaps between needle-shaped crystals may lead to loss of sample and require
787 painstaking cleaning procedures. The sample morphology throughout the stalagmite also
788 warrants consideration. Planar, parallel, and laterally continuous laminae across the sample
789 are ideal, but often stalagmite laminae appear curved in a slabbed sample. These are normally
790 convex, but in some cases are concave (particularly in the case of a 'splash' cup), and with
791 laminae that thin towards the edges. The greater such curvature, the narrower the
792 micromilling trough required for sub-annual (seasonal-scale) sampling (Figure 5), because a
793 wider trench would integrate material from other laminae. Similarly, the sample should allow
794 2-3 mm sampling into the depth of the sample slab, and ideally the growth layers should not
795 taper out in the third dimension. X-ray and Neutron CT scans can help visualise the 3D internal
796 structure of the sample (Walczak et al., 2015; Wortham et al., 2019), and the appropriate
797 milling depth.

798 The determination of the x, y, and z dimensions of the sampling increment is the first step of
799 any sampling strategy (Figure 5). For seasonal resolution, this strategy will ideally permit a
800 very small y-axis increment (the y-axis is parallel to the stalagmite growth axis). The other
801 dimensions must then allow the collection of enough carbonate for analysis (typically 50-120
802 μg for carbon and oxygen stable isotopes). Depending on sample characteristics and desired
803 resolution, dimensions of $y = 10\text{-}100 \mu\text{m}$ and $x = 10\text{-}300 * y \mu\text{m}$ (parallel to growth
804 layers on the slab) are ideal (Figure 5). The sampling depth (z-axis) is best minimised because

805 lamina behaviour into the sample is often unknown, unless CT scans of the sample exist.

806 Larger sample masses are occasionally needed for non-traditional proxies.

807 A common issue in the speleothem sciences is the precise correlation between two datasets

808 obtained via different means, for example a micromilled stable isotope dataset and a LA-

809 ICPMS derived trace element dataset. Annual- to decadal-scale correlations are usually

810 possible, but rarely are the records correlative on the seasonal- or even annual-scale.

811 Comparisons are achievable using very careful measurements from a datum (often the

812 stalagmite top), with or without the use of banding as 'landmarks' (e.g., (Johnson et al., 2006;

813 Treble et al., 2005a)). A recent technological advance is the development of software, such as

814 the open-source GIS-based QGIS software (Linzmeier et al., 2018), which integrates micro-

815 imaging and analysis into a single spatial reference frame. This approach is particularly useful

816 for organising different analyses derived from differently sectioned portions of samples and

817 has been successfully applied to stalagmite data (Orland et al., 2019).

818 The problem of correlating different types of data is to some extent avoidable by sampling

819 sufficient material with the micromill for both stable isotope and trace elemental analysis via

820 ICP-MS. The sampled powder is divided into two aliquots, one for each analytical technique.

821 The resultant trace element and stable isotope data permit zero-lag cross-correlations and

822 highly robust interpretations of different environmental processes (e.g., Jamieson et al.,

823 2016).

824 For example, if planned multi-proxy analyses require 0.8 mg of carbonate powder (e.g., stable

825 isotope ratios, ^{14}C , and trace elements), and a 50 μm spatial resolution is desired using a

826 milling bit diameter of 0.8 mm, a 0.05 mm x 4.15 mm x 1 mm trench would suffice (assuming

827 calcite density of 2.7 g/cm^3 and no sample loss via incomplete recovery); sample loss and a

828 particularly low-density sample would require a larger volume. An often-overlooked
829 additional consideration involves the corners that are initially unsampled when milling
830 trenches (red corner areas, Figure 5). Depending on the drill bit diameter and trench
831 dimensions, the corners at each end of the trench would lead to unwanted integration of
832 material from several sample increments and thus time slices. Use of a smaller milling bit
833 diameter minimizes this effect. Additionally, a 50% reduction of this sampling effect is
834 achieved if a trench is milled along the growth axis prior to the high-resolution milling, or if
835 the milled trench is adjacent to a longitudinal cut (Figure 5). Material from the first trench can
836 be used for reconnaissance studies. Another approach yielding similar results involves
837 collecting the desired powder, and then moving the milling bit along the horizontal sampling
838 track (i.e., parallel to the growth layer) for a distance corresponding to half the width of the
839 milling bit. This powder is then discarded (or collected as auxiliary powder), and the milling
840 bit returns to the original position, ready to produce the next aliquot of powder. Either of
841 these sampling approaches effectively reduce spatial integration of sample (Kennett et al.,
842 2012; Myers et al., 2015; Ridley et al., 2015b), thereby increasing the likelihood of obtaining
843 a clear seasonal signal (Figure 6). [These considerations are important because many](#)
844 [stalagmites, particularly from non-tropical localities, may have low growth rates](#) (Railsback,
845 2018)
846 [that require a very high sampling resolution with minimal integration across samples to](#)
847 [extract a seasonal signal.](#)
848 [Many samples may deviate from an idealised geometry, and may contain imperfections along](#)
849 [preferred micromilling tracks, growth rate changes, or growth axis shifts. These instances may](#)
850 [require special consideration and sample-specific solutions, such as moving to a different](#)
851 [track within the sample or changing the resolution of the analyses in response to major](#)

852 [changes in growth rate. In the case of the latter, interpretations should consider how changes](#)
853 [in sampling resolution might have affected the amplitude of any seasonal cycle.](#)

854 Other issues include growth layers that slope inward rather than geometrically perfect layers

855 Other minor issues include the possible conversion of aragonite to calcite during milling,
856 which would result in a decrease in $\delta^{18}\text{O}$ values of 0.02‰ for every 1% aragonite converted
857 to calcite (Waite and Swart, 2015). This effect may have implications for modelling oxygen
858 isotope variability or calculating deviations from equilibrium deposition. However, using a
859 slower rotation rate of the milling bit (500-800 rpm) will minimise, or even eliminate, this
860 effect. A final recommendation is to run micromilled samples through the IRMS non-
861 sequentially (i.e., out of stratigraphic order). Ideally the laboratory environment is static and
862 will not affect results, but any unaccounted for changes (e.g., lab temperature) may
863 affect the analyses in a cyclical way. Running samples non-sequentially both helps ensure
864 that any cycles detected (e.g., a seasonal cycle) are not analytical artefacts and helps to
865 identify issues, if they exist (e.g., a persistent cycle when samples are arranged in the order
866 that they were run).

868 **4.1.3. LA-ICPMS**

869 Laser Ablation Inductively Coupled Plasma Mass Spectrometry (LA-ICPMS) is a beam method
870 sampling technique. A polished speleothem slab is analysed by ablating small portions of
871 material using a laser within a sample cell. The laser (typically an ArF excimer laser at a 193
872 nm wavelength) physically ablates the sample, aerosolising the material which is then carried
873 into the ICP-MS system by a carrier gas (typically helium and/or argon, with helium yielding a

874 greater signal intensity (Luo et al., 2018)) where trace element concentrations are measured
875 and quantified against standards of known compositions. The specific mass spectrometer set-
876 up depends on the research question; for example, by using a quadrupole ICP-MS for
877 elemental measurements using a reference isotope, or a multi-collector ICP-MS for isotope
878 ratio analyses. Additional analytical set-ups are compatible with LA-ICPMS, including reaction
879 cells, triple-quadrupoles, and split-stream analysis using two mass spectrometers in tandem
880 (Frick et al., 2016; Kylander-Clark et al., 2013; Woodhead et al., 2016).

881 The advantages of LA-ICPMS for speleothem trace element analysis are numerous and include
882 excellent spatial resolution (down to ~3 microns (Müller and Fietzke, 2016)) using a
883 rectangular aperture with long axis oriented along laminae whilst preserving low detection
884 limits (Figure 6). Although historically LA-ICPMS instruments used round 'spots', some laser
885 ablation instruments are now fitted with rectangular masks (apertures), resulting in
886 rectangular spots optimised for speleothem analysis, where the ablation spot's long
887 dimension is oriented perpendicular to speleothem growth axis, along the x-axis (Müller et
888 al., 2009). This permits the ablation of a surface area equivalent to large circular spot sizes,
889 while retaining high spatial resolution in the growth direction (similar to the micromill
890 sampling described in 4.1.2). The speed of analysis via this method is also exceptionally high,
891 with typical scan speed of $10 \mu\text{m s}^{-1}$ (e.g., (Jamieson et al., 2015)). Two-volume laser cells are
892 now available, minimising sample damage incurred via sectioning and ensuring consistent
893 aerosol flow within the cell. The coupling of a laser ablation system with a large-capacity gas
894 exchange device even allows analysis under atmospheric air (Tabersky et al., 2013) although
895 with somewhat elevated limits of detection. This technique is particularly suitable for large
896 stalagmites, or archaeological samples, because it minimises physical sample destruction by
897 requiring less sectioning.

898 The presence of a localised impurity can produce a trace elemental concentration peak even
899 in the absence of a laterally contiguous geochemical horizon with that geochemistry. LA-
900 ICPMS can produce elemental maps that can verify the spatial continuity of geochemical
901 laminae of interest, particularly when combined with a square aperture (Evans and Müller,
902 2013; Rittner and Muller, 2012; Treble et al., 2005b; Woodhead et al., 2007). This permits the
903 resolution of spatial relationships with greater confidence and can
904 corroborate interpretations based on stacked and parallel line scans, thereby avoiding issues
905 related to the overinterpretation of a small number of points. Other microanalytical
906 techniques (e.g., SIMS, synchrotron, μ XRF, etc.) can also produce elemental maps, but LA-
907 ICPMS techniques can provide greater spatial coverage more rapidly.

908 The most significant disadvantage to LA-ICPMS is related to difficulties with standardisation.
909 The use of matrix matched standards (i.e., made of the same material as the sample) during
910 laser ablation analysis is ideal, but the limited availability, variable degrees of standard
911 homogeneity, and accurate standardisation of carbonate materials are ongoing challenges.
912 Orland et al. (2014) and later Müller et al. (2015) provide promising tests for a carbonate
913 standard, albeit for a limited range of elements. Many analyses are standardised with
914 somewhat greater uncertainty than is ideal using glasses such as NIST 620 or 622. These
915 analyses are often regarded as semi-quantitative, with high levels of confidence regarding
916 variability and data trends but uncertainty regarding absolute values. Another minor
917 disadvantage is lack of precise knowledge regarding the position of individual analytical spots.
918 The sheer number of analyses possible via this technique (often >10,000) and indistinct,
919 continuous track means that the exact position of any one individual spot is often difficult to
920 determine precisely, complicating the correlation with other climate proxies. This
921 disadvantage is mitigatable by precise notetaking, syn-analytical microscopy recording,

922 careful reflected light imaging, cross-correlation, application of QGIS or similar software, and
923 judicious ‘wiggle-matching’ with other proxy records, as well as creating marker laser lines at
924 certain intervals to further help to constrain spatial uncertainties.

925

926 **4.1.4. Secondary ionisation mass spectrometry**

927 Secondary ionisation mass spectrometry (SIMS) uses a primary beam of positive (often
928 caesium) or negative (often oxygen) ions to impact a sample surface under a vacuum,
929 ‘sputtering’ secondary ions into a mass spectrometer (Wiedenbeck et al., 2012).

930 The sputtered secondary ions are then accelerated into a double-focusing mass [spectrometer](#)

931 The sputtered secondary ions are then accelerated into a double-focusing mass [spectrometer](#)

932 The sputtered secondary ions are then accelerated into a double-focusing mass
933 [spectrometer and](#) counted by ion detectors (electron multiplier or Faraday

934 cup). This analytical technique can yield both trace element analysis and stable isotope ratio

935 data in speleothem carbonate at the micron scale, with very little damage to the sample, and

936 with very high sensitivity (Figure 6).

937 The spatial resolution typically ranges between 1 to 10 µm spot size and 1-2 µm spot depth

938 for trace elements, with stable isotope analyses historically restricted to 20–30 µm resolution

939 (Fairchild and Baker, 2012) but now capable of achieving 10 µm resolution (Orland et al.,

940 2019). This represents a very high-resolution method for stable isotope analysis within

941 speleothem [carbonate and](#) is therefore ideal for detecting palaeoseasonality

942 (Fairchild et al., 2006). The analytical resolution for trace elements is [lower](#)

943 [than when](#) using synchrotron radiation, but with the added advantage of full quantification

944 of concentration data and the ability to cover much greater areas of sample. Matrix matched
945 materials, typically calcium carbonate, are used for standardisation to ensure consistent
946 ionisation of chemical species and ablation rates (Fairchild and Treble, 2009).

947 Early studies of SIMS-derived trace element trends in speleothems helped to demonstrate
948 that many stalagmites retained a seasonal signal (Baldini et al., 2002; Finch et al., 2001;
949 Roberts et al., 1998), representing a considerable shift in resolving power compared to the
950 former decadal- to centennial-scale of analysis previously possible. The presence of annual
951 trace element cycles was quickly established as the norm rather than the exception for
952 shallow cave sites, even in the absence of visible speleothem laminations (Fairchild et al.,
953 2001). Divalent alkaline earth metals such as magnesium and barium were suggested as
954 palaeohydrological proxies, phosphorus as indicative of bioproductivity, and strontium as
955 reflecting calcite growth rate and/or PCP (Fairchild et al., 2001; Fairchild et al., 2000; Treble
956 et al., 2003). However, the need for better empirical transfer functions between speleothems
957 and external climatic processes, and partitioning between drip waters and speleothem
958 calcite, complicated interpretations (Fairchild et al., 2001). Subsequent process-based studies
959 have revealed the complexity involved in interpreting trace elements at seasonal scales,
960 highlighting the role they play in complexation with organic matter as colloids (Borsato et al.,
961 2007), in speleothem diagenesis (Martin-Garcia et al., 2014), and the complex controls on
962 transfer through vegetation/soil/epikarst (Hartland et al., 2009; Hartland et al., 2012), as well
963 as controls on partitioning via internal cave microclimate and crystallographic structures
964 (Fairchild and Treble, 2009). The use of trace element cycles obtained via SIMS as
965 chronological markers is exemplified through the work of Smith et al. (2009), where the ability

966 of trace element cycles to provide relative age constraints at a finer spatial resolution than
967 traditional U-series age models is unambiguously demonstrated.

968 A frontier for SIMS trace element measurements lies in the potential of combining these trace
969 element records with stable isotope measurements undertaken at sub-annual scale. Prior to
970 the advent of SIMS techniques for stable isotope analysis, there were very few combined
971 trace element – stable isotope studies due to the incompatibility of analytical resolution
972 between the two parameters (Orland et al., 2014). However, the analysis of stable isotopes
973 by SIMS now achieves a spatial resolution capable of allowing direct comparability between
974 both isotopic and trace element indicators of seasonality (Orland et al., 2014).

975 SIMS stable isotope studies have investigated the $\delta^{18}\text{O}$, $\delta^{13}\text{C}$ and $\delta^{34}\text{S-SO}_4$ dynamics in
976 stalagmite records (typical uncertainties (2σ): $\delta^{18}\text{O} = 0.2\text{‰}$ (Orland et al., 2019); $\delta^{13}\text{C} = 0.6$ –
977 0.7‰ (Oerter et al., 2016; Sliwinski et al., 2015); $\delta^{34}\text{S} = 1.6\text{‰}$ (1σ) at 70 ppm S concentrations
978 (Wynn et al., 2010)). Whereas each of these isotope ratios reflects changing surface
979 environmental conditions over inter-annual timescales, only the $\delta^{18}\text{O}$ measurements by SIMS
980 can produce records of intra-annual seasonality. Analysis of $\delta^{13}\text{C}$ in speleothem carbonate
981 cannot be undertaken simultaneously with $\delta^{18}\text{O}$, and any available records in the literature
982 (e.g., (Pacton et al., 2013)) are not undertaken at seasonal resolution. The apparent lack of
983 seasonal change in cave dripwater $\delta^{34}\text{S-SO}_4$ (Borsato et al., 2015) has also so far prevented
984 SIMS speleothem sulphur isotope measurements at the seasonal scale (Wynn et al., 2010).
985 Treble et al. (2005a) produced the first $\delta^{18}\text{O}$ record unambiguously linking seasonal cycles in
986 speleothem oxygen isotopes to rainfall [dynamics and](#) corroborated these
987 interpretations with trace element cycles and contemporary rainfall monitoring. Subsequent
988 work at Soreq Cave (Israel), further developed the technique to detect seasonality and links

989 with rainfall dynamics across a range of time periods (Orland et al., 2012; Orland et al., 2009;
990 Orland et al., 2014). Coupled annual variability in fluorescence and $\delta^{18}\text{O}$ provided a seasonal
991 marker of annual variability in rainfall from before the climate instrumental record (Orland et
992 al., 2012; Orland et al., 2009). Careful correlation between fluorescent banding, $\delta^{18}\text{O}$ and
993 trace element measurements, and surface environmental conditions demonstrated that the
994 fluorescent banding represented seasonal organic colloid flux variability into the cave.

995 Despite the clear advantages of utilising SIMS stable isotope analyses of speleothem
996 carbonate to reveal seasonal patterns of rainfall delivery and drivers of climatic change, the
997 technique also comes with its analytical challenges, including the considerable impact of
998 geometric imperfections (e.g., sample topography, porosity, inclusions, cracks, etc) (Kita et
999 al., 2011; Liu et al., 2015; Pacton et al., 2013; Treble et al., 2005a)
1000 . In most instances, the ability to control the precise location of SIMS analyses
1001 enable geometric imperfections to be avoided, provided [that i](#)) good surface mapping can be
1002 used to identify optimal locations for analysis and [that ii](#)) post-processing can
1003 [visualise](#) geometric imperfections in each analysis pit (Orland et al., 2009). This
1004 [contrasts with](#) micromilling, where large swathes of sample are often bulked
1005 together regardless of sample porosity or imperfections. The need to use matrix matched
1006 standard materials presents similar problems of availability and homogeneity for the accuracy
1007 of data analysis as encountered with LA-ICPMS. However, recent improvements in this area,
1008 alongside improvements in sample preparation techniques have been substantial enough to
1009 enable accurate correction for instrumental drift (Valley and Kita, 2009). The impact of trace
1010 element content on carbonate $\delta^{18}\text{O}$ and $\delta^{13}\text{C}$ analyses also requires careful consideration
1011 (Sliwinski et al., 2017), but can be corrected following careful standardisation and is generally

1012 not a problem encountered through speleothem analysis where the trace element content is
1013 typically less than 1 weight %. An emerging analytical frontier concerns the impact of water
1014 and/or organic content on SIMS carbonate $\delta^{18}\text{O}$ and $\delta^{13}\text{C}$, requiring careful pre-screening of
1015 sample material and simultaneous analysis of OH- and CH- respectively
1016 (Orland et al., 2015; Orland et al., 2019; Orland, 2013; Wycech et al., 2018).
1017 (Orland et al., 2015; Orland et al., 2019; Orland, 2013; Wycech et al., 2018).
1018 (Orland et al., 2015; Orland et al., 2019; Orland, 2013; Wycech et al., 2018).
1019 Despite these issues, SIMS remains an appealing choice for palaeoseasonality reconstruction
1020 using stalagmites due to its sensitivity and resolution. SIMS has produced some of the highest
1021 resolution records of palaeoseasonality available and will continue to play an important role
1022 in linking stalagmite records to seasonal changes in environmental conditions, particularly
1023 across discrete, short-lived events. Although the technique is not suitable for building long
1024 records, the comparison of discrete timeslices permits seasonality to be contrasted for key
1025 intervals (Orland et al., 2012; Orland et al., 2015; Orland et al., 2019).

1026

1027 **4.1.5. Synchrotron**

1028 The application of Synchrotron Radiation micro X-Ray Fluorescence (SR- μ XRF) to the study of
1029 speleothem carbonate opened up new possibilities in terms of greater resolving power for
1030 geochemical analysis (Kuczumow et al., 2003; Kuczumow et al., 2001). Based on the emission
1031 of electromagnetic radiation from charged electrons accelerated in an orbit, synchrotron
1032 radiation generates secondary radiation from speleothem carbonate based on the
1033 characteristic fluorescent properties of chemical elements. The excellent spatial resolution of

1034 analysis (0.5–5 microns), low detection limits, low background, and the ability to
1035 quantitatively map trace element variability across a given area has enabled the study of
1036 speleothem geochemical structures at the sub-annual timescale and in two dimensions
1037 (Figure 6). The use of XANES (X-Ray Absorption Near Edge structure) can define the oxidation
1038 state of the element under consideration, thereby adding further resolving power to
1039 determine environmental processes.

1040 Applications range from using SR- μ XRF to determine long-term (100 year) secular changes in
1041 elemental signals (Frisia et al., 2005), high resolution event imaging across sub-annual to
1042 multi-annual timescales (Badertscher et al., 2014; Frisia et al., 2008; Vanghi et al., 2019; Wang
1043 et al., 2019b), and for investigating petrological controls on geochemical composition (Frisia
1044 et al., 2018; Ortega et al., 2005; Vanghi et al., 2019). However, it is at the seasonal scale of
1045 analysis where the resolving power of synchrotron radiation has really pushed the boundaries
1046 of speleothem science.

1047 No conventional dating technique provides an absolute timeframe at the sub-annual scale of
1048 speleothem carbonate deposition. However, linking the seasonality of external
1049 environmental processes to speleothem petrology and geochemical characteristics can yield
1050 a monthly scale resolution of trace element content. SR- μ XRF was used to determine the
1051 coincidence of trace element distributions and physical calcite characteristics within annual
1052 stalagmite laminations (Borsato et al., 2007). Based on the annually laminated stalagmite
1053 ER78 from Ernesto Cave, Italy, a suite of trace elements (P, Cu, Zn, Br, Y, and Pb) were found
1054 to form an annual peak, coincident with a characteristic thin (0.5-4 μ m) brown UV-fluorescent
1055 layer in each annual couplet. The brown colouration of each UV-fluorescent layer is probably
1056 due to organic acids derived from high rates of water infiltration during each autumn (Frisia

1057 et al., 2000; Huang et al., 2001; Orland et al., 2014). The transport of trace elements is
1058 associated with colloidal organic molecules (Hartland et al., 2010; Hartland et al., 2012), and
1059 leads to the incorporation of this distinctive elemental suite on a seasonal basis associated
1060 with the autumnal rains (the 'autumnal pulse' as described in Section 2.4). SR- μ XRF permits
1061 the detection of variability inherent to each individual year, which then can be contrasted
1062 against the symmetrical mean annual profile. Any differences (e.g., double peaks or shoulder
1063 peaks) provide an indication that the rainfall distribution throughout that year deviated from
1064 the mean annual profile. Strontium was observed to vary inversely to colloiddally transported
1065 elements (Borsato et al., 2007), possibly due to competition for binding to defect sites, thus
1066 limiting incorporation into the calcite lattice. SR- μ XRF revealed seasonal patterns of zinc, lead,
1067 phosphorus, and strontium within speleothem Obi84 from Obir Cave, Austria, whose
1068 concentration peaks also coincided with the dark coloured visible laminae. These were
1069 similarly interpreted as hydrological event markers associated with autumnal
1070 [infiltration but](#) could also result from dry deposition of aerosols (Dredge et al., 2013).

1071 SR- μ XRF 2D mapping within speleothem Obi84 over three annual cycles demonstrated the
1072 effects of several infiltration events each year, present as short-lived peaks in Zn
1073 concentration and which build in magnitude towards the main autumnal flush (Wynn et al.,
1074 2014) (Figure 6). Using these event peaks as markers of autumnal flushing permitted
1075 attribution of annual sulphate cycles to summer high and winter low concentrations. At the
1076 Obir Cave site, these seasonal shifts in speleothem sulphate content were attributed to
1077 temperature-driven cave ventilation and associated cave air $p\text{CO}_2$ variability which controlled
1078 the dripwater pH and the sulphate:carbonate ratio. Wynn et al. (2018) later verified this
1079 proposed seasonal mechanism using controlled laboratory experiments, thereby permitting
1080 the extraction of seasonal temperature information based on the annual sulphate cycle's

1081 topology. SR- μ XRF can thus extract geochemical expressions of seasonality, and the technique
1082 is well-suited to investigating changing rainfall and temperature seasonality dynamics back
1083 through time.

1084

1085 **4.1.6. Data analysis**

1086 Following the geochemical analyses and data processing, the information must be
1087 interpreted. For techniques producing tens to hundreds of data points, this is not particularly
1088 challenging. On the other hand, techniques such as LA-ICPMS can produce tens of thousands
1089 of data points for multiple [elements and](#) can greatly increase the processing
1090 time on common spreadsheet programmes. To circumvent these issues, it is possible to
1091 simplify the data using a Principal Component Analysis (PCA), a multivariate statistical analysis
1092 technique which extracts modes of variation from large multivariate timeseries datasets that
1093 best describe overall variability of those datasets. The technique is ideal for large multivariate
1094 stalagmite-derived LA-ICPMS datasets (Borsato et al., 2007; Jamieson
1095 et al., 2015; Orland et al., 2014; Wassenburg et al., 2012). PCA has also been used to extract
1096 a seasonal signal from trace elemental concentrations even in the absence of visible laminae
1097 and applied towards the development of a chronology (Ban et al., 2018).

1098 Comparing the intra-annual amplitude of a geochemical signal (Orland et al., 2012; Orland
1099 et al., 2009; Orland et al., 2014; Orland et al., 2019) from monthly-resolved datasets is ideal
1100 for extracting seasonal information from an otherwise difficult to interpret dataset. For
1101 example, Ridley et al. (2015b) used the well-developed annual carbon isotope cycles with
1102 their Belizean stalagmite to extract seasonal amplitudes, which were then interpreted in
1103 terms of the strength of the seasonal ITCZ incursion into southern Belize. Orland et al.

1104 (2015) used the topology of oxygen isotope variability within individual growth bands in a
1105 Chinese stalagmite to clarify the origin the oxygen isotope variability. Spectral analysis of
1106 well-dated samples can also reduce data complexity (Myers et al., 2015;
1107 Ronay et al., 2019). For example, Asmerom et al. (2020) used a wavelet analysis to
1108 reconstruct the strength of the wet season in Central America over the last two millennia,
1109 and to show that modern seasonality in rainfall was only emplaced in the 15th Century.
1110 Extracting a meaningful metric from numerous more complex data using statistical
1111 techniques is one way of simplifying a complex geochemical dataset.

1112

1113 **5. Modelling techniques**

1114 [There have been many](#) efforts at modelling both the hydrology feeding a stalagmite and
1115 the climate signal within. Proxy system models (PSMs) describe how geological or
1116 chemical archives are imprinted with [a](#) climate signal (Evans et al., 2013). In terms of
1117 stalagmite-specific models, several exciting geochemical models now exist which can explore
1118 the emplacement of a geochemical signal in a stalagmite (Wong and Breecker, 2015), often
1119 based on established processes which govern stalagmite precipitation (e.g., (Buhmann and
1120 Dreybrodt, 1985)). Two recent examples (specifically of disequilibrium isotope fractionation
1121 processes proxy system models) are the IsoCave model, which can examine disequilibrium
1122 isotope effects in speleothems and related implications for speleothem isotope thermometry
1123 (Guo and Zhou, 2019), and the ISOLUTION model which similarly helps to better understand
1124 the effect of these disequilibrium isotope fractionation processes on stalagmite proxy records
1125 (Deininger and Scholz, 2019). The I-STAL model allows the simulation of PCP and how this
1126 affects dripwater Mg, Sr, and Ba (Stoll et al., 2012). [Numerous](#) models looking

1127 specifically at drip hydrology now exist (e.g., KarstHydroModel (Baker and Bradley, 2010;
1128 Treble et al., 2003)), and these are extremely useful for understanding how the rainfall input
1129 signal is transformed before reaching the stalagmite. Rather than using hydrological or
1130 geochemical modelling, a recent publication introduced a Monte Carlo approach to model
1131 rainfall and temperature seasonality in a stalagmite from La Garma Cave, northern Spain, over
1132 the Holocene (Baldini et al., 2019). Here, we build [a second generation of this](#)
1133 [model](#) and compare [results to](#) both synthetic and real-world input data
1134 [. Whereas the older version of the model could only run a limited](#)
1135 [number of simulations and a run stopped once the model converged upon a](#)
1136 [solution \(though it could be run multiple times\), this next generation model is able to run a](#)
1137 [large number \(user-defined; we used 1,000 simulations in the runs presented here\) of](#)
1138 [simulations and retain the output of each one, permitting the creation of probability](#)
1139 [distributions for each timeslice.](#)

1140 [This new](#) model requires some widely available types of input data, including: i) a stalagmite-
1141 based $\delta^{18}\text{O}$ record, ii) a record of regional mean annual temperature (MAT) of any resolution
1142 (e.g., borehole, marine sediments, stalagmite fluid inclusions) over the interval of interest, iii)
1143 monthly-scale modern instrumental records of rainfall and temperature above the site (or as
1144 close as possible to the site), and iv) cave air temperature and its relationship with above
1145 ground temperature. The relationship between meteoric precipitation $\delta^{18}\text{O}$ and temperature
1146 at the site is useful but not required information because regional or global meteoric
1147 precipitation $\delta^{18}\text{O}$ and temperature equations can provide a suitable alternative.

1148 Essentially, the model assumes that the MAT of the cave site is similar to the MAT of the
1149 regional [surface](#) temperature input record (ii above) [and](#) produces a sine function

1150 around this value of an amplitude reflecting modern [surface](#) temperature seasonality but with
1151 random variability added to the absolute minimum and maximum temperatures (the amount
1152 of randomness is user-defined). A second sine function reflects the rainfall seasonality, and
1153 whereas the temperature wave's polarity is fixed (i.e., summers are always warmer than
1154 winters), the rainfall seasonality sine wave's polarity is allowed to flip randomly ([but where
1155 only outputs that 'converge' are retained, and unrealistic results are rejected – see below](#)).
1156 The seasonal extreme values (['extreme' meaning minima and maxima](#)) associated with either
1157 sine function are fixed to the same calendar months, linked to the timing of the modern
1158 minima and maxima.

1159 These two sine waves produce synthetic monthly temperature and rainfall values, which are
1160 then converted to $\delta^{18}\text{O}_p$ based ideally on local temperature-rainfall $\delta^{18}\text{O}$ relationships, or in
1161 cases where this relationship is not known, to more global equations (e.g., (Schubert and
1162 Jahren, 2015)). It is assumed that the $\delta^{18}\text{O}_p$ is conveyed to the dripwater (see discussion
1163 regarding evapotranspiration, Section 4.3) and that this is converted to carbonate $\delta^{18}\text{O}$ using
1164 the Tremaine equation (Tremaine et al., 2011) at ambient cave air temperature adjusted
1165 according to observed relationships between outside and inside air. This equation was chosen
1166 as most appropriate because its empirical nature accounts for in-cave disequilibrium
1167 fractionation processes more completely than other equations. The model therefore
1168 considers seasonal changes in rainfall but is independent of total annual rainfall. The annual
1169 amount-weighted mean modelled carbonate $\delta^{18}\text{O}$ value is then compared with the actual
1170 measured carbonate $\delta^{18}\text{O}$ value, and if it is within a certain user-defined value, it is logged as
1171 a successful simulation. If the difference between the modelled and actual carbonate $\delta^{18}\text{O}$ is
1172 greater than this value (generally ~ 0.1 per mil), the simulation is logged as unsuccessful. 1,000

1173 of these coupled temperature and rainfall simulations are conducted per time slice, all the
1174 successful and unsuccessful simulations are logged, and the mean monthly modelled rainfall
1175 and temperature values calculated from the successful simulations. [For a table describing the](#)
1176 [steps in the modelling process, please see Baldini et al. \(2019\).](#)

1177

1178 **5.1 Test Runs: Gradual shifts in rainfall polarity**

1179 [In this section we test the ability of the second-generation model to extract seasonality](#)
1180 [information using synthetic data.](#) The model reproduces shifts in rainfall polarity in synthetic
1181 datasets well (Figure 7). In one experiment, the input $\delta^{18}\text{O}$ dataset was created by using i) a
1182 temperature sine function that was set as invariant (i.e., it maintained its polarity and
1183 amplitude throughout the run), and ii) a rainfall sine function that shifted in polarity
1184 completely over 14 model years. [The input sine waves were used to create the annually-](#)
1185 [resolved synthetic \$\delta^{18}\text{O}\$ record but were independent from the sine waves generated by the](#)
1186 [model.](#) The wettest month in the input rainfall record was April in Year 1, gradually changing
1187 polarity to November by Year 14. As such, model Year 7 was characterised by no seasonality
1188 (Figure 7). The model was run without *a priori* knowledge of these shifts other than the mean
1189 annually-resolved synthetic $\delta^{18}\text{O}$ record, MAT, ‘modern’ seasonality range, and cave
1190 temperature (i.e., the simulations were run ‘modeller blind’), but the output reproduced the
1191 shifting rainfall pattern very well. The gradual shift in rainfall polarity is detected, and the lack
1192 of seasonality in the input rainfall signal during Year 7 is reproduced. The input temperature
1193 data had a 15 °C annual temperature range, and two model simulations were conducted: one
1194 derived using an annual seasonal temperature range of 10 ± 6 °C, and a second using an
1195 annual seasonal temperature range of 15 ± 6 °C. In the case of the lower annual temperature

1196 range, the model overestimates rainfall seasonality to compensate for the inappropriate
1197 annual temperature range, but still detects shifts in rainfall polarity (Figure 7). When the more
1198 appropriate temperature range is used, the simulation captures both the amplitude and
1199 polarity of the shifting rainfall input signal. However, this experiment highlights a limitation
1200 of this modelling approach; $\delta^{18}\text{O}$ data is explicable both in terms of rainfall and temperature
1201 seasonality shifts, and an unknown annual temperature range introduces uncertainties.

1202 A second experiment involved synthetic temperature and rainfall input records with both
1203 considerable inter-annual variability and noise introduced (Figure 8). Notably, one model year
1204 (Year 4) had the polarity of the rainfall signal completely reversed. Again, the model was able
1205 to extract the salient features of the input data very well. Reproduced were inter-annual
1206 variations in rainfall and temperature, and, importantly, the model detected the reversed
1207 seasonality of the rainfall signal in Year 4 (Figure 8).

1208

1209 **5.2 Application to a stalagmite $\delta^{18}\text{O}$ dataset from a seasonally arid continental region**

1210 The first version of the model was run successfully across the Holocene using a $\delta^{18}\text{O}$ dataset
1211 derived from the maritime climate of northern Spain (Baldini et al., 2019). Here, we apply the
1212 [second-generation](#) model to a dataset from Bir-Uja Cave in the Keklik-Too mountain ridge,
1213 Kyrgyzstan, a location characterised by extremely strong seasonal fluctuations in both
1214 temperature and rainfall. The cave (40°29'N, 72°35'E) is ~60 m long and is developed at an
1215 altitude of ~1,325 m above sea level (Fohlmeister et al., 2017). The input data consisted of
1216 the $\delta^{18}\text{O}$ dataset from stalagmite Keklik1 reported on in Fohlmeister et al. (2017), a 500-year
1217 long, centennial-resolution borehole temperature record from the Tian Shan mountains

1218 (~461 km to the north of the cave site) (Huang et al., 2000), instrumental precipitation and
1219 temperature records since 1880 C.E. from Tashkent, Uzbekistan (~300 km to the east) (Menne
1220 et al., 2012), and cave temperature (Fohlmeister et al., 2017). The $\delta^{18}\text{O}$ input data were
1221 decadal-resolved, and the stalagmite was dated using a recently developed radiocarbon
1222 technique (Fohlmeister and Lechleitner, 2019; Fohlmeister et al., 2017; Lechleitner et al.,
1223 2016b). The Keklik1 record extends from 2011 C.E. back to 1150 C.E., but the borehole record
1224 only extends back to 1500 C.E., so the interval modelled only extends to 1500 C.E. On average,
1225 the site receives ~450 mm of precipitation per year (based on Global Network of Isotopes in
1226 Precipitation data from Tashkent), with ~80% falling from November to April. Summers are
1227 very dry, with August (the driest month) receiving ~5 mm of rainfall. Monthly temperatures
1228 range from -1.4 °C in January to 25.0 °C in July, with a MAT of 12.1 °C. Stalagmite Keklik1 was
1229 located ~40 meters from the cave entrance and was collected in October 2011. Cave
1230 temperature varies seasonally, from 12 °C from the end of November until April, to a
1231 maximum of 16.5 °C in May. The site is characterised by near 100% relative humidity in the
1232 cold season which drops considerably to ~60% during the warmer months (Fohlmeister et al.,
1233 2017).

1234 Unlike the Spanish GAR-01 record which extended back to ~13,500 years BP and was
1235 modelled using 100-year timeslices (Baldini et al., 2019), the Keklik1 $\delta^{18}\text{O}$ record was
1236 modelled using annual timeslices. The duration of the timeslice is user-defined and is
1237 independent of the resolution of the original stalagmite $\delta^{18}\text{O}$ dataset, but a timeslice with a
1238 somewhat higher resolution than the $\delta^{18}\text{O}$ dataset ensures that the input data are entirely
1239 represented. The timings of the minimum and maximum values of the modelled temperature
1240 sine function were fixed at January and July, respectively. These months were also designated

Formatted: Font: Symbol

Formatted: Superscript

1241 as the minimum/maximum of the modelled rainfall sine wave, which fits present day
1242 observations, but the sine function's polarity was not prescribed in advance.

1243 Baldini et al. (2019) noted that the modelled temperature curve for northern Iberia closely
1244 resembled a previously published temperature reconstruction for the region (Martin-Chivelet
1245 et al., 2011) with a temporal resolution that exceeded the information provided by the low-
1246 resolution input dataset. Although no annual-scale MAT record exists in the Kyrgyzstan region
1247 for the last 500 years, summer temperatures are well constrained by tree ring records. A
1248 comparison of the modelled July temperature derived from the Keklik1 $\delta^{18}\text{O}$ record reveals a
1249 very good match with the NTREND AG2 temperature anomalies (~300 km to the north of the
1250 cave site) (Anchukaitis et al., 2017; Cook et al., 2013) (Figure 9). The model's ability to
1251 reconstruct palaeotemperature may reflect the fact that the probability of a successful model
1252 run is maximised when modelled temperature approximates the actual temperature shift.
1253 Successful model runs with a different (and incorrect) temperature pattern are possible with
1254 certain modelled rainfall simulations, but the mean monthly temperature values (reflecting
1255 the mean of all successful runs) will be biased towards model simulations with the correct
1256 temperature shift. The apparently robust reconstruction of warm-season palaeotemperature
1257 is an unexpected and exciting model outcome, but one that requires further evaluation.

1258 The rainfall reconstruction reproduces many of the same features highlighted by Fohlmeister
1259 et al. (2017). In particular, decreases in the winter rainfall contributions in the late 1500s, the
1260 mid-1700s, and the early 1800s are apparent in both records.

1261 [This agreement](#) is expected because the $\delta^{18}\text{O}$ record is integral to both reconstructions,
1262 [but](#) it is interesting that the two reconstructions use two fundamentally different techniques
1263 (numerical versus geochemical modelling) to estimate the importance of winter rainfall to the

1264 overall annual water budget at the [site and](#) arrive at broadly similar results. For example, a
1265 winter rainfall peak occurs in 1797 CE in both records and transitions to drier winters by 1815
1266 CE, with ~22% and ~50% reductions in winter rainfall implied by the model and $\delta^{18}\text{O}$ data,
1267 respectively. The model underestimating the reduction in rainfall probably arises because of
1268 the model's utilisation of smooth sine waves rather than more step-like functions; in other
1269 words, although it is possible for one month per year to have zero rainfall in the model, the
1270 adjacent two months must necessarily have some rainfall, whereas in reality, several dry
1271 months per summer could occur. The use of step functions would permit the incorporation
1272 of several dry months annually and would amplify apparent shifts in seasonal rainfall
1273 amounts. Modelled DJFM rainfall compares reasonably well with GHCN rainfall from Tashkent
1274 (Figure 9), particularly considering that the Tashkent meteorological station is ~300 km away
1275 from and ~1,000 m lower in altitude than the cave site.

1276

1277 **5.3 Limitations to the modelling technique and future work**

1278 Several limitations to the presented modelling technique exist. First, the timing of the rainfall
1279 minima and maxima versus temperature signal could affect the model's efficacy; for example,
1280 if the rainiest month occurs three months after (or before) the warmest month, the use of
1281 the sine function means that all outcomes are possible. This is because the maxima/minima
1282 in one parameter's sine function occur at the nodes of the other sine wave, effectively making
1283 both sine waves independent of each other. At many sites, temperature and rainfall are
1284 intrinsically linked and their seasonal cycle broadly synchronous, but the above may be an
1285 issue at some locations. Additionally, the model would require a differently shaped rainfall-

1286 function to model rainfall at locations with two distinct rainy intervals every year, such as low
1287 latitude sites affected by the ITCZ twice each year.

1288 The current version of the model does not incorporate evapotranspiration, and this is an
1289 obvious oversimplification. This may have repercussions for sites like Kyrgyzstan that
1290 experience a pronounced hot and dry season with negative effective infiltration. Similarly,
1291 variable kinetic fractionation almost certainly occurred within the cave (Fohlmeister et al.,
1292 2017) but is not considered within the model. Future versions of the model will incorporate
1293 both evapotranspiration and kinetic effects, but the model currently likely overcomes this
1294 limitation simply by reducing rainfall amount for months with high evapotranspiration rates.
1295 Potentially, coupling the new model discussed here with a dripwater isotope evolution model
1296 (e.g., ISOLUTION (Deininger and Scholz, 2019)) could produce very robust results. The model
1297 also cannot identify intervals characterized by changes in moisture pathway or fractionation
1298 amount; rather, it highlights intervals that are not explicable in terms of changes in
1299 temperature or rainfall amount seasonality (intervals where the model cannot converge on
1300 any solutions), and thus points to the involvement of other processes.

1301 The model is allowed to randomly vary MAT above or below the low-resolution temperature
1302 input record, but only within user-defined bounds. Too great a range of permissible MAT
1303 values would allow essentially any outcome. For example, if there were no limits to minimum
1304 winter temperature, a low $\delta^{18}\text{O}$ value could be modelled as either a very cold winter with a
1305 subdued rainfall seasonality or as a mild winter but with substantial winter rain. Limiting the
1306 temperature seasonality to reasonable bounds (for example, based modern interannual MAT
1307 variability) permits assessing whether any given month is warmer or colder than the low-
1308 resolution temperature input, but may underestimate the total amount of cooling and

1309 warming. In extreme cases, this may manifest itself as a failure to converge upon any
1310 successful model, thus highlighting timeslices that require closer inspection and potentially
1311 an alternative explanation.

1312 As discussed in Section 5.2, the utilisation of step functions to describe rainfall seasonality
1313 may facilitate the modelling of climate for sites where several months receive similar amounts
1314 of rainfall. Future studies should investigate the ramifications of function choice on output.
1315 Additionally, theoretically arriving at a mathematical solution utilising the relevant equations
1316 and input data is possible, obviating the need for MC simulations, and future research will
1317 investigate this possibility. Finally, future models could incorporate options for geochemical
1318 modelling of drip and carbonate chemistry.

1319

1320 **6. Regional seasonality**

1321 In this section we analyse global meteoric precipitation and temperature data to highlight
1322 regions experiencing pronounced seasonal variability in temperature, precipitation amount,
1323 and precipitation $\delta^{18}\text{O}$ (Figures 10 and 11), helping to facilitate the identification of cave sites
1324 sensitive to seasonality. This also highlights locations that are at the margins of such regions,
1325 where seasonality may have affected the record in the past, despite the lack of a modern
1326 influence.

1327

1328 **6.1. Identification of seasonally sensitive regions**

1329 WorldClim Version 2 data were obtained at a 2.5 minute (~4.5 km at the equator) spatial
1330 resolution (Fick and Hijmans, 2017). Inland continental regions within the mid- to high-
1331 latitudes of the Northern Hemisphere (e.g., central and northern Canada, eastern Russia,
1332 northeast China, and Mongolia) are characterised by the greatest mean annual temperature
1333 range (Figure 10a). A greater annual temperature range is characteristic of continental
1334 climates due to the reduced oceanic influence, with ocean water's high heat capacity and
1335 moderating influence on air temperature. The lowest mean annual temperature ranges occur
1336 in the low latitudes (where insolation remains high year-round) and maritime regions of the
1337 world (where oceans moderate temperature variability) (Figure 10a). The pattern of global
1338 temperature seasonality (herein calculated as the maximum temperature of the warmest
1339 month minus the minimum temperature of the coldest month averaged over the period 1970
1340 – 2000 based on WorldClim Version 2 data) is consistent with the geographic pattern of cave
1341 air ventilation reported in (James et al., 2015), a study concerning the role of outside
1342 temperature seasonality in the seasonal ventilation of caves.

1343 Seasonality in precipitation amount (Figure 10b) is greatest in the low latitudes due to the
1344 annual migration of the Intertropical Convergence Zone (ITCZ) and monsoonal systems that
1345 cause distinct wet and dry seasons, along the western coast of North America, southern South
1346 America, and Europe where seasonal westerlies preferentially bring enhanced winter
1347 precipitation, and bordering the Mediterranean where a 'Mediterranean climate'
1348 characterised by wet-winters and dry-summer dominates (Figure 10b). The lowest
1349 precipitation amount seasonality occurs in arid and semi-arid regions of the world and the
1350 non-coastal mid- to high-latitudes of the northern and southern hemispheres.

1351 Global seasonality in amount-weighted $\delta^{18}\text{O}_p$ (Figure 11) approximates the pattern of
1352 temperature seasonality (Figure 10a), with the greatest annual range in $\delta^{18}\text{O}_p$ observed at
1353 Northern Hemisphere continental interior and high latitude sites (e.g., northeast Asia, central
1354 Canada, northern Greenland). In addition, high altitude sites (e.g., the Andes in western South
1355 America, the Caucasus Mountains at the intersection of Europe and Asia) also exhibit higher
1356 annual WM $\delta^{18}\text{O}_p$ ranges due to the altitude effect. The lowest $\delta^{18}\text{O}_p$ seasonality occurs within
1357 maritime (e.g., NW Europe, SW and SE Australia) and arid/semi-arid regions (e.g., East Africa,
1358 eastern Brazil, South Africa). Many stalagmite records are from temperate regions where
1359 modern MAT ranges from 10 to 16 °C (Baldini et al., 2019; Baldini et al., 2015; Ban et al., 2018;
1360 Huang et al., 2001; Johnson et al., 2006; Orland et al., 2014). Global cave dripwater $\delta^{18}\text{O}$ data
1361 reveal that caves from regions with this MAT range have dripwater chemistry that reflects
1362 recharge-weighted $\delta^{18}\text{O}_p$ (Baker et al., 2019). The seasonal distribution of $\delta^{18}\text{O}_p$ is therefore a
1363 critical control in the case of many different stalagmite samples.

1364 In other cases, very pronounced seasonality inherent in stalagmite geochemical records are
1365 not due to seasonality in $\delta^{18}\text{O}_p$, but instead to seasonality in rainfall amount (Ridley et al.,
1366 2015b) and associated shifts in bioproductivity (Baldini et al., 2005) or PCP (Fairchild and
1367 Hartland, 2010; Fairchild et al., 2006). Seasonality in temperature can also induce cave
1368 ventilation in temperate zone caves during the winter (providing the cave geometry is
1369 appropriate), promoting carbonate deposition within the cave and biasing annual- to decadal-
1370 scale records towards the winter season rainfall (James et al., 2015). The maps provided
1371 herein can help identify regions containing speleothems retaining the desired seasonal signal,
1372 and determine what the most likely control is on any seasonal signal found within a
1373 stalagmite. Furthermore, the maps help highlight cave sites that are located on the

1374 peripheries of climatologically seasonal zones at present, where past seasonality shifts could
1375 have influenced a record. Examples include the Sahel and southern Belize (Figure 12), both
1376 currently at the very northern extent of the ITCZ, where a small ITCZ shift to the south would
1377 produce both severe drying and a substantial decrease in rainfall seasonality. This perspective
1378 was underscored by recent results from Central America that used monthly-scale rainfall
1379 proxy data over the last two millennia to suggest that the region has only been affected by
1380 the ITCZ since ~1400 C.E., and that the ITCZ influence may wane in the near future (Asmerom
1381 et al., 2020) (Figure 12).

1382

1383 **6.2. Complexities despite strong seasonality: northeast India as an example**

1384 The seasonality maps presented here highlight regions most likely to contain stalagmites
1385 which retain seasonal signals in temperature, rainfall amount, or $\delta^{18}\text{O}_p$. However, they also
1386 illustrate that not all seasonal variations in $\delta^{18}\text{O}_p$ are explicable in regional temperature or
1387 rainfall amount terms. In many cases, complex moisture source variability overprints
1388 temperature-induced seasonality, hampering the use of models such as the one presented in
1389 Section 5. Here, we discuss the Indian Summer Monsoon (ISM) as an example of such a
1390 situation, and focus specifically on Mawmluh Cave in Meghalaya, northeast India, one of the
1391 most seasonal locations on Earth in terms of rainfall amount (Fig. 10). In Meghalaya,
1392 hydroclimate is characterised by extreme seasonality, as the plateau constitutes the first
1393 topographic barrier for moisture-laden air masses travelling inland from the Bay of Bengal
1394 (Murata et al., 2007; Prokop and Walanus, 2003). At present, the ISM brings ~80% of the
1395 annual rainfall to the cave site, inducing extreme amounts of rainfall (up to 12 meters per
1396 year (Breitenbach et al., 2015). The seasonal precipitation cycle is reflected in rainfall $\delta^{18}\text{O}$

1397 composition (Berkelhammer et al., 2012; Breitenbach et al., 2010). Rainfall $\delta^{18}\text{O}$ becomes
1398 progressively lighter during the ISM, but this effect is only partially driven by increasing
1399 precipitation intensity and the amount effect because the period of maximum precipitation
1400 (June-August) precedes maximum ^{18}O depletion (August-October) (Breitenbach et al., 2010)).
1401 Instead, the ^{18}O -depletion results predominantly from the moisture source shifting from a
1402 proximal location (the Bay of Bengal) in the early and late ISM to a more distal location (the
1403 open Indian Ocean) during the peak ISM (longer transport times resulting in more Rayleigh
1404 distillation). Rainfall and dripwater $\delta^{18}\text{O}$ at Mawmluh Cave are thus highly seasonal, but the
1405 relationship between temperature, rainfall amount, and rainfall $\delta^{18}\text{O}$ is not straightforward
1406 (Breitenbach et al., 2010; Breitenbach et al., 2015). Additional complexity arises from the
1407 filtering and buffering capacity of the karst aquifer through which rainwater percolates *en*
1408 *route* to a stalagmite. Although a clear seasonal dripwater $\delta^{18}\text{O}$ cycle exists, with its lowest
1409 value approximating ISM rainfall $\delta^{18}\text{O}$, its annual amplitude is compressed, reflecting buffering
1410 in the karst (Breitenbach et al., 2015). This further complicates the interpretation of $\delta^{18}\text{O}$
1411 records from these stalagmites, and information from independent proxies that are sensitive
1412 to processes dominating during the winter season is required to disentangle such processes.
1413 Combining summer-sensitive $\delta^{18}\text{O}$ with winter-sensitive Mg/Ca (reflecting PCP) permitted
1414 disentangling ISM strength and the degree of dry season dryness in a stalagmite from
1415 Mawmluh Cave (Myers et al., 2015; Ronay et al., 2019). Such a multi-proxy approach,
1416 supported by local monitoring and karst process modelling, allows robust interpretations of
1417 seasonal-scale climate from stalagmites, even when the proxy seasonality is driven by more
1418 complex processes than temperature or rainfall amount alone.

1419

1420 **7. Future directions and recommendations**

1421 In this review, we introduce and discuss several concepts that we hope will facilitate the
1422 development and interpretation of robust seasonal-resolution climate records
1423 from stalagmites, will improve the extraction and interpretation of seasonal information from
1424 stalagmites, and promote future discussion, including: **A)** that replication of records should
1425 not always be an expectation without *a priori* knowledge that the drip type and
1426 environmental conditions responsible for the deposition of the stalagmites are comparable
1427 (e.g., some stalagmites retain seasonal information, whereas others do not), **B)** that every
1428 stalagmite-based geochemical record is different and records a unique component of the
1429 environmental signal of varying complexity (i.e., each stalagmite retains an accurate history
1430 of its environment; the question is whether or not this history can be deconvolved), and **C)**
1431 that the application of at least one year's worth of hourly-resolved drip rate monitoring
1432 combined with a new drip classification scheme presented here may help identify stalagmites
1433 retaining a seasonal signal. Furthermore, we have **(D)** developed global seasonality maps of
1434 temperature (as was done previously by (James et al., 2015)), meteoric precipitation amount,
1435 and meteoric precipitation $\delta^{18}\text{O}$ ratios which allow the identification of regions sensitive to
1436 different types of seasonality recordable by stalagmites. The maps facilitate predicting what
1437 type of seasonality potentially affects modern stalagmite samples from that region. They also
1438 assist in palaeoclimate interpretations by identifying locations proximal to regions with
1439 pronounced seasonality, where past migration of key atmospheric circulation systems could
1440 have altered the geochemical record retained by a stalagmite. On a similar note, we **(E)**
1441 present a model that interprets annual- to centennial-scale stalagmite $\delta^{18}\text{O}$ records in terms
1442 of seasonal temperature and meteoric precipitation seasonality shifts. Although we stress

1443 that this model only highlights one possible interpretation (that the data were modulated
1444 primarily by regional long-term mean annual temperature variability combined with
1445 seasonality shifts in rainfall and temperature), often this interpretation is the most
1446 parsimonious. The modelling technique also helps identify time intervals when altered
1447 seasonality cannot account for the observed isotope shifts, suggesting that another variable
1448 needs consideration. We **(F)** discuss four major controls on the seasonality signal within
1449 stalagmites: i) Earth atmospheric, ii) Meteoric precipitation, iii) biological (e.g., soil processes),
1450 and iv) cave atmospheric, and **(G)** discuss a case study from India that serves as an example
1451 of a stalagmite whose seasonal signal is not derived from rainfall amount or regional
1452 temperature, but instead results from seasonal shifts in air mass trajectories (i.e., affected by
1453 seasonal shifts in Earth atmospheric processes).

1454 Stalagmites are remarkable archives of information regarding climate (on both seasonal and
1455 longer timescales), surface and cave environmental conditions, dry deposition, moisture
1456 source pathway, marine aerosols contributions, and hydrological routing. Replication of proxy
1457 records present strong support for palaeoclimatic [interpretations and](#)
1458 should remain a goal of any stalagmite science research programme, but unless the climate
1459 signal-to-noise ratio of a region is unusually high, replication is only possible when comparing
1460 stalagmites deposited under similar conditions. A thorough understanding of the
1461 environmental processes affecting both entire caves (e.g., ventilation) as well as individual
1462 stalagmites (e.g., drip rate) facilitates replication efforts. The geochemical record from even
1463 adjacent stalagmites will reflect numerous processes, some of which are common to the two
1464 samples but many which are not, and only through a thorough understanding of the processes
1465 affecting each sample are robust (and replicable) climate interpretations achievable.

1466 However, unless analytical issues exist, non-replication does not imply that one record is
1467 incorrect; rather it generally implies that the two records simply record different
1468 environmental parameters.

1469 Cave monitoring prior to the collection of a stalagmite will increase the likelihood of obtaining
1470 a record of the desired sensitivity to seasonal climate shifts, or other desired forcing. We
1471 recommend monitoring the drip feeding the stalagmite for at least one year using an
1472 automated drip logger and plotting the results in a diagram similar to Figure 3 to evaluate a
1473 stalagmite's likelihood of retaining hydrological seasonality. We recommend monitoring
1474 multiple sites within the cave and selecting the most appropriate stalagmite for collection
1475 based on the monitoring results. It is worth bearing in mind that unless the seasonality signal
1476 in a stalagmite is conveyed via seasonal cave ventilation, stalagmites fed by diffuse flow drips
1477 with long residence times may not retain seasonal information. Other drips that are
1478 seasonally either dry or undersaturated with respect to carbonate will lead to the
1479 occurrence of seasonal hiatuses in the stalagmites and signal loss for that particular
1480 season. Monitoring a stalagmite's drip rate and drip chemistry for as long as possible
1481 represents one of the simplest but most effective means of understanding the potential
1482 climate signal contained within a sample prior to collection. This also has implications for cave
1483 conservation and protection efforts, because clearly formulated research goals and drip
1484 monitoring prior to stalagmite sample collection can greatly reduce the number of samples
1485 removed from a cave for research purposes.

1486 If sample growth rate permits, we suggest that the extraction of the palaeoseasonality signal
1487 over millennial timescales is best achieved via micromilling, leaving no gap between
1488 adjacent samples, or LA-ICPMS. The major disadvantages of micromilling are that it is

1489 resource intensive and that many samples may not have growth rates high enough to permit
1490 the required [temporal](#) resolution. The major disadvantage of LA-ICPMS is that the trace
1491 element signature of a stalagmite is often dominated by site-specific factors such as
1492 temperature, sea spray, volcanic aerosols, fire, variable throughput of colloidal material, or
1493 rainfall, and consequently aligning the data with other records is sometimes complex.
1494 Micromilled carbonate powders that are divided into two or more aliquots that are
1495 subsequently analysed for stable isotope ratios, trace elements, and other geochemical
1496 proxies can provide very robust interpretations (e.g., Jamieson et al., 2016). This eliminates
1497 issues of cross-correlation and enables a powerful multiproxy approach, where each stable
1498 isotope ratio value is linked directly and unambiguously to numerous elemental
1499 concentration values. The technique can yield important information regarding
1500 palaeoseasonality but is considerably more resource intensive than running multiple LA-
1501 ICPMS tracks parallel to each other and the micromilled stable isotope track. An alternative is
1502 to produce a long decadal-scale isotope ratio traverse complemented by higher resolution
1503 transects or maps across key intervals of interest using LA-ICPMS, SIMS, synchrotron, or μ XRF
1504 to corroborate interpretations based on the longer transects. In the future, proxy mapping at
1505 micron-scale resolution using these techniques will help reduce uncertainties related to
1506 geometric ambiguities such as those associated with crystal boundaries and improve the
1507 robustness of interpretations.

1508

1509 **9. Conclusions**

1510 The reconstruction of palaeoseasonality using stalagmites is an exciting research direction
1511 that has yet to mature into its full potential. Numerous records of palaeoseasonality exist, but

1512 few direct reconstructions extend before the last two millennia. Ideally, future studies
1513 concluding that a decadal- to annual-scale isotope ratio record is affected by seasonality
1514 changes should support this by either using short windows of sub-annual data or by
1515 modelling.

1516 Any stalagmite-based climate proxy record is affected by inherent complexities in climate
1517 signal transfer to the stalagmite and by selective sampling of the stalagmite for analysis. A
1518 high-resolution (sub-annual to annual-scale) sampling strategy coupled with appropriate site
1519 monitoring maximises the likelihood of extracting a signal approximating the climate input
1520 signal. For long records annual- to decadal-scale resolution is ideal, and shorter records could
1521 benefit from an even higher resolution if resources permit. Large shifts in isotope ratios could
1522 reflect changes in seasonality, potentially associated with the migration of key atmospheric
1523 circulation systems over the cave site. New models incorporating seasonality can provide
1524 information regarding whether observed geochemical shifts are interpretable in terms of
1525 altered seasonality, and these represent an exciting and inexpensive new research tool. A
1526 seasonal-scale sampling strategy over short intervals of interest can verify these model
1527 interpretations, and LA-ICPMS or line-scan μ XRF represent potentially the most efficient
1528 methods to achieve this; other alternatives include monthly-scale micromilling, synchrotron
1529 analysis (SR- μ XRF), and SIMS.

1530 The robust interpretation of stalagmite geochemical records in terms of seasonality
1531 represents a key challenge for the next decade. Achieving this is complicated by multiple in-
1532 cave and exogenic environmental forcings with dynamic seasonality, including: rainfall,
1533 temperature, humidity, bioproductivity, cave air $p\text{CO}_2$, drip rate, source moisture region and
1534 $\delta^{18}\text{O}$, and moisture mass trajectory from the source region. Even apparently straightforward

1535 $\delta^{18}\text{O}$ records from regions with high signal-to-noise ratios typically interpretable as either
1536 varying total annual rainfall or summer rainfall may reflect another parameter instead
1537 (e.g., a change in moisture source or rainfall seasonality), as is the case with the Indian
1538 Summer Monsoon. Most records would benefit from a rigorous multi-proxy approach utilising
1539 not only multiple geochemical proxy datasets, but also site monitoring and new modelling
1540 approaches. Similarly, focussing research efforts at the same well-understood cave sites both
1541 maximises the quality of interpretations and contributes to the conservation of caves and
1542 stalagmite samples. The application of multiple stalagmites from the same site but with
1543 different drip rates and affected by different amounts of disequilibrium fractionation may
1544 provide the key to reconstructing formerly elusive climate variables, such as temperature.
1545 Instead of representing an irresolvable issue, we suggest that disequilibrium fractionation
1546 may present opportunities to quantify temperature, potentially even at seasonal resolutions.
1547 Similarly, multi-proxy data could yield seasonal information even in the absence of seasonal
1548 sampling resolution; if two or more independent proxies reflect different seasonal data,
1549 combining the proxies could yield palaeoseasonality.

1550 Over the past few decades stalagmites have provided some of the most iconic records in
1551 palaeoclimatology. In the future, stalagmites will continue to not only provide long records of
1552 exceptional quality, but they will also provide rare glimpses into palaeoseasonality at
1553 unprecedented temporal resolution. Recent microanalytical advances have facilitated the
1554 construction of exquisitely resolved stalagmite-based climate records; we are now at a stage
1555 where the interpretation of these records is catching up with their remarkable technical
1556 aspects. Extracting quantitative and accurate seasonal climate information from these

1557 geochemical records is a key challenge over the next decade, and, if this is achieved,
1558 stalagmites will truly be considered in a class of their own as climate archives.

1559

1560 **Acknowledgements**

1561 We thank SISAL and PAGES for access to the SISAL database v1b. Portions of this research
1562 were funded by European Research Council Grant #240167. Tim Horscroft is thanked for his
1563 support in facilitating the preparation of the manuscript. Ian Orland and
1564 [Jasper Wassenburg](#) are thanked for detailed constructive reviews that greatly
1565 improved the manuscript. Alex Iveson is thanked for useful comments regarding LA-ICPMS.

1566

1567 **References:**

- 1568 Allison, V.C., 1923. The growth of stalagmites and stalactites. *Journal of Geology* 31, 106-125.
- 1569 Allison, V.C., 1926. The antiquity of the deposit in Jacob's cavern. *American Museum of Natural*
1570 *History, Anthropological Papers* 19, 204-225.
- 1571 Anchukaitis, K.J., Wilson, R., Briffa, K.R., Buntgen, U., Cook, E.R., D'Arrigo, R., Davi, N., Esper, J.,
1572 Frank, D., Gunnarson, B.E., Hegerl, G., Helama, S., Klesse, S., Krusic, P.J., Linderholm, H.W., Myglan,
1573 V., Osborn, T.J., Zhang, P., Rydval, M., Schneider, L., Schurer, A., Wiles, G., Zorita, E., 2017. Last
1574 millennium Northern Hemisphere summer temperatures from tree rings: Part II, spatially resolved
1575 reconstructions. *Quaternary Sci. Rev.* 163, 1-22.

1576 Arbel, Y., Greenbaum, N., Lange, J., Inbar, M., 2010. Infiltration processes and flow rates in
1577 developed karst vadose zone using tracers in cave drips. *Earth Surface Processes and Landforms* 35,
1578 1682-1693.

1579 Arbel, Y., Greenbaum, N., Lange, J., Shtober-Zisu, N., Grodek, T., Wittenberg, L., Inbar, M., 2008.
1580 Hydrologic classification of cave drips in a Mediterranean climate, based on hydrograph separation
1581 and flow mechanisms. *Israel Journal of Earth Sciences* 57, 291-310.

1582 Asmerom, Y., Baldini, J.U.L., Pruger, K.M., Polyak, V.J., Ridley, H.E., Aquino, V.V., Baldini, L.M.,
1583 Breitenbach, S.F.M., Macpherson, C.G., Kennett, D.J., 2020. Intertropical convergence zone
1584 variability in the Neotropics during the Common Era. *Science Advances* 6, eaax3644.

1585 Atkinson, T.C., 1977. Diffuse flow and conduit flow in limestone terrain in the Mendip Hills, Somerset
1586 (Great Britain). *J Hydrol* 35, 93-110.

1587 Atkinson, T.C., Hess, J.W., Harmon, R.S., 1985. Stable isotope variations in recharge to a karstic
1588 aquifer, Yorkshire dales, England. *Annales de la Société Géologique de Belgique* 108, 225.

1589 Atsawawaranunt, K., Comas-Bru, L., Mozhdghi, S.A., Deininger, M., Harrison, S.P., Baker, A., Boyd,
1590 M., Kaushal, N., Ahmad, S.M., Brahim, Y.A., Arienzo, M., Bajo, P., Braun, K., Burstyn, Y., Chawchai, S.,
1591 Duan, W.H., Hatvani, I.G., Hu, J., Kern, Z., Labuhn, I., Lachniet, M., Lechleitner, F.A., Lorrey, A., Perez-
1592 Mejias, C., Pickering, R., Scroxton, N., Members, S.W.G., 2018. The SISAL database: a global resource
1593 to document oxygen and carbon isotope records from speleothems. *Earth System Science Data* 10,
1594 1687-1713.

1595 Ayalon, A., Bar-Matthews, M., Sass, E., 1998. Rainfall-recharge relationships within a karstic terrain
1596 in the Eastern Mediterranean semi-arid region, Israel: $\delta^{18}O$ and δD characteristics *Journal of*
1597 *Hydrology* 207, 18-31.

1598 Badertscher, S., Borsato, A., Frisia, S., Cheng, H., Edwards, R.L., Tuysuz, O., Fleitmann, D., 2014.
1599 Speleothems as sensitive recorders of volcanic eruptions - the Bronze Age Minoan eruption recorded
1600 in a stalagmite from Turkey. *Earth Planet. Sci. Lett.* 392, 58-66.

1601 Baker, A., Barnes, W.L., Smart, P.L., 1997. Variations in the discharge and organic matter content of
1602 stalagmite drip waters in Lower Cave, Bristol. *Hydrological Processes* 11, 1541-1555.

1603 Baker, A., Bradley, C., 2010. Modern stalagmite $\delta^{18}O$: Instrumental calibration and forward
1604 modelling. *Global and Planetary Change* 71, 201-206.

1605 Baker, A., Brunson, C., 2003. Non-linearities in drip water hydrology: an example from Stump Cross
1606 Caverns, Yorkshire. *Journal of Hydrology* 277, 151-163.

1607 Baker, A., Hartmann, A., Duan, W., Hankin, S., Comas-Bru, L., Cuthbert, M.O., Treble, P.C., Banner, J.,
1608 Genty, D., Baldini, L.M., Bartolomé, M., Moreno, A., Pérez-Mejías, C., Werner, M., 2019. Global
1609 analysis reveals climatic controls on the oxygen isotope composition of cave drip water. *Nature*
1610 *Communications* 10, 2984.

1611 Baker, A., Smart, P.L., Edwards, R.L., Richards, D.A., 1993. Annual growth banding in a cave
1612 stalagmite. *Nature* 364, 518-520.

1613 Baker, A.J., Matthey, D.P., Baldini, J.U.L., 2014. Reconstructing modern stalagmite growth from cave
1614 monitoring, local meteorology, and experimental measurements of dripwater films. *Earth Planet.*
1615 *Sci. Lett.* 392, 239-249.

1616 Baldini, J.U.L., Bertram, R.A., Ridley, H.E., 2018. Ground air: A first approximation of the Earth's
1617 second largest reservoir of carbon dioxide gas. *Sci. Total Environ.* 616-617, 1007-1013.

1618 Baldini, J.U.L., McDermott, F., Baker, A., Baldini, L.M., Matthey, D.P., Railsback, L.B., 2005. Biomass
1619 effects on stalagmite growth and isotope ratios: A 20th century analogue from Wiltshire, England.
1620 Earth Planet. Sci. Lett. 240, 486-494.

1621 Baldini, J.U.L., McDermott, F., Baldini, L.M., Ottley, C.J., Linge, K.L., Clipson, N., Jarvis, K.E., 2012.
1622 Identifying short-term and seasonal trends in cave drip water trace element concentrations based on
1623 a daily-scale automatically collected drip water dataset. Chem. Geol. 330, 1-16.

1624 Baldini, J.U.L., McDermott, F., Fairchild, I.J., 2002. Structure of the 8200-year cold event revealed by
1625 a speleothem trace element record. Science 296, 2203-2206.

1626 Baldini, J.U.L., McDermott, F., Fairchild, I.J., 2006. Spatial variability in cave drip water
1627 hydrochemistry: Implications for stalagmite paleoclimate records. Chem. Geol. 235, 390-404.

1628 Baldini, J.U.L., McDermott, F., Hoffmann, D.L., Richards, D.A., Clipson, N., 2008. Very high-frequency
1629 and seasonal cave atmosphere P_{CO_2} variability: Implications for stalagmite growth and oxygen
1630 isotope-based paleoclimate records. Earth Planet. Sci. Lett. 272, 118-129.

1631 Baldini, L.M., Baldini, J.U.L., McDermott, F., Arias, P., Cueto, M., Fairchild, I.J., Hoffmann, D.L.,
1632 Matthey, D.P., Müller, W., Nita, D.C., Ontañón, R., Garcíá-Moncó, C., Richards, D.A., 2019. North
1633 Iberian temperature and rainfall seasonality over the Younger Dryas and Holocene. Quaternary Sci.
1634 Rev. 226, 105998.

1635 Baldini, L.M., McDermott, F., Baldini, J.U.L., Arias, P., Cueto, M., Fairchild, I.J., Hoffmann, D.L.,
1636 Matthey, D.P., Müller, W., Nita, D.C., Ontañón, R., Garcíá-Moncó, C., Richards, D.A., 2015. Regional
1637 temperature, atmospheric circulation, and sea-ice variability within the Younger Dryas Event
1638 constrained using a speleothem from northern Iberia. Earth Planet. Sci. Lett. 419, 101-110.

1639 Ban, F.M., Baker, A., Marjo, C.E., Duan, W.H., Li, X.L., Han, J.X., Coleborn, K., Akter, R., Tan, M.,
1640 Nagra, G., 2018. An optimized chronology for a stalagmite using seasonal trace element cycles from
1641 Shihua Cave, Beijing, North China. *Scientific Reports* 8, 4551.

1642 Banner, J.L., Guilfoyle, A., James, E.W., Stern, L.A., Musgrove, M., 2007. Seasonal variations in
1643 modern speleothem calcite growth in Central Texas, USA. *J Sediment Res* 77, 615-622.

1644 Bar-Matthews, M., Ayalon, A., Matthews, A., Sass, E., Halicz, L., 1996. Carbon and oxygen isotope
1645 study of the active water-carbonate system in a karstic Mediterranean cave: Implications for
1646 paleoclimate research in semiarid regions. *Geochim. Cosmochim. Acta* 60, 337-347.

1647 Bergel, S.J., Carlson, P.E., Larson, T.E., Wood, C.T., Johnson, K.R., Banner, J., Breecker, D.O., 2017.
1648 Constraining the subsoil carbon source to cave-air CO₂ and speleothem calcite in central Texas. 217,
1649 112-127.

1650 Berkelhammer, M., Sinha, A., Stott, L., Cheng, H., Pausata, F.S.R., Yoshimura, K., 2012. An abrupt
1651 shift in the Indian Monsoon 4000 years ago. *Geophysical Monograph Series* 198, 75-87.

1652 Blyth, A.J., Baker, A., Thomas, L.E., Van Calsteren, P., 2011. A 2000-year lipid biomarker record
1653 preserved in a stalagmite from north-west Scotland. *J. of Quaternary Sci.* 26, 326-334.

1654 Borsato, A., Frisia, S., Fairchild, I.J., Somogyi, A., Susini, J., 2007. Trace element distribution in annual
1655 stalagmite laminae mapped by micrometer-resolution X-ray fluorescence: Implications for
1656 incorporation of environmentally significant species. *Geochim. Cosmochim. Acta* 71, 1494-1512.

1657 Borsato, A., Frisia, S., Hellstrom, J., Treble, P., Johnson, K., Howard, D., Greig, A., 2019. Fast high-
1658 resolution synchrotron micro-XRF mapping of annually laminated stalagmites, European Geoscience
1659 Union General Assembly. EGU, Vienna.

1660 Borsato, A., Frisia, S., Wynn, P.M., Fairchild, I.J., Miorandi, R., 2015. Sulphate concentration in cave
1661 dripwater and speleothems: long-term trends and overview of its significance as proxy for
1662 environmental processes and climate changes. *Quaternary Sci. Rev.* 127, 48-60.

1663 Breecker, D.O., Payne, A.E., Quade, J., Banner, J.L., Ball, C.E., Meyer, K.W., Cowan, B.D., 2012. The
1664 sources and sinks of CO₂ in caves under mixed woodland and grassland vegetation. *Geochim.*
1665 *Cosmochim. Acta* 96, 230-246.

1666 Breitenbach, S.F.M., Adkins, J.F., Meyer, H., Marwan, N., Kumar, K.K., Haug, G.H., 2010. Strong
1667 influence of water vapor source dynamics on stable isotopes in precipitation observed in Southern
1668 Meghalaya, NE India. *Earth and Planetary Science Letters* 292, 212-220.

1669 Breitenbach, S.F.M., Bernasconi, S.M., 2011. Carbon and oxygen isotope analysis of small carbonate
1670 samples (20 to 100 μ g) with a GasBench II preparation device. *Rapid Commun. Mass Spectrom.*
1671 25, 1910-1914.

1672 Breitenbach, S.F.M., Lechleitner, F.A., Meyer, H., Diengdoh, G., Matthey, D., Marwan, N., 2015. Cave
1673 ventilation and rainfall signals in dripwater in a monsoonal setting – a monitoring study from NE
1674 India. *Chemical Geology* 402, 111-124.

1675 Breitenbach, S.F.M., Plessen, B., Waltgenbach, S., Tjallingii, R., Leonhardt, J., Jochum, K.P., Meyer, H.,
1676 Goswami, B., Marwan, N., Scholz, D., 2019. Holocene interaction of maritime and continental climate
1677 in Central Europe: New speleothem evidence from Central Germany. *Global and Planet. Change* 176,
1678 144-161.

1679 Broecker, W.S., 1960. Radiocarbon measurements and annual rings in cave formations. *Nature* 185,
1680 93-94.

1681 Broughton, P.L., 1983. Environmental Implications of competitive growth fabrics in stalactitic
1682 carbonate. *International Journal of Speleology*. 13, 31-41.

1683 Buhmann, D., Dreybrodt, W., 1985. The kinetics of calcite dissolution and precipitation in
1684 geologically relevant situations of karst areas. 2. closed system. *Chem. Geol.* 53, 109-124.

1685 Cabellero, E., Jimenez de Cisneros, C., Reyes, E., 1996. A stable isotope study of cave seepage waters.
1686 *Applied Geochemistry* 11, 583-587.

1687 Carlson, P.E., Miller, N.R., Banner, J.L., Breecker, D.O., Casteel, R.C., 2018. The potential of near-
1688 entrance stalagmites as high-resolution terrestrial paleoclimate proxies: Application of isotope and
1689 trace-element geochemistry to seasonally-resolved chronology. *Geochimica et Cosmochimica Acta*
1690 235, 55-75.

1691 Chapman, J.B., Ingraham, N.L., Hess, J.W., 1992. Isotopic investigation of infiltration and unsaturated
1692 zone flow processes at Carlsbad Caverns. *Journal of Hydrology* 133, 343-363.

1693 Chen, C.-J., Li, T.-Y., 2018. Geochemical characteristics of cave drip water respond to ENSO based on
1694 a 6-year monitoring work in Yangkou Cave, Southwest China. *Journal of Hydrology* 561, 896-907.

1695 Cheng, H., Lawrence Edwards, R., Shen, C.-C., Polyak, V.J., Asmerom, Y., Woodhead, J., Hellstrom, J.,
1696 Wang, Y., Kong, X., Spötl, C., Wang, X., Calvin Alexander, E., 2013. Improvements in ²³⁰Th dating,
1697 ²³⁰Th and ²³⁴U half-life values, and U–Th isotopic measurements by multi-collector inductively
1698 coupled plasma mass spectrometry. *Earth and Planetary Science Letters* 371-372, 82-91.

1699 Cole, J.M., Nienstedt, J., Spataro, G., Rasbury, E.T., Lanzirotti, A., Celestian, A.J., Nilsson, M., Hanson,
1700 G.N., 2003. Phosphor imaging as a tool for in situ mapping of ppm levels of uranium and thorium in
1701 rocks and minerals. *Chem. Geol.* 193, 127-136.

1702 Comas-Bru, L., Harrison, S.P., 2019. SISAL: Bringing Added Value to Speleothem Research.
1703 *Quaternary* 2, 7.

1704 Comas-Bru, L., Harrison, S.P., Werner, M., Rehfeld, K., Scroxton, N., Veiga-Pires, C., Ahmad, S.M.,
1705 Brahim, Y.A., Mozdhehi, S.A., Arienzo, M., Atsawawaranunt, K., Baker, A., Braun, K., Breitenbach, S.,
1706 Burstyn, Y., Chawchai, S., Columbu, A., Deininger, M., Demeny, A., Dixon, B., Hatvani, I.G., Hu, J.,
1707 Kaushal, N., Kern, Z., Labuhn, I., Lachniet, M.S., Lechleitner, F.A., Lorrey, A., Markowska, M., Nehme,
1708 C., Novello, V.F., Oster, J., Perez-Mejias, C., Pickering, R., Sekhon, N., Wang, X.F., Warken, S.,
1709 Atkinson, T., Ayalon, A., Baldini, J., Bar-Matthews, M., Bernal, J.P., Boch, R., Borsato, A., Boyd, M.,
1710 Brierley, C., Cai, Y.J., Carolin, S., Cheng, H., Constantin, S., Couchoud, I., Cruz, F., Denniston, R.,
1711 Dragusin, V., Duan, W.H., Ersek, V., Finne, M., Fleitmann, D., Fohlmeister, J., Frappier, A., Genty, D.,
1712 Holzkamper, S., Hopley, P., Johnston, V., Kathayat, G., Keenan-Jones, D., Koltai, G., Li, T.Y., Lone,
1713 M.A., Luetscher, M., Matthey, D., Moreno, A., Moseley, G., Psomiadis, D., Ruan, J.Y., Scholz, D., Sha,
1714 L.J., Smith, A.C., Strikis, N., Treble, P., Unal-Imer, E., Vaks, A., Vansteenberge, S., Voarintsoa, N.R.G.,
1715 Wong, C., Wortham, B., Wurtzel, J., Zhang, H., Grp, S.W., 2019. Evaluating model outputs using
1716 integrated global speleothem records of climate change since the last glacial. *Clim Past* 15, 1557-
1717 1579.

1718 Cook, E.R., Krusic, P.J., Anchukaitis, K.J., Buckley, B.M., Nakatsuka, T., Sano, M., Asia2K, P., 2013.
1719 Tree-ring reconstructed summer temperature anomalies for temperate East Asia since 800 CE. *Clim.*
1720 *Dynam.* 41, 2957-2972.

1721 Cowan, B.D., Osborne, M.C., Banner, J.L., 2013. Temporal variability of cave air PCO₂ in Central
1722 Texas. *J Cave Karst Stud* 75, 38-50.

1723 Cruz Jr., F.W., Karmann, I., Vianna, J., O., Burns, S.J., Ferrari, J.A., Vuille, M., Sial, A.N., Moreira, M.Z.,
1724 2005. Stable isotope study of cave percolation waters in subtropical Brazil: Implications for
1725 paleoclimate inferences from speleothems. *Chemical Geology* 220, 245-262.

1726 Czuppon, G., Demény, A., Leél-Össy, S., Óvari, M., Stieber, J., Kiss, K., Kármán, K., Surányi, G.,
1727 Haszpra, L., 2018. Cave monitoring in the Béke and Baradla caves (Northeastern Hungary):

1728 implications for the conditions for the formation cave carbonates. International Journal of
1729 Speleology, 13-28.

1730 Daëron, M., Drysdale, R.N., Peral, M., Huyghe, D., Blamart, D., Coplen, T.B., Lartaud, F., Zanchetta,
1731 G., 2019. Most Earth-surface calcites precipitate out of isotopic equilibrium. Nat Commun 10.

1732 Deininger, M., McDermott, F., Mudelsee, M., Werner, M., Frank, N., Mangini, A., 2017. Coherency of
1733 late Holocene European speleothem delta O-18 records linked to North Atlantic Ocean circulation.
1734 Clim. Dynam. 49, 595-618.

1735 Deininger, M., Scholz, D., 2019. ISOLUTION 1.0: an ISOTOpe evoLUTION model describing the stable
1736 oxygen (delta O-18) and carbon (delta C-13) isotope values of speleothems. Int J Speleol 48, 21-32.

1737 Deininger, M., Werner, M., McDermott, F., 2016. North Atlantic Oscillation controls on oxygen and
1738 hydrogen isotope gradients in winter precipitation across Europe; implications for palaeoclimate
1739 studies. Clim Past 12, 2127-2143.

1740 Dredge, J., Fairchild, I.J., Harrison, R.M., Fernandez-Cortes, A., Sanchez-Moral, S., Jurado, V., Gunn, J.,
1741 Smith, A., Spotl, C., Matthey, D., Wynn, P.M., Grassineau, N., 2013. Cave aerosols: distribution and
1742 contribution to speleothem geochemistry. Quaternary Sci. Rev. 63, 23-41.

1743 Dreybrodt, W., 1980. Deposition of calcite from thin films of natural calcareous solutions and the
1744 growth of speleothems. Chem. Geol. 29, 89-105.

1745 Dreybrodt, W., 1988. Processes in karst systems - physics, chemistry and geology. Springer, Berlin,
1746 New York.

1747 Dreybrodt, W., 1999. Chemical kinetics, speleothem growth and climate. Boreas 28, 347-356.

1748 Dreybrodt, W., Deininger, M., 2014. The impact of evaporation to the isotope composition of DIC in
1749 calcite precipitating water films in equilibrium and kinetic fractionation models. *Geochim.*
1750 *Cosmochim. Acta* 125, 433-439.

1751 Duan, F.C., Wu, J.Y., Wang, Y.J., Edwards, R.L., Cheng, H., Kong, X.G., Zhang, W.H., 2015. A 3000-yr
1752 annually laminated stalagmite record of the Last Glacial Maximum from Hulu Cave, China.
1753 *Quaternary Res.* 83, 360-369.

1754 Duan, W., Ruan, J., Luo, W., Li, T., Tian, L., Zeng, G., Zhang, D., Bai, Y., Li, J., Tao, T., Zhang, P., Baker,
1755 A., Tan, M., 2016. The transfer of seasonal isotopic variability between precipitation and drip water
1756 at eight caves in the monsoon regions of China. *Geochim. Cosmochim. Acta* 183, 250-266.

1757 Edwards, L.R., Chen, J.H., Wasserburg, G.J., 1987. ^{238}U - ^{234}U - ^{230}Th - ^{232}Th systematics and the
1758 precise measurement of time over the past 500,000 years. *Earth Planet. Sci. Lett.* 81, 175-192.

1759 Edwards, R.L., Gallup, C.D., 1993. Dating of the Devils Hole Calcite Vein. *Science* 259, 1626-1627.

1760 Emiliani, C., 1955. Pleistocene temperatures. *Journal of Geology* 63, 538-578.

1761 Epstein, S., Buchsbaum, R., Lowenstam, H.A., Urey, H.C., 1951. Carbonate-water isotopic
1762 temperature scale. *Bulletin of the Geological Society of America* 62, 417-427.

1763 Evans, D., Müller, W., 2013. LA-ICPMS elemental imaging of complex discontinuous carbonates: An
1764 example using large benthic foraminifera. *J. Anal. At. Spectrom.* 28, 1039-1044.

1765 Evans, M.N., Tolwinski-Ward, S.E., Thompson, D.M., Achukaitis, K.J., 2013. Applications of proxy
1766 system modeling in high resolution paleoclimatology. *Quaternary Science Reviews* 76, 16-28.

1767 Faimon, J., Lang, M., 2013. Variances in airflows during different ventilation modes in a dynamic U-
1768 shaped cave. *Int J Speleol* 42, 115-122.

1769 Fairchild, I.J., Baker, A., 2012. *Speleothem Science: From Processes to Past Environments*. Wiley-
1770 Blackwell, Chichester, UK.

1771 Fairchild, I.J., Baker, A., Borsato, A., Frisia, S., Hinton, R.W., McDermott, F., Tooth, A.F., 2001. Annual
1772 to sub-annual resolution of multiple trace-element trends in speleothems. *Journal of the Geological*
1773 *Society of London* 158, 831-841.

1774 Fairchild, I.J., Borsato, A., Tooth, A.F., Frisia, S., Hawkesworth, C.J., Huang, Y., McDermott, F., Spiro,
1775 B., 2000. Controls on trace element (Sr-Mg) compositions of carbonate cave waters: implications for
1776 speleothem climatic records. *Chem. Geol.* 166, 255-269.

1777 Fairchild, I.J., Hartland, A., 2010. Trace element variations in stalagmites: controls by climate and by
1778 karst system processes. *EMU Notes in Mineralogy* 10, 259-287.

1779 Fairchild, I.J., Smith, C.L., Baker, A., Fuller, L., Spotl, C., Matthey, D., McDermott, F., Eimp, 2006.
1780 Modification and preservation of environmental signals in speleothems. *Earth Sci. Rev.* 75, 105-153.

1781 Fairchild, I.J., Treble, P.C., 2009. Trace elements in speleothems as recorders of environmental
1782 change. *Quaternary Science Reviews* 28, 449-468.

1783 Feng, W., Casteel, R.C., Banner, J.L., Heinze-Fry, A., 2014. Oxygen isotope variations in rainfall, drip-
1784 water and speleothem calcite from a well-ventilated cave in Texas, USA: Assessing a new
1785 speleothem temperature proxy. *Geochim. Cosmochim. Acta* 127, 233-250.

1786 Feng, X., Porporato, A., Rodriguez-Iturbe, I., 2013. Changes in rainfall seasonality in the tropics.
1787 *Nature Climate Change* 3, 811-815.

1788 Fick, S.E., Hijmans, R.J., 2017. WorldClim 2: new 1-km spatial resolution climate surfaces for global
1789 land areas. *Int J Climatol* 37, 4302-4315.

1790 Finch, A.A., Shaw, P.A., Weedon, G.P., Holmgren, K., 2001. Trace element variation in speleothem
1791 aragonite: potential for palaeoenvironmental reconstruction. *Earth Planet. Sci. Lett.* 186, 255-267.

1792 Fohlmeister, J., Lechleitner, F.A., 2019. STAlagmite dating by radiocarbon (star): A software tool for
1793 reliable and fast age depth modelling. *Quat Geochronol* 51, 120-129.

1794 Fohlmeister, J., Plessen, B., Dudashvili, A.S., Tjallingii, R., Wolff, C., Gafurov, A., Cheng, H., 2017.
1795 Winter precipitation changes during the Medieval Climate Anomaly and the Little Ice Age in arid
1796 Central Asia. *Quaternary Science Reviews* 178, 24-36.

1797 Frappier, A., Sahagian, D., González, L.A., Carpenter, S.J., 2002. El Niño Events Recorded by
1798 Stalagmite Carbon Isotopes. *Science* 298, 565-565.

1799 Frappier, A.B., Sahagian, D., Carpenter, S.J., González, L.A., Frappier, B.R., 2007. Stalagmite stable
1800 isotope record of recent tropical cyclone events. *Geology* 35.

1801 Frick, D.A., Schuessler, J.A., von Blanckenburg, F., 2016. Development of routines for simultaneous in
1802 situ chemical composition and stable Si isotope ratio analysis by femtosecond laser ablation
1803 inductively coupled plasma mass spectrometry. *Analytica Chimica Acta* 938, 33-43.

1804 Frisia, S., 2015. Microstratigraphic logging of calcite fabrics in speleothems as tool for palaeoclimate
1805 studies. *Int J Speleol* 44, 1-16.

1806 Frisia, S., Borsato, A., Fairchild, I.J., McDermott, F., 2000. Calcite fabrics, growth mechanisms, and
1807 environments of formation in speleothems from the Italian Alps and southwestern Ireland. *J*
1808 *Sediment Res* 70, 1183-1196.

1809 Frisia, S., Borsato, A., Fairchild, I.J., Susini, J., 2005. Variations in atmospheric sulphate recorded in
1810 stalagmites by synchrotron micro-XU and XANES analyses. *Earth Planet. Sci. Lett.* 235, 729-740.

1811 Frisia, S., Borsato, A., Hellstrom, J., 2018. High spatial resolution investigation of nucleation, growth
1812 and early diagenesis in speleothems as exemplar for sedimentary carbonates. *Earth Sci. Rev.* 178, 68-
1813 91.

1814 Frisia, S., Borsato, A., Susini, J., 2008. Synchrotron radiation applications to past volcanism archived
1815 in speleothems: An overview. *J. Volcanol. Geotherm. Res.* 177, 96-100.

1816 Gascoyne, M., Schwarcz, H.P., Ford, D.C., 1980. A palaeotemperature record for the mid-Wisconsin
1817 in Vancouver Island. *Nature* 285, 474-476.

1818 Gazis, C., Feng, X.H., 2004. A stable isotope study of soil water: evidence for mixing and preferential
1819 flow paths. *Geoderma* 119, 97-111.

1820 Genty, D., 2008. Palaeoclimate research in Villars Cave (Dordogne, SW France). *Int J Speleol* 37, 173-
1821 191.

1822 Genty, D., Baker, A., Vokal, B., 2001. Intra- and inter-annual growth rate of modern stalagmites.
1823 *Chemical Geology* 176, 191-212.

1824 Genty, D., Deflandre, G., 1998. Drip flow variations under a stalactite of the Père Noël cave
1825 (Belgium). Evidence of seasonal variations and air pressure constraints. *J Hydrol* 211, 208-232.

1826 Guo, W., Zhou, C., 2019. Patterns and controls of disequilibrium isotope effects in speleothems:
1827 Insights from an isotope-enabled diffusion-reaction model and implications for quantitative
1828 thermometry. *Geochimica et Cosmochimica Acta* 267, 196-226.

1829 Harmon, R.S., 1979. An isotopic study of groundwater seepage in the Central Kentucky karst. *Water*
1830 *Resources Research* 15, 476.

1831 Hartland, A., Fairchild, I.J., Lead, J.R., 2009. Colloids in karstic percolation waters: Implications for the
1832 interpretation of trace element variations in speleothems. *Geochim. Cosmochim. Acta* 73, A498-
1833 A498.

1834 Hartland, A., Fairchild, I.J., Lead, J.R., Baker, A., 2010. Fluorescent properties of organic carbon in
1835 cave dripwaters: Effects of filtration, temperature and pH. *Sci. Total Environ.* 408, 5940-5950.

1836 Hartland, A., Fairchild, I.J., Lead, J.R., Borsato, A., Baker, A., Frisia, S., Baalousha, M., 2012. From soil
1837 to cave: Transport of trace metals by natural organic matter in karst dripwaters. *Chem. Geol.* 304,
1838 68-82.

1839 Hartland, A., Fairchild, I.J., Lead, J.R., Zhang, H., Baalousha, M., 2011. Size, speciation and lability of
1840 NOM-metal complexes in hyperalkaline cave dripwater. *Geochim. Cosmochim. Acta* 75, 7533-7551.

1841 Hellstrom, J., 2003. Rapid and accurate U/Th dating using parallel ion-counting multi-collector ICP-
1842 MS. *J. Anal. At. Spectrom.* 18, 1346-1351.

1843 Helser, T.E., Kestelle, C.R., McKay, J.L., Orland, I.J., Kodzon, R., Valley, J.W., 2018. Evaluation of
1844 micromilling/conventional isotope ratio mass spectrometry and secondary ion mass spectrometry of
1845 $\delta^{18}\text{O}$ values in fish otoliths for sclerochronology. *Rapid Commun Mass Spectrom* 32, 1781-1790.

1846 Hendy, C.H., Wilson, A.T., 1968. Paleoclimatic data from speleothems. *Nature* 216, 48-51.

1847 Hess, J.W., White, W.B., 1989. Water Budget and Physical Hydrology, in: B., W.W., White, E.L. (Eds.),
1848 *Karst Hydrology: Concepts from the Mammoth Cave Area*. Springer-Verlag, Boston, pp. 105-126.

1849 Hoffmann, D.L., Prytulak, J., Richards, D.A., Elliott, T.R., Coath, C.D., Smart, P.L., Scholz, D., 2007.
1850 Procedures for accurate U and Th isotope measurements by high precision MC-ICPMS. *Int. J. Mass*
1851 *Spectrom. Ion Processes* 264, 97-109.

1852 Hsiang, S.M., Burke, M., Miguel, E., 2013. Quantifying the Influence of Climate on Human Conflict.
1853 Science 341, 1235367.

1854 Hu, C., Henderson, G.M., Huang, J., Xie, S., Sun, Y., Johnson, K.R., 2008. Quantification of Holocene
1855 Asian monsoon rainfall from spatially separated cave records. Earth Planet. Sci. Lett. 266, 221-232.

1856 Huang, S.P., Pollack, H.N., Shen, P.Y., 2000. Temperature trends over the past five centuries
1857 reconstructed from borehole temperatures. Nature 403, 756-758.

1858 Huang, Y., Fairchild, I.J., 2001. Partitioning of Sr²⁺ and Mg²⁺ into calcite under karst-analogue
1859 experimental conditions. Geochim. Cosmochim. Acta 65, 47-62.

1860 Huang, Y., Fairchild, I.J., Borsato, A., Frisia, S., Cassidy, N.J., McDermott, F., Hawkesworth, C.J., 2001.
1861 Seasonal variations in Sr, Mg and P in modern speleothems (Grotta di Ernesto, Italy). Chem. Geol.
1862 175, 429-448.

1863 IAEA, 2001. GNIP Maps and Animations. , Vienna.

1864 IAEA/WMO, 2001. Global Network of Isotopes in Precipitation. The GNIP Database.

1865 James, E., Banner, J., Hardt, B., 2015. A global model for cave ventilation and seasonal bias in
1866 speleothem paleoclimate records.

1867 Jamieson, R.A., Baldini, J.U.L., Brett, M.J., Taylor, J., Ridley, H.E., Ottley, C.J., Prufer, K.M.,
1868 Wassenburg, J.A., Scholz, D., Breitenbach, S.F.M., 2016. Intra- and inter-annual uranium
1869 concentration variability in a Belizean stalagmite controlled by prior aragonite precipitation: A new
1870 tool for reconstructing hydro-climate using aragonitic speleothems. Geochim. Cosmochim. Acta 190,
1871 332-346.

1872 Jamieson, R.A., Baldini, J.U.L., Frappier, A.B., Muller, W., 2015. Volcanic ash fall events identified
1873 using principle component analysis of a high-resolution speleothem trace element dataset. *Earth*
1874 *Planet. Sci. Lett.* 426, 36-45.

1875 Johnson, K.R., Hu, C., Belshaw, N.S., Henderson, G.M., 2006. Seasonal trace-element and stable-
1876 isotope variations in a Chinese speleothem: The potential for high-resolution paleomonsoon
1877 reconstruction. *Earth Planet. Sci. Lett.* 244, 394-407.

1878 Kaufman, A., Bar-Matthews, M., Ayalon, A., Carmi, I., 2003. The vadose flow above Soreq Cave,
1879 Israel: a tritium study of the cave waters. *Journal of Hydrology* 273, 155-163.

1880 Kennett, D.J., Breitenbach, S.F.M., Aquino, V.V., Asmerom, Y., Awe, J., Baldini, J.U.L., Bartlein, P.,
1881 Culleton, B.J., Ebert, C., Jazwa, C., Macri, M.J., Marwan, N., Polyak, V., Pruffer, K.M., Ridley, H.E.,
1882 Sodemann, H., Winterhalder, B., Haug, G.H., 2012. Development and Disintegration of Maya Political
1883 Systems in Response to Climate Change. *Science* 338, 788-791.

1884 Khiewtam, R.S., Ramakrishnan, P.S., 1993. Litter and fine root dynamics of a relict sacred grove
1885 forest at Cherrapunji in north-eastern India. *Forest Ecology and Management* 60, 327-344.

1886 Kita, N.T., Huberty, J.M., Kozdon, R., Beard, B.L., Valley, J.W., 2011. High-precision SIMS oxygen,
1887 sulfur and iron stable isotope analyses of geological materials: accuracy, surface topography and
1888 crystal orientation. *Surf. Interface Anal.* 43, 427-431.

1889 Kolodny, Y., Bar-Matthews, M., Ayalon, A., McKeegan, K.D., 2003. A high spatial resolution $\delta^{18}\text{O}$
1890 profile of a speleothem using an ion-microprobe. *Chemical Geology* 197, 21-28.

1891 Köppen, W., 1918. Classification of climates according to temperature, precipitation and course of
1892 the year. *Petermanns Mitt* 64, 193-203.

1893 Kuczumow, A., Genty, D., Chevallier, P., Nowak, J., Ro, C.U., 2003. Annual resolution analysis of a
1894 SW-France stalagmite by X-ray synchrotron microprobe analysis. *Spectrochim Acta B* 58, 851-865.

1895 Kuczumow, A., Vekemans, B., Schalm, O., Gysels, K., Ro, C.U., Van Grieken, R., 2001. Analysis of
1896 speleothems by electron and X-ray microprobes. *J. Anal. At. Spectrom.* 16, 90-95.

1897 Kylander-Clark, A.R.C., Hacker, B.R., Cottle, J.M., 2013. Laser-ablation split-stream ICP
1898 petrochronology. *Chemical Geology* 345, 99-112.

1899 Lachniet, M.S., 2009. Climatic and environmental controls on speleothem oxygen-isotope values.
1900 *Quaternary Science Reviews* 28, 412-432.

1901 Lauritzen, S., 1995. High Resolution Paleotemperature Proxy Record for the Last Interglaciation
1902 Based on Norwegian Speleothems. *Quaternary Res.* 43, 133-146.

1903 Lauritzen, S., Lundberg, J., 1999. Calibration of the speleothem delta function: an absolute
1904 temperature record for the Holocene in northern Norway. *Holocene* 9, 659-669.

1905 Lechleitner, F.A., Baldini, J.U.L., Breitenbach, S.F.M., Fohlmeister, J., McIntyre, C., Goswami, B.,
1906 Jamieson, R.A., van der Voort, T.S., Prufer, K., Marwan, N., Culleton, B.J., Kennett, D.J., Asmerom, Y.,
1907 Polyak, V., Eglinton, T.I., 2016a. Hydrological and climatological controls on radiocarbon
1908 concentrations in a tropical stalagmite. *Geochim. Cosmochim. Acta* 194, 233-252.

1909 Lechleitner, F.A., Fohlmeister, J., McIntyre, C., Baldini, L.M., Jamieson, R.A., Hercman, H.,
1910 Gąsiorowski, M., Pawlak, J., Stefaniak, K., Socha, P., Eglinton, T.I., Baldini, J.U.L., 2016b. A novel
1911 approach for construction of radiocarbon-based chronologies for speleothems. *Quaternary*
1912 *Geochronology* 35, 54-66.

1913 Li, F., Vanwezer, N., Boivin, N., Gao, X., Ott, F., Petraglia, M., Roberts, P., 2019. Heading north: Late
1914 Pleistocene environments and human dispersals in central and eastern Asia. *Plos One* 14, e0216433.

1915 Linzmeier, B.J., Kitajima, K., Denny, A.C., Cammack, J.N., 2018. Making maps on a micrometer scale.
1916 Eos 99.

1917 Liu, Y., Tang, G., Ling, X., Hu, C., Li, X., 2015. Speleothem annual layers revealed by seasonal SIMS
1918 $\delta^{18}O$ measurements. Science China Earth Sciences 58, 1741-1747.

1919 Liu, Y.H., Henderson, G.M., Hu, C.Y., Mason, A.J., Charnley, N., Johnson, K.R., Xie, S.C., 2013. Links
1920 between the East Asian monsoon and North Atlantic climate during the 8,200 year event. Nat.
1921 Geosci. 6, 117-120.

1922 Luetscher, M., Boch, R., Sodemann, H., Spotl, C., Cheng, H., Edwards, R.L., Frisia, S., Hof, F., Müller,
1923 W., 2015. North Atlantic storm track changes during the Last Glacial Maximum recorded by Alpine
1924 speleothems. Nat Commun 6, 6344.

1925 Luo, T., Hu, Z., Zhang, W., Günther, D., Liu, Y., Zong, K., Hu, S., 2018. Reassessment of the influence
1926 of carrier gases He and Ar on signal intensities in 193 nm excimer LA-ICP-MS analysis. Journal of
1927 Analytical Atomic Spectrometry 33, 1655-1663.

1928 Luo, W., Wang, S., Zeng, G., Zhu, X., Liu, W., 2014. Daily response of drip water isotopes to
1929 precipitation in Liangfeng Cave, Guizhou Province, SW China. Quaternary International 349, 153-158.

1930 Markowska, M., Baker, A., Andersen, M.S., Jex, C.N., Cuthbert, M.O., Rau, G.C., Graham, P.W.,
1931 Rutledge, H., Mariethoz, G., Marjo, C.E., Treble, P.C., Edwards, N., 2016. Semi-arid zone caves:
1932 Evaporation and hydrological controls on delta O-18 drip water composition and implications for
1933 speleothem paleoclimate reconstructions. Quaternary Sci. Rev. 131, 285-301.

1934 Markowska, M., Baker, A., Treble, P.C., Andersen, M.S., Hankin, S., Jex, C.N., Tadros, C.V., Roach, R.,
1935 2015. Unsaturated zone hydrology and cave drip discharge water response: Implications for
1936 speleothem paleoclimate record variability. J Hydrol 529, 662-675.

1937 Markowska, M., Fohlmeister, J., Treble, P.C., Baker, A., Andersen, M.S., Hua, Q., 2019. Modelling the
1938 ¹⁴C bomb-pulse in young speleothems using a soil carbon continuum model. *Geochim. Cosmochim.*
1939 *Acta* 261, 342-367.

1940 Martin-Chivelet, J., Munoz-Garcia, M.B., Edwards, R.L., Turrero, M.J., Ortega, A.I., 2011. Land surface
1941 temperature changes in Northern Iberia since 4000 yr BP, based on delta C-13 of speleothems.
1942 *Global and Planet. Change* 77, 1-12.

1943 Martin-Garcia, R., Alonso-Zarza, A.M., Martin-Perez, A., Schroder-Ritzrau, A., Ludwig, T., 2014.
1944 Relationships between colour and diagenesis in the aragonite-calcite speleothems in Basajaun Etxea
1945 cave, Spain. *Sediment Geol* 312, 63-75.

1946 Matthey, D., Collister, C., 2008. Controls on water drop volume at speleothem drip sites: An
1947 experimental study. *J Hydrol* 358, 259-267.

1948 Matthey, D., Lowry, D., Duffet, J., Fisher, R., Hodge, E., Frisia, S., 2008. A 53 year seasonally resolved
1949 oxygen and carbon isotope record from a modern Gibraltar speleothem: Reconstructed drip water
1950 and relationship to local precipitation. *Earth Planet. Sci. Lett.* 269, 80-95.

1951 Matthey, D.P., Atkinson, T.C., Barker, J.A., Fisher, R., Latin, J.P., Durell, R., Ainsworth, M., 2016. Carbon
1952 dioxide, ground air and carbon cycling in Gibraltar karst. *Geochim. Cosmochim. Acta* 184, 88-113.

1953 Matthey, D.P., Fairchild, I.J., Atkinson, T.C., 2009. Seasonal microclimate control on calcite fabrics,
1954 stable isotopes and trace elements in modern speleothem from St. Michaels Cave, Gibraltar.
1955 *Geochim. Cosmochim. Acta* 73, A849-A849.

1956 Matthey, D.P., Fairchild, I.J., Atkinson, T.C., Latin, J.-P., Ainsworth, M., Durell, R., 2010. Seasonal
1957 microclimate control of calcite fabrics, stable isotopes and trace elements in modern speleothem
1958 from St Michaels cave, Gibraltar in: Pedley, H.M., Rogerson, M. (Eds.), *Tufas and Speleothems:*

1959 Unravelling the Microbial and Physical Controls. Geological Society of London Special Publication,
1960 London, pp. 323-344.

1961 Maupin, C.R., Partin, J.W., Shen, C.C., Quinn, T.M., Lin, K., Taylor, F.W., Banner, J.L., Thirumalai, K.,
1962 Sinclair, D.J., 2014. Persistent decadal-scale rainfall variability in the tropical South Pacific
1963 Convergence Zone through the past six centuries. *Clim Past* 10, 1319-1332.

1964 McDermott, F., 2004. Palaeo-climate reconstruction from stable isotope variations in speleothems: a
1965 review. *Quaternary Sci. Rev.* 23, 901-918.

1966 McDermott, F., Atkinson, T.C., Fairchild, I.J., Baldini, L.M., Matthey, D.P., 2011. A first evaluation of the
1967 spatial gradients in delta O-18 recorded by European Holocene speleothems. *Global and Planet.
1968 Change* 79, 275-287.

1969 McMillan, E.A., Fairchild, I.J., Frisia, S., Borsato, A., McDermott, F., 2005. Annual trace element cycles
1970 in calcite-aragonite speleothems: evidence of drought in the western Mediterranean 1200-1100 yr
1971 BP. *J. of Quaternary Sci.* 20, 423-433.

1972 Menne, M.J., Durre, I., Vose, R.S., Gleason, B.E., Houston, T.G., 2012. An Overview of the Global
1973 Historical Climatology Network-Daily Database. *J Atmos Ocean Tech* 29, 897-910.

1974 Mickler, P.J., Stern, L.A., Banner, J.L., 2006. Large kinetic isotope effects in modern speleothems.
1975 *Geol. Soc. Am. Bull.* 118, 65-81.

1976 Millo, C., Strikis, N.M., Vonhof, H.B., Deininger, M., da Cruz, F.W., Wang, X.F., Cheng, H., Edwards,
1977 R.L., 2017. Last glacial and Holocene stable isotope record of fossil dripwater from subtropical Brazil
1978 based on analysis of fluid inclusions in stalagmites. *Chem. Geol.* 468, 84-96.

1979 Mischel, S.A., Scholz, D., Spötl, C., 2015. $\delta^{18}O$ values of cave drip water: a promising proxy for the
1980 reconstruction of the North Atlantic Oscillation? *Climate Dynamics* 45, 3035-3050.

- 1981 Moerman, J.W., Cobb, K.M., Partin, J.W., Meckler, A.N., Carolin, S.A., Adkins, J.F., Lejau, S., Malang,
1982 J., Clark, B., Tuen, A.A., 2014. Transformation of ENSO-related rainwater to dripwater $\delta^{18}\text{O}$
1983 variability by vadose water mixing. *Geophys Res Lett* 41, 7907-7915.
- 1984 Moquet, J.S., Cruz, F.W., Novello, V.F., Strikis, N.M., Deininger, M., Karmann, I., Santos, R.V., Millo,
1985 C., Apaestegui, J., Guyot, J.L., Siffedine, A., Vuille, M., Cheng, H., Edwards, R.L., Santini, W., 2016.
1986 Calibration of speleothem delta O-18 records against hydroclimate instrumental records in Central
1987 Brazil. *Global and Planet. Change* 139, 151-164.
- 1988 Morellón, M., Valero-Garcés, B., Vegas-Villarrúbia, T., González-Sampériz, P., Romero, O., Delgado-
1989 Huertas, A., Mata, P., Moreno, A., Rico, M., Corella, J.P., 2009. Lateglacial and Holocene
1990 palaeohydrology in the western Mediterranean region: the Lake Estanya record (NE Spain).
1991 *Quaternary Science Reviews* 28, 2582-2599.
- 1992 Moreno, A., Pérez-Mejías, C., Bartolomé, M., Sancho, C., Cacho, I., Stoll, H., Delgado-Huertas, A.,
1993 Hellstrom, J., Edwards, R.L., Cheng, H., 2017. New speleothem data from Molinos and Ejulve caves
1994 reveal Holocene hydrological variability in northeast Iberia. *Quaternary Research* 88, 223-233.
- 1995 Moreno, A., Sancho, C., Bartolomé, M., Oliva-Urcia, B., Delgado-Huertas, A., Estrela, M.J., Corell, D.,
1996 López-Moreno, J.I., Cacho, I., 2014. Climate controls on rainfall isotopes and their effects on cave
1997 drip water and speleothem growth: the case of Molinos cave (Teruel, NE Spain). *Climate Dynamics*
1998 43, 221-241.
- 1999 Moseley, G.E., Spötl, C., Cheng, H., Boch, R., Min, A., Edwards, R.L., 2015. Termination-II
2000 interstadial/stadial climate change recorded in two stalagmites from the north European Alps.
2001 *Quaternary Science Reviews* 127, 229-239.
- 2002 Müller, W., Fietzke, J., 2016. The role of LA-ICP-MS in palaeoclimate research. *Elements* 12, 329-334.

2003 Müller, W., Shelley, M., Miller, P., Broude, S., 2009. Initial performance metrics of a new custom-
2004 designed ArF excimer LA-ICPMS system coupled to a two-volume laser-ablation cell. *J. Anal. At.*
2005 *Spectrom.* 24, 209-214.

2006 Müller, W., Valley, J.W., Warter, V., Kodzon, R., Evans, D., Orland, I.J., 2015. Natural high-
2007 temperature metamorphic calcite as compositionally homogenous microanalytical standard?,
2008 *Goldschmidt 2015, Prague.*

2009 Murata, F., Terao, T., Hayashi, T., Asada, H., Matsumoto, J., 2007. Relationship between atmospheric
2010 conditions at Dhaka, Bangladesh, and rainfall at Cherrapunjee, India. *Natural Hazards* 44, 399-410.

2011 Myers, C.G., Oster, J.L., Sharp, W.D., Bennartz, R., Kelley, N.P., Covey, A.K., Breitenbach, S.F.M.,
2012 2015. Northeast Indian stalagmite records Pacific decadal climate change: Implications for moisture
2013 transport and drought in India. *Geophys. Res. Lett.* 42, 4124-4132.

2014 Nagra, G., Treble, P.C., Andersen, M.S., Bajo, P., Hellstrom, J., Baker, A., 2017. Dating stalagmites in
2015 mediterranean climates using annual trace element cycles. *Sci. Rep.* 7, 621.

2016 Noronha, A.L., Johnson, K.R., Southon, J.R., Hu, C., Ruan, J., McCabe-Glynn, S., 2015. Radiocarbon
2017 evidence for decomposition of aged organic matter in the vadose zone as the main source of
2018 speleothem carbon. *Quaternary Sci. Rev.* 127, 37-47.

2019 O'Neil, J.R., Clayton, R.M., Mayeda, T., 1969. Oxygen isotope fractionation in divalent metal
2020 carbonates. *J. Chem. Phys.* 30, 5547-5558.

2021 Oerter, E.J., Sharp, W.D., Oster, J.L., Ebeling, A., Valley, J.W., Kodzon, R., Orland, I.J., Hellstrom, J.,
2022 Woodhead, J.D., Hergt, J.M., Chadwick, O.A., Amundson, R., 2016. Pedothem carbonates reveal
2023 anomalous North American atmospheric circulation 70,000–55,000 years ago. *Proc Natl Acad Sci U S*
2024 *A* 113, 919-924.

2025 Onac, B.P., Pace-Graczyk, K., Atudirei, V., 2008. Stable isotope study of precipitation and cave drip
2026 water in Florida (USA): implications for speleothem-based paleoclimate studies. *Isot. Environ. Health*
2027 *Stud.* 44, 149-161.

2028 Orland, I.J., Bar-Matthews, M., Ayalon, A., Matthews, A., Kozdon, R., Ushikubo, T., Valley, J.W., 2012.
2029 Seasonal resolution of Eastern Mediterranean climate change since 34 ka from a Soreq Cave
2030 speleothem. *Geochim. Cosmochim. Acta* 89, 240-255.

2031 Orland, I.J., Bar-Matthews, M., Kita, N.T., Ayalon, A., Matthews, A., Valley, J.W., 2008. Seasonal
2032 climate change as revealed by ion microprobe analysis of delta O-18 in Soreq Cave (Israel)
2033 speleothems. *Geochimica Et Cosmochimica Acta* 72, A709-A709.

2034 Orland, I.J., Bar-Matthews, M., Kita, N.T., Ayalon, A., Matthews, A., Valley, J.W., 2009. Climate
2035 deterioration in the Eastern Mediterranean as revealed by ion microprobe analysis of a speleothem
2036 that grew from 2.2 to 0.9 ka in Soreq Cave, Israel. *Quaternary Research* 71, 27-35.

2037 Orland, I.J., Burstyn, Y., Bar-Matthews, M., Kozdon, R., Ayalon, A., Matthews, A., Valley, J.W., 2014.
2038 Seasonal climate signals (1990-2008) in a modern Soreq Cave stalagmite as revealed by high-
2039 resolution geochemical analysis. *Chemical Geology* 363, 322-333.

2040 Orland, I.J., Edwards, R.L., Cheng, H., Kozdon, R., Cross, M., Valley, J.W., 2015. Direct measurements
2041 of deglacial monsoon strength in a Chinese stalagmite. *Geology* 43, 555-558.

2042 Orland, I.J., He, F., Bar-Matthews, M., Chen, G., Ayalon, A., Kutzbach, J.E., 2019. Resolving seasonal
2043 rainfall changes in the Middle East during the last interglacial period. *Proc Natl Acad Sci U S A* 116,
2044 24985-24990.

2045 Orland, I.J.d., 2013. Seasonality from speleothems : high-resolution ion microprobe studies at Soreq
2046 Cave, Israel. Ann Arbor, MI : ProQuest LLC, 2013.

2047 Orr, P.C., 1952. Excavations in Moaning Cave. Santa Barbara Museum of Natural History Bulletin 1, 1-
2048 19.

2049 Ortega, R., Maire, R., Deves, G., Quinif, Y., 2005. High-resolution mapping of uranium and other trace
2050 elements in recrystallized aragonite-calcite speleothems from caves in the Pyrenees (France):
2051 Implications for U-series dating. *Earth Planet. Sci. Lett.* 237, 911-023.

2052 Oster, J.L., Montañez, I.P., Kelley, N.P., 2012. Response of a modern cave system to large seasonal
2053 precipitation variability. *Geochim. Cosmochim. Acta* 91, 92-108.

2054 Pacton, M., Breitenbach, S.F.M., Lechleitner, F.A., Vaks, A., Rollion-Bard, C., Gutareva, O.S., Osintcev,
2055 A.V., Vasconcelos, C., 2013. The role of microorganisms in the formation of a stalactite in Botovskaya
2056 Cave, Siberia – paleoenvironmental implications. *Biogeosciences* 10, 6115-6130.

2057 Parton, A., Farrant, A.R., Leng, M.J., Telfer, M.W., Groucutt, H.S., Petraglia, M.D., Parker, A.G., 2015.
2058 Alluvial fan records from southeast Arabia reveal multiple windows for human dispersal. *Geol.* 43,
2059 295-298.

2060 Peel, M.C., Finlayson, B.L., McMahon, T.A., 2007. Updated world map of the Köppen-Geiger climate
2061 classification. *Hydrology and Earth System Sciences* 11, 1633-1644.

2062 Perrin, J., Jeannin, P.-Y., Zwahlen, F., 2003. Epikarst storage in a karst aquifer: a conceptual model
2063 based on isotopic data, Milandre test site, Switzerland. *Journal of Hydrology* 279, 106-124.

2064 Prokop, P., Walanus, A., 2003. Trends and periodicity in the longest instrumental rainfall series for
2065 the area of most extreme rainfall in the world, northeast India. *Geographia Polonica* 76, 25-35.

2066 Pu, J., Wang, A., Shen, L., Yin, J., Yuan, D., Zhao, H., 2016. Factors controlling the growth rate, carbon
2067 and oxygen isotope variation in modern calcite precipitation in a subtropical cave, Southwest China.
2068 *Journal of Asian Earth Sciences* 119, 167-178.

2069 Railsback, L.B., 2018. A comparison of growth rate of late Holocene stalagmites with atmospheric
2070 precipitation and temperature, and its implications for paleoclimatology. *Quaternary Science*
2071 *Reviews* 187, 94-111.

2072 Railsback, L.B., Brook, G.A., Chen, J., Kalin, R., Fleisher, C., 1994. Environmental controls on the
2073 petrology of a late Holocene speleothem from Botswana with annual layers of aragonite and calcite.
2074 *J Sediment Res A64*, 147-155.

2075 Railsback, L.B., Liang, F.Y., Romani, J.R.V., Grandal-d'Anglade, A., Rodriguez, M.V., Fidalgo, L.S.,
2076 Mosquera, D.F., Cheng, H., Edwards, R.L., 2011. Petrographic and isotopic evidence for Holocene
2077 long-term climate change and shorter-term environmental shifts from a stalagmite from the Serra
2078 do Courel of northwestern Spain, and implications for climatic history across Europe and the
2079 Mediterranean. *Palaeogeography Palaeoc.* 305, 172-184.

2080 Railsback, L.B., Liang, F.Y., Vidal-Romani, J.R., Garrett, K.B., Sellers, R.C., Vaquero-Rodriguez, M.,
2081 Grandal-d'Anglade, A., Cheng, H., Edwards, R.L., 2017. Radiometric, isotopic, and petrographic
2082 evidence of changing interglacials over the past 550,000 years from six stalagmites from the Serra do
2083 Courel in the Cordillera Cantabrica of northwestern Spain. *Palaeogeography Palaeoc.* 466, 137-152.

2084 Ramakrishnan, P.S., Subhash, C.R., 1988. Vegetation, biomass and productivity of seral grasslands of
2085 Cherrapunji in north-east India. *Vegetatio* 74, 47-53.

2086 Ridley, H., Baldini, J., Pruffer, K., Walczak, I., Breitenbach, S., 2015a. High-resolution monitoring of Yok
2087 Balum Cave, Belize: An investigation of seasonal ventilation regimes and the atmospheric and drip-
2088 flow response to a local earthquake. *Journal of Cave and Karst Studies* 77, 183-199.

2089 Ridley, H.E., Asmerom, Y., Baldini, J.U.L., Breitenbach, S.F.M., Aquino, V.V., Pruffer, K.M., Culleton,
2090 B.J., Polyak, V., Lechleitner, F.A., Kennett, D.J., Zhang, M., Marwan, N., Macpherson, C.G., Baldini,

2091 L.M., Xiao, T., Peterkin, J.L., Awe, J., Haug, G.H., 2015b. Aerosol forcing of the position of the
2092 intertropical convergence zone since AD1550. *Nat. Geosci.* 8, 195–200.

2093 Riechelmann, D.F.C., Deininger, M., Scholz, D., Riechelmann, S., Schroder-Ritzrau, A., Spotl, C.,
2094 Richter, D.K., Mangini, A., Immenhauser, A., 2013. Disequilibrium carbon and oxygen isotope
2095 fractionation in recent cave calcite: Comparison of cave precipitates and model data. *Geochim.*
2096 *Cosmochim. Acta* 103, 232-244.

2097 Riechelmann, D.F.C., Schroder-Ritzrau, A., Scholz, D., Fohlmeister, J., Spotl, C., Richter, D.K., Mangini,
2098 A., 2011. Monitoring Bunker Cave (NW Germany): A prerequisite to interpret geochemical proxy
2099 data of speleothems from this site. *J Hydrol* 409, 682-695.

2100 Riechelmann, S., Breitenbach, S.F.M., Schroder-Ritzrau, A., Mangini, A., Immenhauser, A., 2019.
2101 Ventilation and Cave Air PCO₂ in the Bunker-Emst Cave System (NW Germany): Implications for
2102 Speleothem Proxy Data. *J Cave Karst Stud* 81, 98-112.

2103 Riechelmann, S., Schröder-Ritzrau, A., Spötl, C., Riechelmann, D.F.C., Richter, D.K., Mangini, A.,
2104 Frank, N., Breitenbach, S.F.M., Immenhauser, A., 2017. Sensitivity of Bunker Cave to climatic forcings
2105 highlighted through multi-annual monitoring of rain-, soil-, and dripwaters. *Chemical Geology* 449,
2106 194-205.

2107 Rittner, M., Muller, W., 2012. 2D mapping of LA-ICPMS trace element distributions using R.
2108 *Computers & Geosciences* 42, 152-161.

2109 Roberts, M.S., Smart, P.L., Baker, A., 1998. Annual trace element variations in a Holocene
2110 speleothem. *Earth Planet. Sci. Lett.* 154, 237-246.

2111 Ronay, E.R., Breitenbach, S.F.M., Oster, J.L., 2019. Sensitivity of speleothem records in the Indian
2112 Summer Monsoon region to dry season infiltration. *Sci Rep* 9, 5091.

2113 Sade, Z., Halevy, I., 2017. New constraints on kinetic isotope effects during CO₂(aq) hydration and
2114 hydroxylation: Revisiting theoretical and experimental data. *Geochim. Cosmochim. Acta* 214, 246-
2115 265.

2116 Santer, B.D., Po-Chedley, S., Zelinka, M.D., Cvijanovic, I., Bonfils, C., Durack, P.J., Fu, Q., Kiehl, J.,
2117 Mears, C., Painter, J., Pallotta, G., Solomon, S., Wentz, F.J., Zou, C.-Z., 2018. Human influence on the
2118 seasonal cycle of tropospheric temperature. *Science* 361, eaas8806.

2119 Schubert, B.A., Jahren, A.H., 2015. Seasonal temperature and precipitation recorded in the intra-
2120 annual oxygen isotope pattern of meteoric water and tree-ring cellulose. *Quaternary Science*
2121 *Reviews* 125, 1-14.

2122 Schwarz, K., Barth, J.A.C., Postigo-Rebollo, C., Grathwohl, P., 2009. Mixing and transport of water in a
2123 karst catchment: a case study from precipitation via seepage to the spring. *Hydrology and Earth*
2124 *System Sciences* 13, 285-292.

2125 Scropton, N., Burns, S.J., Dawson, P., Rhodes, J.M., Brent, K., McGee, D., Heijnis, H., Gadd, P.,
2126 Hantoro, W., Gagan, M., 2018. Rapid measurement of strontium in speleothems using core-scanning
2127 micro X-ray fluorescence. *Chemical Geology* 487, 12-22.

2128 Shen, C.C., Lin, K., Duan, W., Jiang, X., Partin, J.W., Edwards, R.L., Cheng, H., Tan, M., 2013. Testing
2129 the annual nature of speleothem banding. *Sci Rep* 3, 2633.

2130 Sherwin, C.M., Baldini, J.U.L., 2011. Cave air and hydrological controls on prior calcite precipitation
2131 and stalagmite growth rates: Implications for palaeoclimate reconstructions using speleothems.
2132 *Geochimica et Cosmochimica Acta* 75, 3915-3929.

2133 Shopov, Y.Y., Ford, D.C., Schwarcz, H.P., 1994. Luminescent microbanding in speleothems - high-
2134 resolution chronology and paleoclimate. *Geol.* 22, 407-410.

2135 Sliwinski, M.G., Kitajima, K., Kodzon, R., Spicuzza, M., Denny, A., Valley, J.W., 2017. In situ $\delta^{13}\text{C}$ and
2136 $\delta^{18}\text{O}$ microanalysis by SIMS: A method for characterizing the carbonate components of natural and
2137 engineered CO_2 -reservoirs. *International Journal of Greenhouse Gas Control* 57, 116-133.

2138 Sliwinski, M.G., Kodzon, R., Kitajima, K., Denny, A., Spicuzza, M., Valley, J.W., 2015. In-Situ, Micron-
2139 Scale $\delta^{13}\text{C}$ & $\delta^{18}\text{O}$ Analyses (by SIMS) of Chemo-Isotopically Zoned Carbonate Cements of
2140 Diagenetic Origin—A Case Study on the Implications for the Thermal and Burial History of the Eau
2141 Claire Fm., Illinois Basin (USA). AAPG Annual Convention and Exhibition.

2142 Smart, P.L., Friedrich, H., 1987. Water movement and storage in the unsaturated zone of a maturely
2143 karstified aquifer, Mendip Hills, England, The conference on environmental problems in karst
2144 terrains and their solution. National Water Well Association, Bowling Green, Kentucky, pp. 57-87.

2145 Smith, C.L., Fairchild, I.J., Spotl, C., Frisia, S., Borsato, A., Moreton, S.G., Wynn, P.M., 2009.
2146 Chronology building using objective identification of annual signals in trace element profiles of
2147 stalagmites. *Quat Geochronol* 4, 11-21.

2148 Spengler, R.N., 2019. *Fruit from the Sands: The Silk Road Origins of the Foods We Eat*, 1 ed.
2149 University of California Press, Oakland, California.

2150 Spötl, C., Fairchild, I.J., Tooth, A.F., 2005. Cave air control on dripwater geochemistry, Obir Caves
2151 (Austria): implications for speleothem deposition in dynamically ventilated caves. *Geochim.*
2152 *Cosmochim. Acta* 69, 2451-2468.

2153 Spötl, C., Matthey, D., 2006. Stable isotope microsampling of speleothems for palaeoenvironmental
2154 studies: A comparison of microdrill, micromill and laser ablation techniques. *Chem. Geol.* 235, 48-58.

2155 Stoll, H., Mendez-Vicente, A., Gonzalez-Lemos, S., Moreno, A., Cacho, I., Cheng, H., Edwards, R.L.,
2156 2015. Interpretation of orbital scale variability in mid-latitude speleothem $\delta^{18}\text{O}$: Significance of
2157 growth rate controlled kinetic fractionation effects. *Quaternary Science Reviews* 127, 215-228.

2158 Stoll, H.M., Müller, W., Prieto, M., 2012. I-STAL, a model for interpretation of Mg/Ca, Sr/Ca and
2159 Ba/Ca variations in speleothems and its forward and inverse application on seasonal to millennial
2160 scales. *Geochemistry Geophysics Geosystems* 13, 09004.

2161 Surić, M., Lončarić, R., Lončar, N., Buzjak, N., Bajo, P., Drysdale, R.N., 2017. Isotopic characterization
2162 of cave environments at varying altitudes on the eastern Adriatic coast (Croatia) – Implications for
2163 future speleothem-based studies. *Journal of Hydrology* 545, 367-380.

2164 Tabersky, D., Nishiguchi, K., Utani, K., Ohata, M., Dietiker, R., Fricker, M.B., de Maddalena, I.M.,
2165 Koch, J., Gunther, D., 2013. Aerosol entrainment and a large-capacity gas exchange device (Q-GED)
2166 for laser ablation inductively coupled plasma mass spectrometry in atmospheric pressure air. *J. Anal.*
2167 *At. Spectrom.* 28, 831-842.

2168 Tadros, C.V., Treble, P.C., Baker, A., Fairchild, I., Hankin, S., Roach, R., Markowska, M., McDonald, J.,
2169 2016. ENSO-cave drip water hydrochemical relationship: a 7-year dataset from south-eastern
2170 Australia. *Hydrology and Earth System Sciences* 20, 4625-4640.

2171 Tan, M., Baker, A., Genty, D., Smith, C., Esper, J., Cai, B.G., 2006. Applications of stalagmite laminae
2172 to paleoclimate reconstructions: Comparison with dendrochronology/climatology. *Quaternary Sci.*
2173 *Rev.* 25, 2103-2117.

2174 Taylor, W., Shnaider, S., Abdykanova, A., Fages, A., Welker, F., Irmer, F., Seguin-Orlando, A., Khan, N.,
2175 Douka, K., Kolobova, K., Orlando, L., Krivoshapkin, A., Boivin, N., 2018. Early pastoral economies
2176 along the Ancient Silk Road: Biomolecular evidence from the Alay Valley, Kyrgyzstan. *Plos One* 13,
2177 e0205646.

2178 Thompson, G.M., Lumsden, D.N., Walker, R.L., Carter, J.A., 1975. Uranium series dating of
2179 stalagmites from Blanchard Springs Caverns, U.S.A. *Geochim. Cosmochim. Acta* 39, 1211-1218.

2180 Treble, P., Shelley, J.M.G., Chappell, J., 2003. Comparison of high resolution sub-annual records of
2181 trace elements in a modern (1911-1992) speleothem with instrumental climate data from southwest
2182 Australia. *Earth Planet. Sci. Lett.* 216, 141-153.

2183 Treble, P.C., Bradley, C., Wood, A., Baker, A., Jex, C.N., Fairchild, I.J., Gagan, M.K., Cowley, J., Azcurra,
2184 C., 2013. An isotopic and modelling study of flow paths and storage in Quaternary calcarenite, SW
2185 Australia; implications for speleothem paleoclimate records. *Quaternary Sci. Rev.* 64, 90-103.

2186 Treble, P.C., Chappell, J., Gagan, M.K., McKeegan, K.D., Harrison, T.M., 2005a. In situ measurement
2187 of seasonal $\delta^{18}\text{O}$ variations and analysis of isotopic trends in a modern speleothem from southwest
2188 Australia. *Earth Planet. Sci. Lett.* 233, 17-32.

2189 Treble, P.C., Chappell, J., Shelley, J.M.G., 2005b. Complex speleothem growth processes revealed by
2190 trace element mapping and scanning electron microscopy of annual layers. *Geochim. Cosmochim.*
2191 *Acta* 69, 4855-4863.

2192 Treble, P.C., Schmitt, A.K., Edwards, R.L., McKeegan, K.D., Harrison, T.M., Grove, M., Cheng, H.,
2193 Wang, Y.J., 2007. High resolution Secondary Ionisation Mass Spectrometry (SIMS) $\delta\text{O-18}$
2194 analyses of Hulu Cave speleothem at the time of Heinrich Event 1. *Chem. Geol.* 238, 197-212.

2195 Tremaine, D.M., Froelich, P.N., Wang, Y., 2011. Speleothem calcite formed in situ: Modern
2196 calibration of $\delta^{18}\text{O}$ and $\delta^{13}\text{C}$ paleoclimate proxies in a continuously-monitored natural cave system.
2197 *Geochimica et Cosmochimica Acta* 75, 4929-4950.

2198 Valley, J.W., Kita, N.T., 2009. In situ oxygen isotope geochemistry by ion microprobe, MAC short
2199 course: secondary ion mass spectrometry in the earth sciences, pp. 19-63.

2200 Vanghi, V., Borsato, A., Frisia, S., Howard, D., Gloy, G., Hellstrom, J., Bajo, P., 2019. High-resolution
2201 synchrotron X-ray fluorescence investigation of calcite coralloid speleothems: Elemental
2202 incorporation and their potential as environmental archives. *Sedimentology* 66, 2661–2685.

2203 Verheyden, S., Genty, D., Deflandre, G., Quinif, Y., Keppens, E., 2008. Monitoring climatological,
2204 hydrological and geochemical parameters in the Pere Noel cave (Belgium): implication for the
2205 interpretation of speleothem isotopic and geochemical time-series. *Int J Speleol* 37, 221-234.

2206 Vonhof, H.B., de Graaf, S., Spero, H.J., Schiebel, R., Verdegaal, S.J.A., Metcalfe, B., Haug, G.H., 2020.
2207 High-precision stable isotope analysis of <5 µg CaCO₃ samples by continuous-flow mass
2208 spectrometry. *Rapid Commun. Mass Spectrom.* 34, e8878.

2209 Vonhof, H.B., van Breukelen, M.R., Postma, O., Rowe, P.J., Atkinson, T.C., Kroon, D., 2006. A
2210 continuous-flow crushing device for on-line delta H-2 analysis of fluid inclusion water in
2211 speleothems. *Rapid Commun. Mass Spectrom.* 20, 2553-2558.

2212 Waite, A.J., Swart, P.K., 2015. The inversion of aragonite to calcite during the sampling of skeletal
2213 archives: Implications for proxy interpretation. *Rapid Commun Mass Spectrom* 29, 955-964.

2214 Walczak, I.W., 2016. Holocene climate variability revealed using geochemistry and Computed
2215 Tomography scanning of stalagmites from the North Atlantic Basin, *Earth Sciences*. Durham
2216 University, Durham, p. 199.

2217 Walczak, I.W., Baldini, J.U.L., Baldini, L.M., McDermott, F., Marsden, S., Standish, C.D., Richards, D.A.,
2218 Andreo, B., Slater, J., 2015. Reconstructing high-resolution climate using CT scanning of unsectioned
2219 stalagmites: A case study identifying the mid-Holocene onset of the Mediterranean climate in
2220 southern Iberia. *Quaternary Sci. Rev.* 127, 117-128.

2221 Wang, C., Bendle, J.A., Greene, S.E., Griffiths, M.L., Huang, J., Moossen, H., Zhang, H., Ashley, K., Xie,
2222 S., 2019a. Speleothem biomarker evidence for a negative terrestrial feedback on climate during
2223 Holocene warm periods. *Earth Planet. Sci. Lett.* 525, 115754.

2224 Wang, J.K., Johnson, K.R., Borsato, A., Amaya, D.J., Griffiths, M.L., Henderson, G.M., Frisia, S., Mason,
2225 A., 2019b. Hydroclimatic variability in Southeast Asia over the past two millennia. *Earth Planet. Sci.*
2226 *Lett.* 525, 115737.

2227 Wang, X.F., Edwards, R.L., Auler, A.S., Cheng, H., Kong, X.G., Wang, Y.J., Cruz, F.W., Dorale, J.A.,
2228 Chiang, H.W., 2017. Hydroclimate changes across the Amazon lowlands over the past 45,000 years.
2229 *Nature* 541, 204–207.

2230 Wang, Y.J., Cheng, H., Edwards, R.L., An, Z.S., Wu, J.Y., Shen, C.-C., Dorale, J.A., 2001. A high-
2231 resolution absolute-dated late Pleistocene monsoon record from Hulu Cave, China. *Science* 294,
2232 2345-2348.

2233 Wassenburg, J., Immenhauser, A., Richter, D., Jochum, K., Fietzke, J., Deininger, M., Goos, M., Scholz,
2234 D., Sabaoui, A., 2012. Climate and cave control on Pleistocene/Holocene calcite-to-aragonite
2235 transitions in speleothems from Morocco: Elemental and isotopic evidence. *Geochim. Cosmochim.*
2236 *Acta* 92, 23–47.

2237 Webb, M., Dredge, J., Barker, P.A., Müller, W., Jex, C., Desmarchelier, J., Hellstrom, J., Wynn, P.M.,
2238 2014. Quaternary climatic instability in south-east Australia from a multi-proxy speleothem record. *J.*
2239 *of Quaternary Sci.* 29, 589-596.

2240 Welte, C., Wacker, L., Hattendorf, B., Christl, M., Fohlmeister, J., Breitenbach, S.F.M., Robinson, L.F.,
2241 Andrews, A.H., Freiwald, A., Farmer, J.R., Yeman, C., Synal, H.A., Gunther, D., 2016. Laser Ablation -
2242 Accelerator Mass Spectrometry: An Approach for Rapid Radiocarbon Analyses of Carbonate Archives
2243 at High Spatial Resolution. *Anal. Chem.* 88, 8570-8576.

2244 Wiedenbeck, M., Bugoi, R., Duke, M.J.M., Dunai, T., Enzweiler, J., Horan, M., Jochum, K.P., Linge, K.,
2245 Kosler, J., Merchel, S., Morales, L.F.G., Nasdala, L., Stalder, R., Sylvester, P., Weis, U., Zoubir, A., 2012.

2246 GGR Biennial Critical Review: Analytical Developments Since 2010. *Geostandards and Geoanalytical*
2247 *Research* 36, 337-398.

2248 Wong, C.I., Banner, J.L., Musgrove, M., 2011. Seasonal dripwater Mg/Ca and Sr/Ca variations driven
2249 by cave ventilation: Implications for and modeling of speleothem paleoclimate records. *Geochimica*
2250 *et Cosmochimica Acta* 75, 3514-3529.

2251 Wong, C.I., Breecker, D.O., 2015. Advancements in the use of speleothems as climate archives.
2252 *Quaternary Science Reviews* 127, 1-18.

2253 Woodhead, J.D., Hellstrom, J., Hergt, J.M., Greig, A., Maas, R., 2007. Isotopic and elemental imaging
2254 of geological materials by laser ablation inductively coupled plasma-mass spectrometry.
2255 *Geostandards and Geoanalytical Research* 31, 331-343.

2256 Woodhead, J.D., Horstwood, M.S.A., Cottle, J.M., 2016. Advances in isotope ratio determination by
2257 LA-ICP-MS. *Elements* 12, 317-322.

2258 Wortham, B.E., Montanez, I.P., Rowland, D.J., Lerche, M., Browning, A., 2019. Mapping Fluid-Filled
2259 Inclusions in Stalagmites Using Coupled X-Ray and Neutron Computed Tomography: Potential as a
2260 Water Excess Proxy. *Geochemistry Geophysics Geosystems* 20, 2647-2656.

2261 Wu, X., Zhu, X., Pan, M., Zhang, M., 2014. Seasonal variability of oxygen and hydrogen stable
2262 isotopes in precipitation and cave drip water at Guilin, southwest China. *Environmental Earth*
2263 *Sciences* 72, 3183-3191.

2264 Wycech, J.B., Kelly, D.C., Kozdon, R., Orland, I.J., Spero, H.J., Valley, J.W., 2018. Comparison of $\delta^{18}\text{O}$
2265 analyses on individual planktic foraminifer (*Orbulina universa*) shells by SIMS and gas-source mass
2266 spectrometry. *Chemical Geology* 483, 119-130.

- 2267 Wynn, P.M., Fairchild, I.J., Borsato, A., Spotl, C., Hartland, A., Baker, A., Frisia, S., Baldini, J.U.L., 2018.
2268 Sulphate partitioning into calcite: Experimental verification of pH control and application to
2269 seasonality in speleothems. *Geochim. Cosmochim. Acta* 226, 69-83.
- 2270 Wynn, P.M., Fairchild, I.J., Frisia, S., Spotl, C., Baker, A., Borsato, A., EIMF, 2010. High-resolution
2271 sulphur isotope analysis of speleothem carbonate by secondary ionisation mass spectrometry.
2272 *Chemical Geology* 271, 101-107.
- 2273 Wynn, P.M., Fairchild, I.J., Spotl, C., Hartland, A., Matthey, D., Fayard, B., Cotte, M., 2014. Synchrotron
2274 X-ray distinction of seasonal hydrological and temperature patterns in speleothem carbonate.
2275 *Environ Chem* 11, 28-36.
- 2276 Yonge, C.J., Ford, D.C., Gray, J., Schwarcz, H.P., 1985. Stable isotope studies of cave seepage water.
2277 *Chemical Geology* 58, 97-105.
- 2278 Zeng, G., Luo, W., Wang, S., Du, X., 2015. Hydrogeochemical and climatic interpretations of isotopic
2279 signals from precipitation to drip waters in Liangfeng Cave, Guizhou Province, China. *Environmental*
2280 *Earth Sciences* 74, 1509-1519.

2281

2282 **Figure Captions:**

- 2283 Figure 1: Top Panel: Resolution of speleothem isotope records over time, compiled from the
2284 SISALv1b database. Individual record resolution (small black circles) and mean resolution of
2285 all available (black bars) and Holocene (blue bars) records published in a given year. Bottom
2286 panel: Total number of stalagmite records identified (grey bars), total number of stalagmite
2287 records in SISALv1b (black bars), and total number of Holocene records in SISALv1b (blue
2288 bars).

2289 Figure 2: Illustration of different drip responses from Yok Balum Cave, Belize, over
2290 approximately two months as captured by a series of automated drip loggers. Two clear rain
2291 events and the subsequent drip responses are indicated by the vertical dashed red lines.
2292 Rainfall amount is recorded directly over the cave site using a tipping bucket rain gauge.
2293 Techniques are discussed in more detail in (Ridley et al., 2015a).

2294 Figure 3: A new drip categorisation scheme designed to emphasise cave drip seasonality.
2295 The scheme does not use classification boundaries as such, but instead uses the data
2296 distribution to understand the hydrology. The scheme uses descriptors that map onto
2297 established drip terminology (see Panels B-D and main text for examples). A) Minimum and
2298 maximum hourly drip rates extracted for every month of record for numerous cave drips
2299 globally. The dashed line represents the 1:1 line, and all data points must necessarily plot
2300 over this (i.e., the minimum drip rate cannot exceed the maximum drip rate for any given
2301 month). The closer a point plots to the dashed line, the lower the difference between
2302 monthly maximum and minimum values for that point; if a point sits on the line the
2303 minimum and maximum values for that month are identical. Panels B-D illustrate some
2304 common drip types (using synthetic data) and their pattern when plotted on this diagram.
2305 Panels B-D are schematic and are not based on actual collected datasets; the symbols used
2306 are arbitrary and are not linked to the symbols used in Panel A.

2307 Figure 4: The simulated effects of sampling resolution on the climate signal extracted from a
2308 stalagmite. The stalagmite data are from stalagmite YOK-G (Yok Balum Cave, Belize), which
2309 was originally sampled with a micromill at a 100 micron (0.1 mm) step size (Ridley et al.,
2310 2015b). The chronology for the stalagmite is precise at the seasonal scale. The rainfall data

2311 (bottom panel) are from the Punta Gorda meteorological station (~30 km to the southeast
2312 of the cave site).

2313 Figure 5: Schematic of a sampling scheme for achieving ~50 micron spatial resolution. Plan
2314 view of a stalagmite surface with 1 mm conventional holes on the right and trenches cut for
2315 low and high resolution. The red trench was milled with a 0.8 mm diameter drill and the (blue-
2316 shaded) higher resolution trench was cut laterally, with each sample integrating 50 μm . The
2317 red corners highlight the area that is incorporated into subsequent steps, which in this case
2318 includes material from the current and the previous sample. In this example each high-
2319 resolution sample (e.g., yellow shaded area) integrates a minimal amount of powder of an
2320 older sample (because the milling direction is upward).

2321 Figure 6: Several examples of output generated by different geochemical-based techniques
2322 for extracting seasonal climate. A) Variability in sulphate in speleothem calcite (Obi84, Obir
2323 cave, Austria) as determined by SR- μXRF (Wynn et al., 2014). The clear annual sulphur maxima
2324 are evident as brighter green colours. B) Ion microprobe-resolved strontium and phosphorous
2325 cycles apparent in stalagmite CC3 from Crag Cave, southwestern Ireland (Baldini et al., 2002).
2326 The well-developed cycles illustrate stronger seasonality at the time of deposition (~8.336 ka
2327 BP) than currently present. C) Annual UV-luminescent banding in a stalagmite from Shihua
2328 Cave, Beijing, China (adapted from Tan et al. (2006)). D) well-develop carbon isotope ratio
2329 cycles in stalagmite YOK-G from Yok Balum Cave, Belize, constructed using data obtained via
2330 micromilling at a 100-micron spatial resolution and analyses of powders on an IRMS (Ridley
2331 et al., 2015b) (see also Figure 4). E) Mg cycles apparent in stalagmite BER-SWI-13 from
2332 Leamington Cave, Bermuda, resolved using LA-ICPMS-derived Mg data (Walczak, 2016). All
2333 panels show three to four cycles, interpreted as annual.

2334 Figure 7: A synthetic rainfall input signal (orange circles) with an annual temperature range of
2335 15 °C compared with two mean model outputs, one derived using an annual temperature
2336 range of 10 ± 6 °C (grey line), and another derived using an annual temperature range of $15 \pm$
2337 6 °C (blue line). At the beginning of the simulated rainfall input signal record (year = 0), April
2338 is the wettest month and November the driest month, but this shifts in polarity slowly through
2339 the record, moving through a brief phase with no seasonality in rainfall (year = 7), and then
2340 transitioning into a phase where April is the driest month (from year = 8). The vertical gridlines
2341 highlight the month of April during every model year. The simulated rainfall input signal
2342 amplitude and polarity is reproduced by the model very satisfactorily, provided that the
2343 model temperature range is realistic, as it is in Model 2. Note that the polarity of the simulated
2344 rainfall input signal is still reproduced by Model 1, but modelled rainfall seasonal amplitude
2345 is too large in order to compensate for the low amplitude of the modelled temperature range.

2346 Figure 8: Temperature (top panel) and rainfall (bottom panel) modelling results (black
2347 dashed lines) against 'noisy' synthetic input datasets (solid coloured lines) for seven model
2348 years. The grey rectangle highlights one model year (Year 4) where the input rainfall signal
2349 polarity was reversed; the model detects this shift. The modelling results presented are the
2350 mean values of all successful model runs for each timeslice.

2351 Figure 9: Mean modelled monthly temperature and rainfall data against Global Historical
2352 Climate Network (GHCN) and tree ring data. A) Stalagmite Keklik1 oxygen isotope ratio data
2353 from Bir-Uja Cave, Kyrgyzstan (input data) (Fohlmeister et al., 2017). B) Centennial-scale
2354 borehole temperature data from the Tian Shan region (Huang et al., 2000) from 1500 to
2355 2000 C.E. (input data, shifted upwards for clarity) (blue diamonds), modelled July
2356 temperature (black curve) (output), and NTREND summer temperature reconstruction for

2357 Asia Grid 2 (AG2) (red curve) (Cook et al., 2013). C) Modelled January rainfall (black curve)
2358 (output) and GHCN January rainfall for Tashkent (orange curve), both in % of total annual
2359 rainfall. The grey rectangles highlight the years 1797 and 1815 C.E. discussed in the text.

2360 Figure 10: Global seasonality in annual temperature ($^{\circ}\text{C}$) and annual precipitation (mm). A)
2361 The annual temperature range was calculated as the maximum temperature of the warmest
2362 month minus the minimum temperature of the coldest month averaged over the period
2363 1970-2000. B) Precipitation seasonality was calculated as the precipitation amount of the
2364 wettest month minus the precipitation amount of the driest month averaged over the
2365 period 1970-2000. WorldClim Version 2 data (<https://www.worldclim.org/>) were obtained
2366 at a 2.5 minute (~ 4.5 km at the equator) spatial resolution (Fick and Hijmans, 2017). The
2367 data span the period 1970-2000 and thus may reflect anthropogenically-influenced
2368 temperature seasonality as discussed in Santer et al. (2018). Therefore, although the general
2369 spatial pattern of temperature (and potentially precipitation) seasonality may persist into
2370 the past, the magnitude of seasonality shifts may deviate from that presented here,
2371 particularly when extending records into the preindustrial era.

2372 Figure 11: Global seasonality in amount-weighted precipitation $\delta^{18}\text{O}$ (‰ VWMOW). The
2373 amount-weighted mean (WM) monthly precipitation $\delta^{18}\text{O}$ data (IAEA/WMO, 2001) were
2374 used to determine the annual range in precipitation isotopes globally (calculated as the
2375 maximum monthly WM $\delta^{18}\text{O}$ minus minimum monthly WM $\delta^{18}\text{O}$ at 267 stations (yellow
2376 symbols) with a complete 12-month dataset over the period 1961-1999. GNIP station data
2377 were interpolated onto a $2.5^{\circ} \times 2.5^{\circ}$ global grid (~ 278 km \times 278 km) (IAEA, 2001).

2378 Figure 12: A Hovmöller plot of the annual cycle of total-column precipitable water vapour
2379 for Central America, based on daily ERA5 re-analysis data across the region from -110 to -

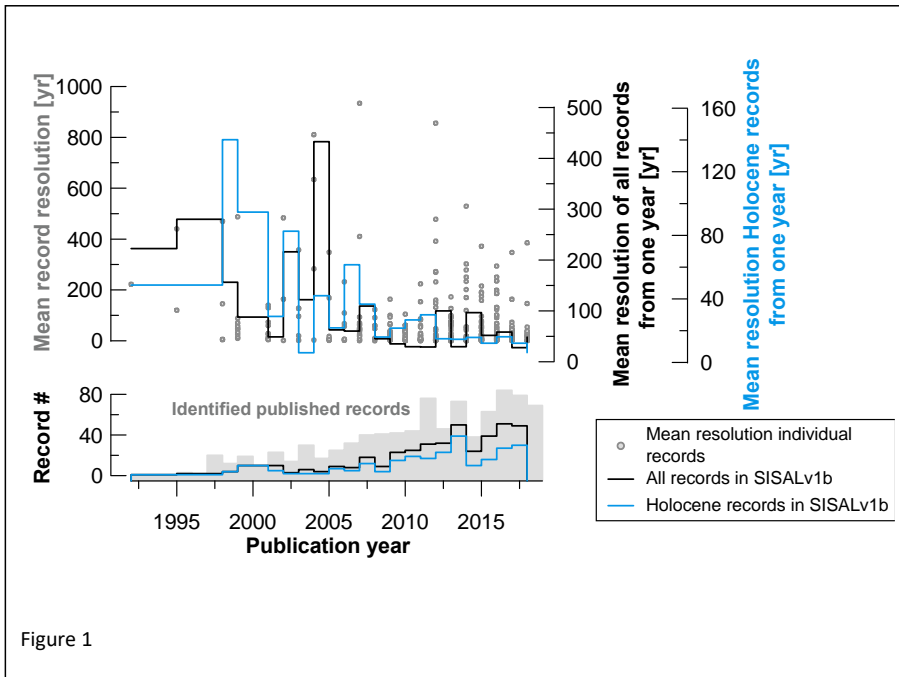
2380 80W and 0 to 35N for the period 1979-2018. Also indicated are the latitudes of three key
2381 cave sites that have yielded stalagmites which have produced oxygen isotope records of
2382 rainfall.

2383

2384 Figures:

2385

2386



2387

2388

2389

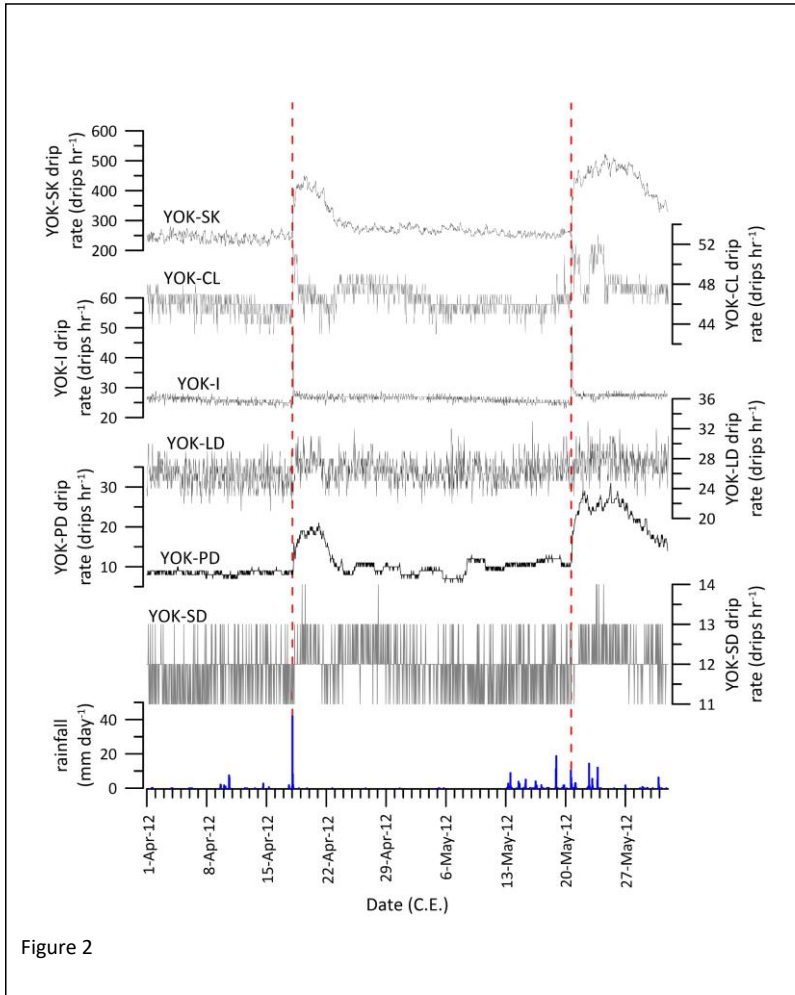


Figure 2

2390

2391

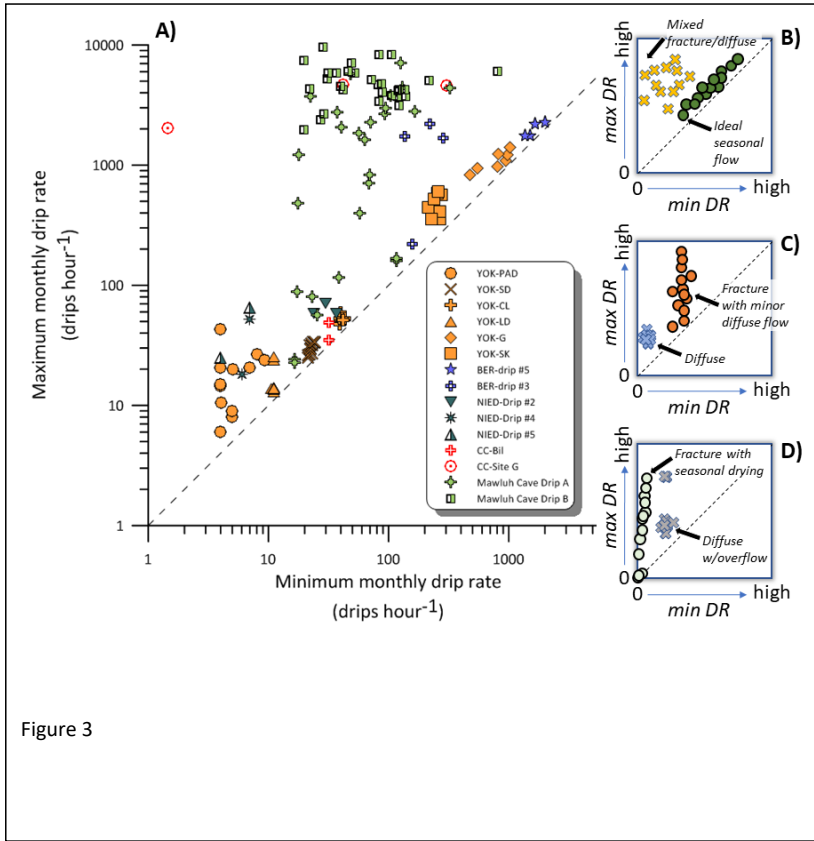


Figure 3

2392

2393

2394

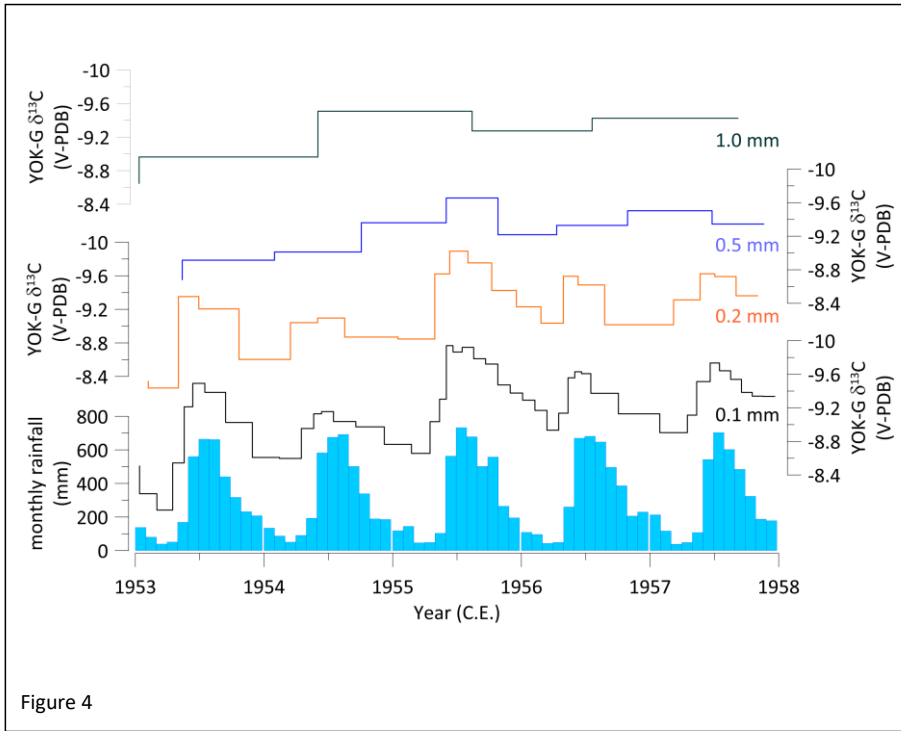


Figure 4

2395

2396

2397

2398

2399

2400

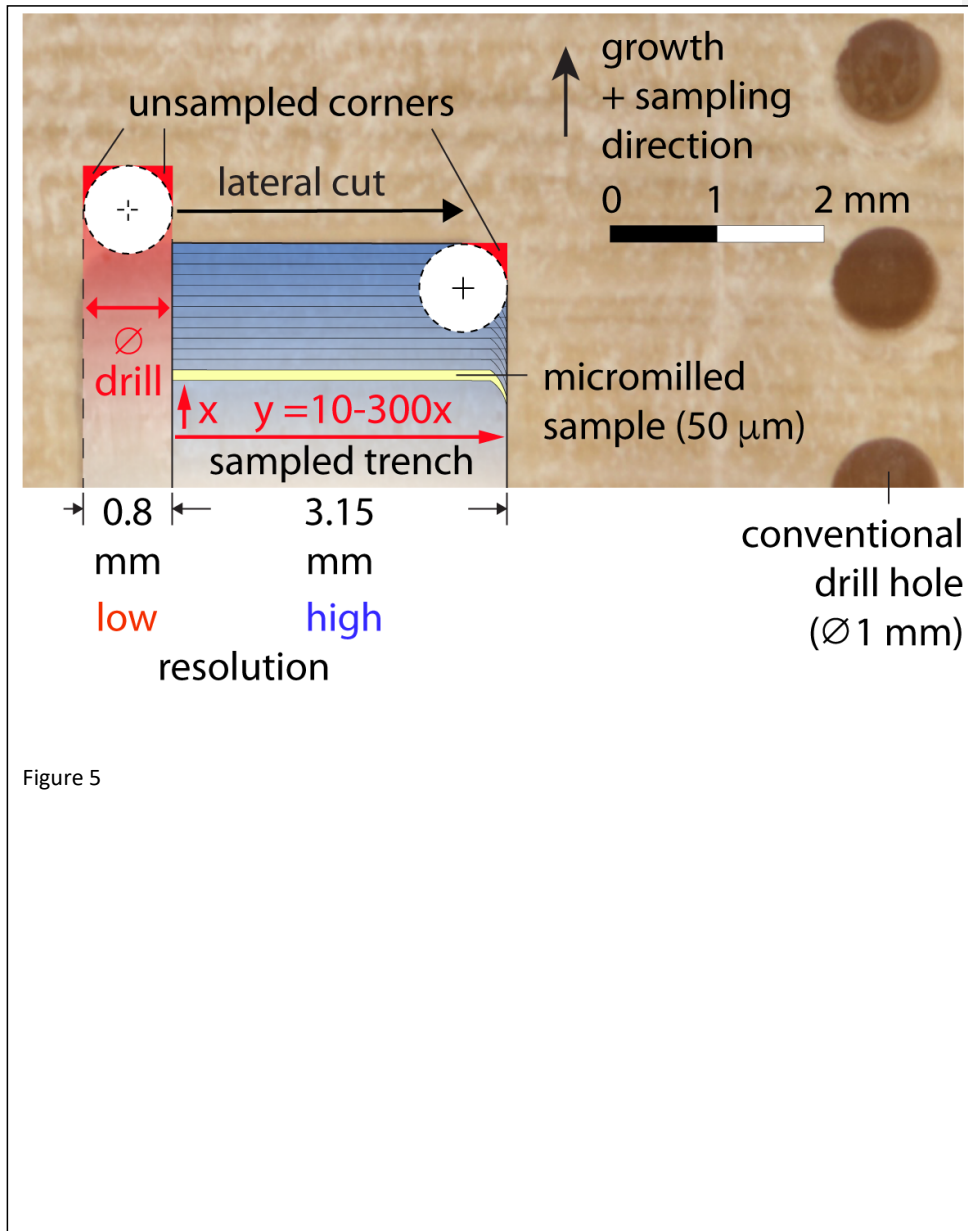


Figure 5

2403

2404

2405

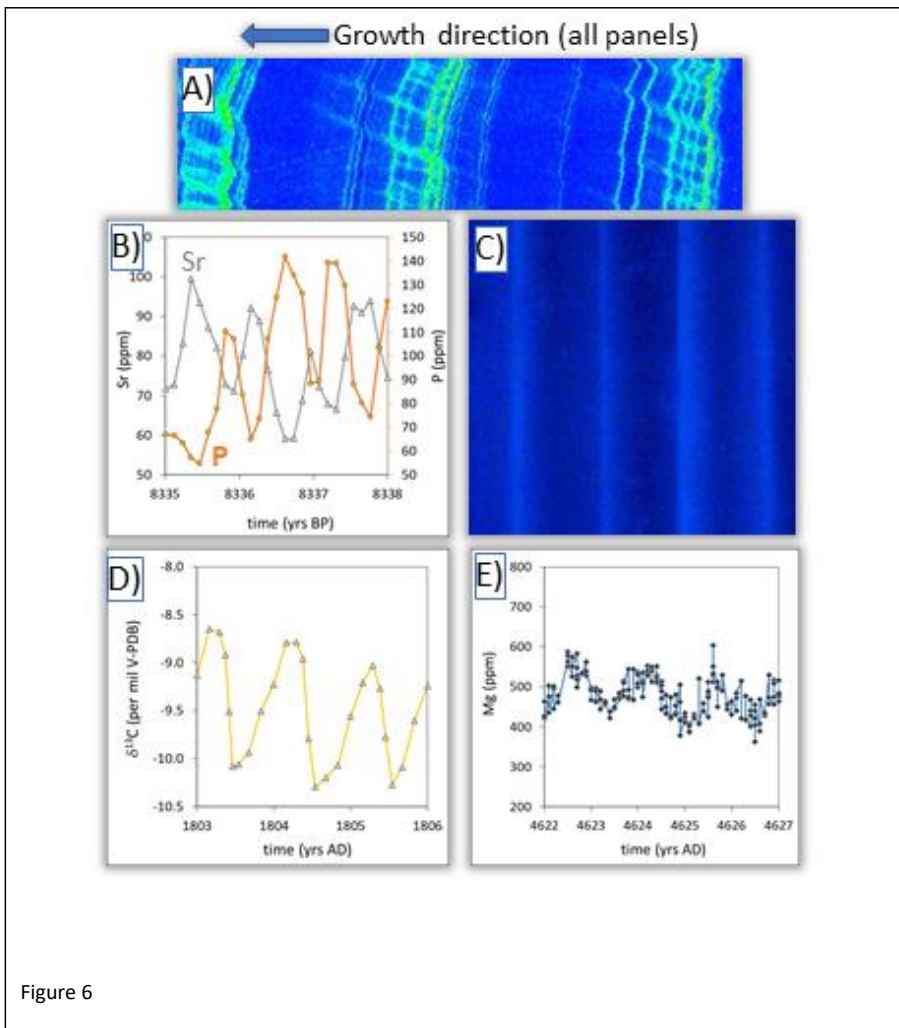
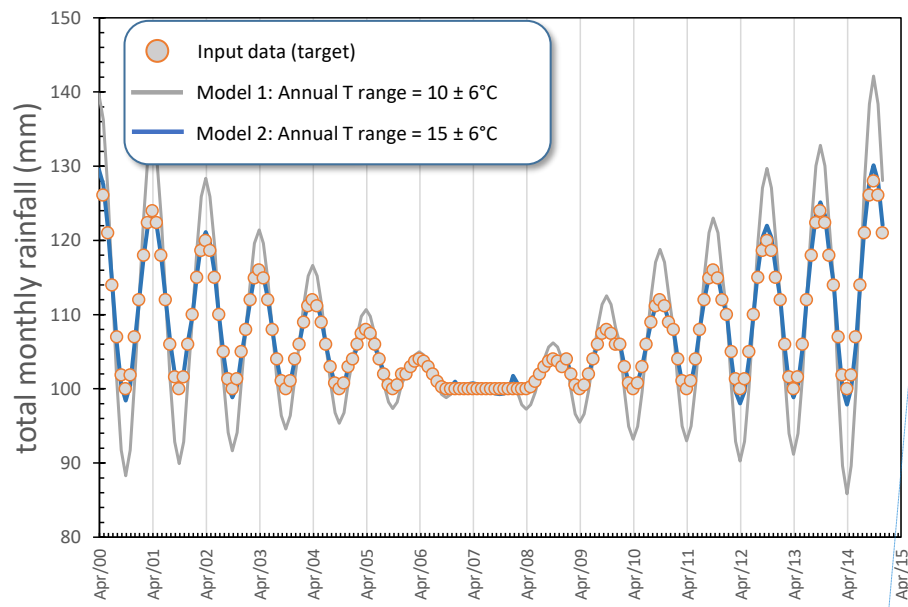


Figure 6

2406



Formatted: Pattern: Clear (Background 2)

Figure 7

2408

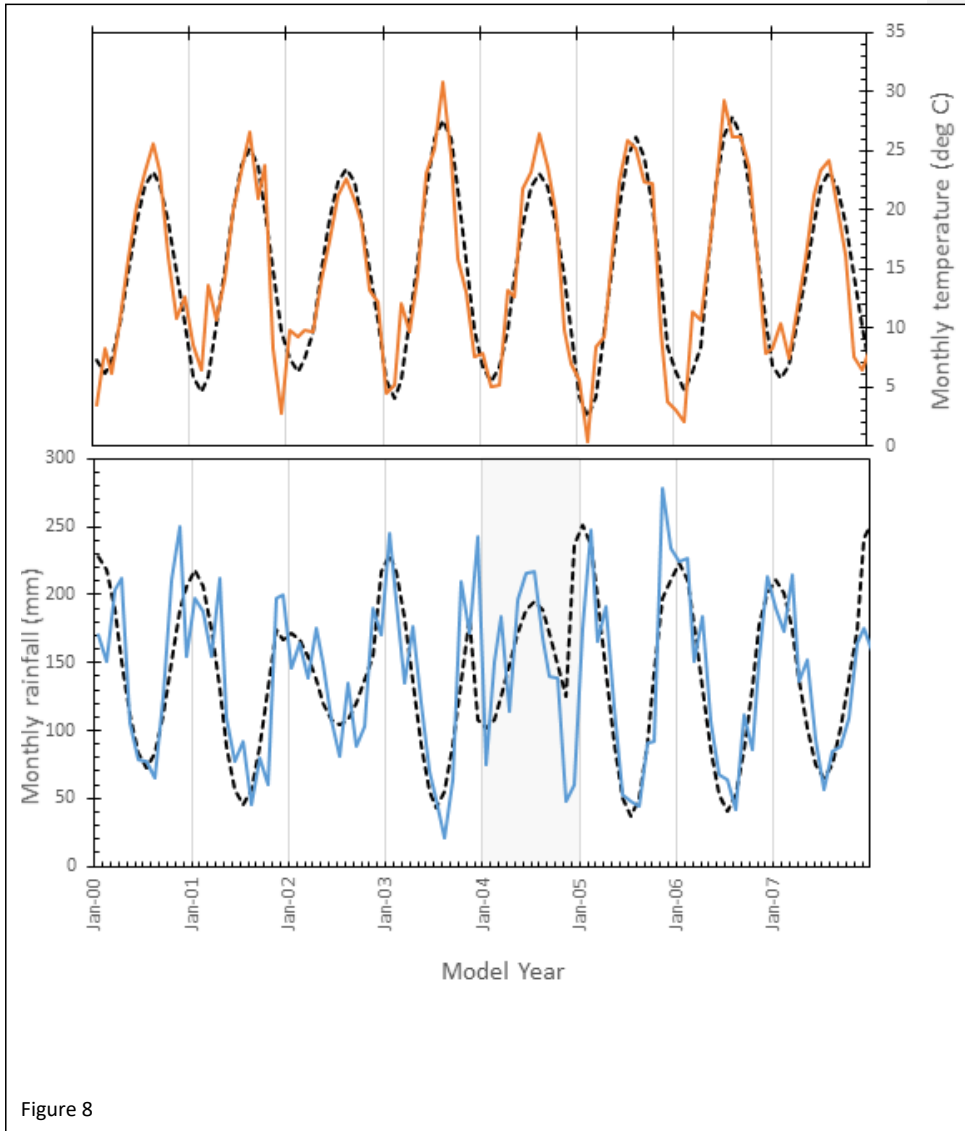


Figure 8

2409

2410

2411

2412

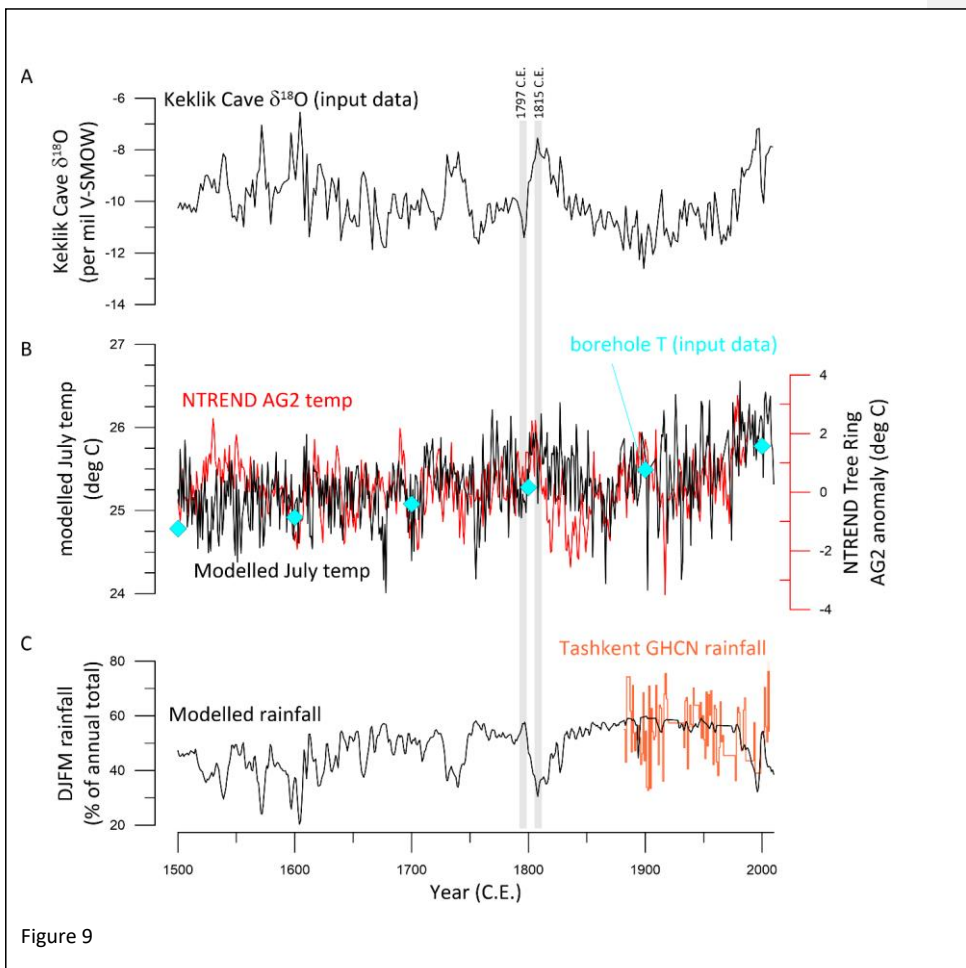
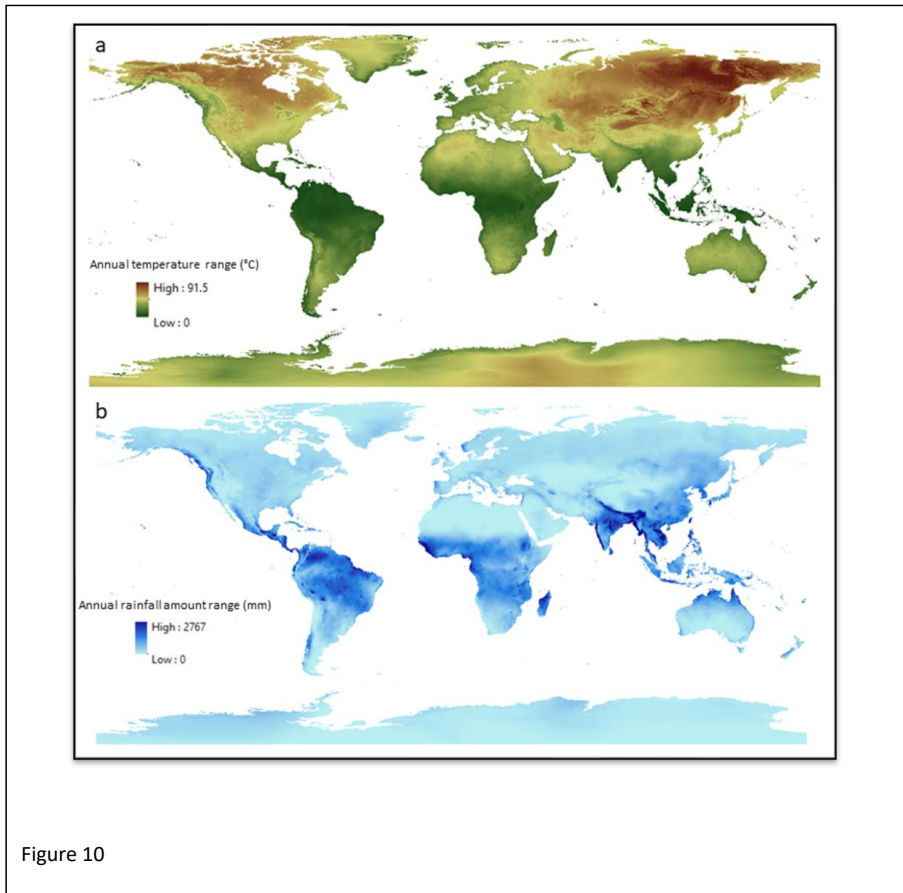


Figure 9

2413

2414

2415



2416

2417

2418

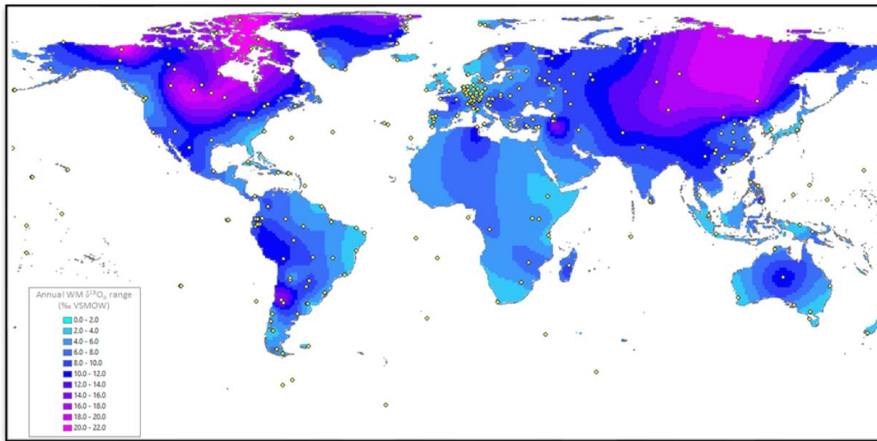
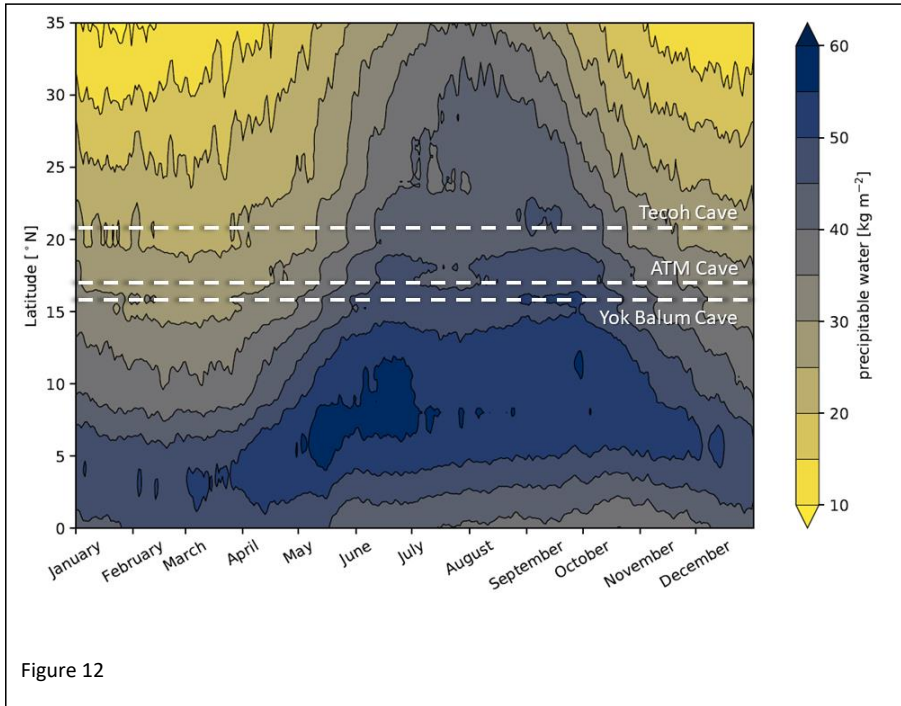


Figure 11

2419



2420

2421

2422